DOCTOR OF PHILOSOPHY

Generation of ultra-bright MeV gamma-ray beams from intense laser-matter interactions

Corvan, Darragh

Award date:
2017

Awarding institution:
Queen's University Belfast

Queen's University Belfast

A thesis presented upon application for admission to the degree of:

DOCTOR OF PHILOSOPHY

Faculty of Engineering and Physical Science

Generation of ultra-bright MeV gamma-ray beams from intense laser-matter interactions

Author:
D.J. Corvan

Supervisors:
Dr. G. Sarri
Prof. M. Zepf

May 23, 2016

Dedicated to my daughter Annie Josephine

"There are risks and costs to action. But they are far less than the long range risks of comfortable inaction." – John F. Kennedy

ABSTRACT

MeV photons are generated in a wide range of physical scenarios, ranging from unstable nuclei up to massive stellar objects such as pulsars. Using relativistically-intense laser pulses, it is possible to produce high-flux high-energy photon beams in an all optical arrangement. This thesis will provide a working theory of what plasmas and lasers are and how energy from lasers couples into plasmas; before a discussion of the generation of synchrotron radiation is presented.

A discussion into the unique diagnostics and techniques applied in the setup of such experiments will be presented in which a novel detector for high flux gamma-ray beams within the $3 - 20$ MeV range with MeV resolution is shown as well as a new technique for the temporal overlap of ultra-short pulses to fs precision is given.

This is followed by the findings from a recent experimental campaign in which NLTS was demonstrated experimentally which implies a peak brilliance of $\sim 10^{20}$ photons s^{-1} mm^{-2} $mrad^{-2}$ 0.1% BW will be presented before a discussion of the likely future work that has been planned is given.

ACKNOWLEDGEMENTS

I would like to extend my sincere thanks to those who have contributed to this body of work. Primarily to my supervisors G. Sarri and M. Zepf, whose vision and diligence lead the foundation of this thesis. With their evident passion and skill they were able to find in me, a competent and capable person, able to achieve something that may otherwise have remained unattainable.

In terms of those who have assigned their talents to progressing the work presented here, you have my utmost gratitude. To T. Dzelzainis and M. Yeung, whose tireless efforts and incredible skill, allowed me to gain a grasp of the experimental techniques necessary for completing this body of work. For W. Schumaker who designed and implemented the gas cells in the non-linear Thomson Scattering experiment I express a sincere thanks to. For C. Harvey who worked with the electron spectrum data to produce necessary theoretical results; I thank you. And finally to all of those who joined me on the experimental campaigns my sincere thanks is yours.

I would like to take the opportunity to thank St. Colman's College, Newry, who afforded me the opportunity of perusing my formal academic studies in Physics to their completion with the knowledge that I would always have a place in their community, thank you.

On a personal level, I would like to thank my wonderful wife Leeanne with whom I have shared this experience with. You have stood by me in all the trial and tribulations. You have my thanks, and my love, always.

CONTENTS

LIST OF FIGURES

Part I

INTRODUCTION

THESIS STRUCTURE

This thesis aims to build on the work that has been carried in the field of laser-plasma physics in order to investigate experimentally, the generation of high energy photons. The structure of this document is as follows:

The first part of the thesis gives an overall introduction to many of the pertinent theories which are exploited in this work. In Chapter 1 the context of this work is outlined and the need for developments in this field is identified. In Chapter 2, an overview of plasmas is given allowing one to understand the basics of what makes a plasma and it's unique dynamics. The propagation of electromagnetic radiation into a plasma is studied. Finally, the chapter closes with how energy from an intense electric field may couple into a plasma and the interesting electron dynamics that arise from such an interaction. Particular attention will be on laser wakefield acceleration. In Chapter 3, the mechanism of synchrotron radiation will be explored with attention turning to undulator and wiggler arrangements before the mechanism is applied to the context of lasers.

In the second part of the thesis, attention turns to the practical techniques that will be used. Chapter 4 looks at the generation of high intensity electric fields by lasers. Chapter 5 looks at how lasers are employed to generate high energy electron beams through laser wakefield acceleration. Then, Chapter 6 explores the spectral resolution of relativistic electrons and their detection, while Chapter 7 presents a novel detector for the detection and spectral resolution of γ-ray beams based on Compton scattering and using the principles outlined in the Chapter 6. This part closes with Chapter 8 where a new technique for the temporal overlap of intense laser pulses based on the principle of spectral interferometry is presented.

Part 3 of the thesis focuses on experimental results obtained. In Chapter 9, the techniques outlined in Chapters 6, 7 & 8 are implemented in an experimental campaign to look at an all-optical source of γ-rays via non-linear Thomson scattering.

In the Final part of the thesis, an outlook is given (Chapter 10) which will indicate the direction that the work is hoped to continue in.

1. INTRODUCTION

1.1 The Uses of High Energy Gamma-Ray Beams

The generation of high-quality multi-MeV γ-ray beams is an active field of research due to the central role played not only in fundamental research [1], but also in extremely important practical applications, which include cancer radiotherapy [2, 3], active interrogation of materials [4], and radiography of dense objects [5]. As an example, Giant Dipole Resonances of most heavy nuclei occur in an energy range of $15 - 30$ MeV [6], exciting photo-fission of the nucleus.

Moreover, their high penetration in materials promotes γ-rays as ideal tools for performing high-quality radiographs of the interior of heavily shielded objects, such as containers and cargos (of which an extremely low faction are currently able to be inspected [7]); allowing one to scan for special nuclear materials (SNM) such as Uranium−235 as seen in figure 1.1 (a) (see, for instance, the Container Security Initiative launched by the U.S. Bureau of Customs and Border Protection [8, 9, 10]). As shown in figure 1.1 (b),

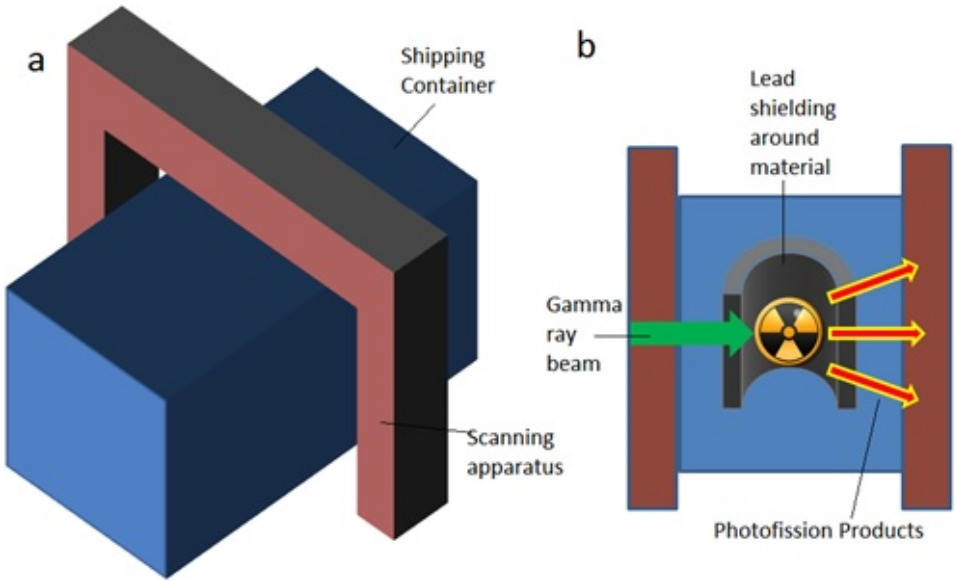

Fig. 1.1: The basic principle behind the scanning of shipping containers [11].

the basic concept behind the so called 'nuclear carwash', is akin to common scanning techniques employed in most modern airports; however, it as the energy of the photons is

much higher, their ability to penetrate into more dense materials is exploited. Moreover, the γ-ray beam is able to interact with the nucleus and may induce 'photofission' where the photons energy is absorbed and drives the nucleus into an excited state in which decay paths become available. In the case of SNM, the decay products could be neutrons of a known, fixed energy thereby leading to a unique signature which can indicate to a user that a particular SNM is present in the container. This is of course, much more efficient than a manual search of such containers and could lead to more rigorous security measures being implemented on a global scale. While other sources have been suggested for such scanners such as neutron based sources, a γ-ray source is preferable as not only are the scanning particles distinct from the products one may wish to detect but a neutron source would need costly preparation (from a particle accelerator facility) and transportation to the site. Using laser plasma techniques, it is to be shown that there is the potential to generate a compact and all optical source of high energy γ-rays with which to form the foundation of such a technology.

As well as scanning, high-energy γ-rays have an impact on living tissues and cells, inducing an extremely complex chain of phenomena in cells ranging from harmless mutations up to cell death. These phenomena are at the core of one of the most effective cancer therapies: radiotherapy [12]. For example, the use of cobalt-60 in an array to form a 'gamma-knife' has been shown to be a successful technique for radiotherapy [13].

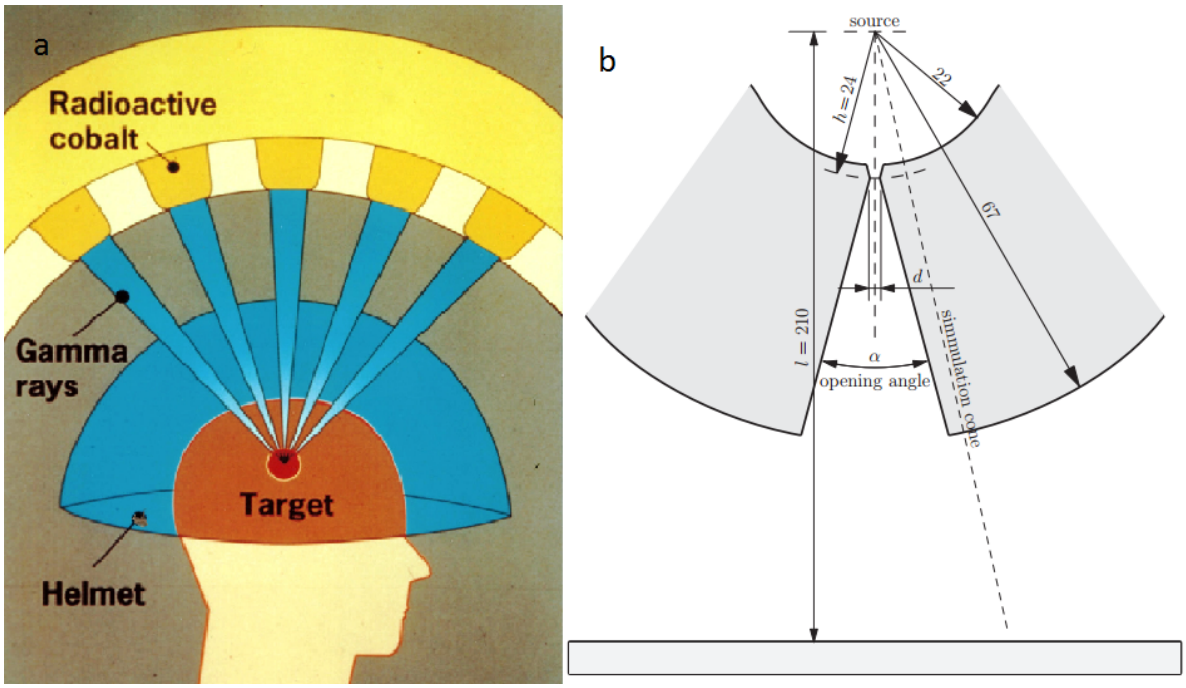

Fig. 1.2: The basic principle behind the gamma-knife (picture courtesy of Wikipedia [14]) [15].

As shown in figure 1.2 (a), the basic principle of the gamma-knife is an array of cobalt-60 sources which emit γ-rays continuously onto a target. The radiation kills the tumour

inside the patient;however, the doses delivered in this manner has the potential to effect other parts of the body not connected to cancerous growths. Research is still ongoing to see how to reduce the impact of this by reducing the number of cobalt components used [16]. The source emits over 4π sr, collimation of the source is required [15] which is a source of inefficiency and cost of the system as demonstrated in figure 1.2 (b). In order to reduce the time of which the dose is deposited (receiving the dose in such a way may be stressful for patients especially young children or animals), an alternative source of γ-rays could be used which have a higher brightness where non-linearities in dose deposition could have a beneficial effect.

1.2 The Need for an Improved Method for Generating High Energy Gamma-Rays

Different mechanisms have been proposed to generate high-quality multi-MeV γ-ray beams, including bremsstrahlung emission, conventional synchrotron emission (including the state of the art HIγS machine [1]). Figure 1.3 contrasts the varying levels of brightness of that can be achieved by various techniques employed within the larger scientific community.

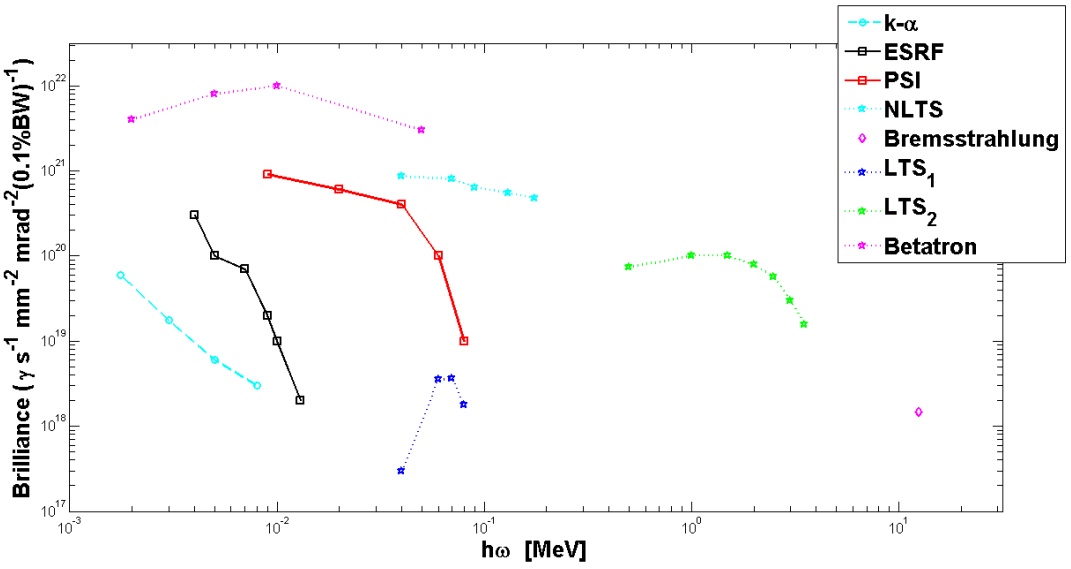

Fig. 1.3: Comparison of some of the present γ-ray source reported in current literature. Brilliance is expressed in units of photons s^{-1} mm^{-2} mrad $^{-2}$ 0.1% BW.

By focusing an intense laser pulse onto a solid target, it is possible to generate ultrashort bursts of k-α radiation (figure 1.3 blue circles, [17]). While such bursts are bright, they show large angular emittance and cannot reach the MeV regime. Synchrotrons equipped with solid-state undulators such as ESRF (figure 1.3 , grey squares [18] and

PSI, (figure 1.3 red squares [19] are able to create low-noise and coherent sources of x-rays but technological constraints on magnet construction will limit their ability to push into the MeV regime. Compton scattering (together with its classical limit, Thomson), and in-flight positron annihilation [20]. Bremsstrahlung sources are routinely used for medical applications, and exploit electron beams accelerated by linear accelerators (LINAC) [21]; however, due to the large size of LINAC's, their implentatation remains a problem.

Laser-driven electron beams with energy per particle of the order of the GeV can now be deployed in the laboratory [22] and hence, laser-driven bremsstrahlung sources have been investigated, whereby the electron beam is generated via laser-wakefield acceleration (LWFA) [22] have been recently reported on (figure 1.3 pink diamond [23]) [5, 24]. The relatively broad divergence and source size limit the peak brightness achievable with this technique. In LWFA, the electrons are forced to undulate by the laser and hence, emit radiation. This 'betatron' radiation (figure 1.3 pink stars [25]) can be extremely bright but without the generation of significantly higher energy electrons, their maximum energy remains capped in the keV regime.

A more promising physical mechanism has been identified in Thompson or Compton scattering; the process is known as Thomson or Compton depending on if quantum effects, like photon recoil, are negligible or not [26] (however, some communities broadly use the term Compton source to refer also to sources exploiting relativistic Thomson scattering [1]). In linear relativistic Thomson scattering (figure 1.3 blue stars [27] and green stars [28]) a high intensity laser is used to scatter off the electrons. This can give a significant boost to the photons incident on those electrons akin to a double Doppler shift. As the laser intensity increases, the mechanism becomes non-linear relativistic Thomson scattering (NLTS, blue stars [29]). In the technique employed in reference [29], the synchronisation issue between the relativistic electrons and ultra-short laser pulse was overcome by using a mirror and reflecting the same driving pulse which generated the electrons back onto them for scattering. This technique is ultimately limited as the pulse will depleted sufficiently as to hamper the true onset of non-linear effects.

From figure 1.3, there is clearly a gap in the community for ultra-bright MeV sources and while in the hard X-ray region (photon energies in the keV regime), the highest peak brilliance is obtained instead with free-electron lasers (10^{25} photons s^{-1} mm^{-2} mrad $^{-2}$ 0.1% BW obtained by PETRA III [30]) with betatron sources peaking at 10^{21} - 10^{22} photons s^{-1} mm^{-2} mrad $^{-2}$ 0.1% BW [25, 31], for MeV applications, one is limited to Bremsstrahlung sources which are unable to achieve the necessary brightness.

The possibility of all-optical and compact Compton sources is on the horizon [26, 32, 33, 34, 35] and the reduction of size from km to cm scale allows for table-top devices which are much more desirable for medical, commercial and security applications. It is

the aim of this thesis to demonstrate the next step to achieving the goal of a compact, ultra-bright source of MeV photons.

1.3 The Need to Develop a New Gamma-Ray Spectrometer

Accurate and efficient detection of high-energy photons is an important area of research for fundamental and applied physics. Currently there are a number of ways of detecting MeV gamma rays, most of which exploiting either Compton scattering or the quantum electromagnetic cascade initiated by the photon in a solid. Compton cameras are compact devices that detect gamma rays by measuring the number of electrons stripped off an atom in the crystal lattice. These free electrons impact onto a scintillator whose photoemission is then collected by a photomultiplier tube and counted. While Compton cameras can give accurate information about flux, they do not give information about the energy of incident photons [36, 37]. On the other hand, the energy of a multi-MeV photon can be measured by detecting the quantum electrodynamic cascade induced during its passage through a material. The size and depth of the cascade yields a direct measurement of the energy of the incident photon [38]. These devices can be extremely accurate but they suffer from the limitation that only single hit events can be precisely resolved.

Detectors have been developed which are able to successfully determine the energy of gamma rays as well as their flux simultaneously. These include the EUROBALL cluster [39] which can spectrally resolve energies up to 10 MeV, and more recently the AFRODITE germanium detector array, which can measure gamma rays with energies up to 20 MeV [40]. Such detectors track the energy of the gamma by looking at its scattering through a volume of germanium. Information from the scattered electrons can be used to reconstruct the energy of the original gamma-ray. While such detectors are able to perform their tasks with great proficiency, the nature of their tracking means that a large number of germanium arrays are used in the device to build up a picture of flux and that increases the volume they occupy, making their implementation in many laboratories infeasible. This means that a new, compact spectrometer which can detect high-energy, high-flux γ-ray beams is required. In this thesis, such a detector will be presented in Chapter 7.

1.4 The Need to Develop New Temporal Overlapping Technique for Intense Laser Systems

Aside from the importance to the production of the next generation of x-ray and γ-ray sources [27, 28, 41, 42, 43, 44] outlined in Section 1.1, multiple laser beam interactions

are progressively attracting the attention of the physics community as they provide a unique scenario for the experimental study of many highly non-linear particle-photon interactions [26], laboratory astrophysics [45], particle acceleration [46, 47] and particle generation [48].

For a meaningful experimental implementation, it is indeed necessary that the high intensity foci of the lasers be spatially and temporally overlapped with a micron and femtosecond scale precision respectively. While spatial overlap is relatively easy to achieve, femtosecond scale temporal overlap is a much harder task, since it lies orders of magnitude below the typical resolution of electronic devices (which respond on the ns to 100's of ps scale). Currently there is no common technique that can be implemented by experimenters who wish to determine the temporal delay present between two ultra-short laser pulses. Hence, there is a need to develop such a technique that can allow for temporal overlap to within a pulse duration. In Chapter 8, a novel technique for temporally overlapping intense laser pulses is presented.

2. PLASMAS AND PARTICLE ACCELERATION

2.1 The Physics of Plasmas

Plasma is a state of matter which can be defined as a "quasineutral gas of charged and neutral particles which exhibits collective behaviour" [49]. Applying this definition, one can see that up to 99% of the visible matter in the universe can be described as being in a plasma state. If one considers a star, with the high temperature and density of the star coupled with the self-sustaining reactions occurring deep within it, a plasma state can easily be formed as atoms become ionised by collisions and photon absorption. A more subtle example of a plasma is that of the interstellar medium, where the intrinsic low density of the medium, means that any ionisations which occur as a result of actions such as Compton scattering from sources such as γ-ray bursts [50], are unlikely to be balanced by subsequent recombination of electron and ion. In both of these examples, if one considers the plasma on the macroscopic scale, neutrality would be observed; however, on the microscopic scale, small differences in the electric fields exist which lead to a collective behaviour unique to the plasma state such as Debye screening and the plasma oscillations [51]. Attention will now be given to defining the Debye length and looking at plasma oscillations.

2.1.1 The Debye Length

Debye screening (or shielding) is a characteristic behaviour unique to plasmas. Considering a plasma as being comprised of free charges both positive and negative, placing a charged sphere into a plasma will cause simultaneous attraction and repulsion of those charged species. As charges with the opposite polarity are biased towards the sphere and those with the same charge polarity move away from it, the sphere becomes 'screened' with respect to an observer. Considering a realistic example of a plasma comprised of electrons with a number density of n_e and heavier ions with a number density of n_i and imposing the condition of quasi-neutrality such that $n_e = Zn_i$, and the ratio of masses is m/M so that the mass of the ions is much greater than that of the electrons, one can begin to understand the effect of the plasma has on potential V introduced to the plasma.

Poissson's equation in one dimension becomes

$$\epsilon_0 \nabla^2 V = \epsilon_0 \frac{d^2V}{dx^2} = -e(Zn_i - n_e) \tag{2.1}$$

For $Z = 1$, $n_i = n_e$ and a density of $n_\infty = n_i$, the in the presence of a potential qV and if the electrons have a temperature T_e then, solving for n_e using the auxiliary equation yields the number density of the electrons

$$n_e = n_\infty \exp(eV/T_e) \tag{2.2}$$

Poisson's equation can now be written as

$$\epsilon_0 \frac{d^2V}{dx^2} = n_\infty \Big[\exp(eV/T_e) - 1\Big] \tag{2.3}$$

From equation 2.3, it can be seen that the bulk dynamics of the plasma are mainly governed by the behaviour of the electrons. Thus, looking at a region where $|eV/T_e| \ll 1$ i.e., looking at a region larger where the potential falls off most rapidly, applying a Taylor approximation yields the result

$$\epsilon_0 \frac{d^2V}{dx^2} = \frac{n_\infty e^2}{T_e} V \tag{2.4}$$

This leads to the definition of an important plasma parameter, the Debye length.

$$\boxed{\lambda_D = \left(\frac{\epsilon_0 T_e}{ne^2}\right)^{1/2}} \tag{2.5}$$

Rather than the familiar fall of electrical potential with r^2, inside a plasma the potential now falls much more rapidly as demonstrated in equation 2.6.

$$V = V_0 \exp(-|x|/\lambda_D) \tag{2.6}$$

The Debye length allows one to determine if collective behaviour will be significant in a substance which may be considered plasma-like. For an ionised gas to be considered a plasma, $\lambda_D \ll L$ where L is the length of the gas in a given direction.

As a consequence, a plasma must possess enough particles within a volume known as a Debye sphere to form a significant charge cloud. In a plasma this condition is met if the number of particles $N_D \gg 1$ where

$$\boxed{N_D = n\frac{4}{3}\pi\lambda_D^3} \tag{2.7}$$

The conditions for plasma size and number density are only two of the defining characteristics of plasmas [49].

2.1.2 Fluid Description of Plasmas

A plasma is by nature a dynamic state of matter involving charged particles. As a result, the electric and magnetic fields present within the plasma must be determined by the position and motion of those charged particles. With a typical plasma having a density of 10^{12} electron-ion pairs per cm^3, the possibility of solving the motion of this numbers is an impossible task; thus, a fluid description is deemed appropriate for describing up to 80% of plasma observed. In the fluid approach, individual particles are neglected and only the motion of fluid elements need be considered [49]. Fluids obey the Navier-Stokes equation given as

$$\rho\left[\frac{\partial \mathbf{u}}{\partial t} + (\mathbf{u}\cdot\nabla)\mathbf{u}\right] = \rho\zeta\nabla^2\mathbf{u} - \nabla p \tag{2.8}$$

Where ρ is the density of the plasma, $\mathbf{u}$ is the velocity of a fluid element, p is the pressure in the plasma and ζ is the kinematic viscosity coefficient of the fluid. In equation 2.8, the $\rho\zeta\nabla^2\mathbf{u}$ represents the collisional term and as one can see, there are no electric or magnetic field descriptions which are of critical importance to the plasma dynamics. Hence, including these terms, equation 2.8 becomes

$$\rho\left[\frac{\partial \mathbf{u}}{\partial t} + (\mathbf{u}\cdot\nabla)\mathbf{u}\right] = en(\mathbf{E} + \mathbf{u}\times\mathbf{B}) - \nabla p - \frac{mn(\mathbf{u}-\mathbf{u_0})}{\tau_{mf}} \tag{2.9}$$

Where $\mathbf{E}$ is the electric field present in the plasma, $\mathbf{B}$ is the ambient magnetic field, $\mathbf{u_0}$ is the velocity of the neutral fluid and τ_{mf} is the mean free time between collisions. In order to simplify the description of the plasma somewhat, it is possible to neglect the final terms if one can consider the plasma 'collisionless' (described in detail later in Section 2.1.4).

2.1.3 The Plasma Frequency

If one considers the motion of an electron in a collsionless plasma with no ambient magnetic field applied and which is in equilibrium, by neglecting the dynamics of the heavier ions (who respond and oscillate much more slowly than their less massive counterparts), the equations of motion for a plasma can be set by using a simplified equation 2.9, the continuity equation for particle conservation and the adiabatic equation of state for tem-

perature dynamics.

$$n_e m_e \frac{\partial \mathbf{u_e}}{\partial t} = q n_e \Big(\mathbf{E} + \mathbf{u_e} \times \mathbf{B} \Big) - \nabla p \tag{2.10a}$$

$$\frac{\partial n_e}{\partial t} + \nabla \cdot (n_e \mathbf{u_e}) = 0 \tag{2.10b}$$

$$\frac{\partial}{\partial t}(p n^{-\xi}) = 0 \tag{2.10c}$$

Where m_e is the mass of the electron, ξ related to the degrees of freedom. In order to solve these, one must consider Maxwell's equations

$$\nabla \cdot \mathbf{E} = \rho / \epsilon_0 \tag{2.11a}$$

$$\nabla \cdot \mathbf{B} = 0 \tag{2.11b}$$

$$\nabla \times \mathbf{E} = -\frac{d\mathbf{B}}{dt} \tag{2.11c}$$

$$\nabla \times \mathbf{B} = \mu_0 \mathbf{J} + \epsilon_0 \mu_0 \frac{d\mathbf{E}}{dt} \tag{2.11d}$$

Here ϵ_0 is the permittivity of free space, μ_0 is the permeability of free space, ρ is the charge density and $\mathbf{J}$ is the current density. From the concept of quasi-neutrality, one can assume that the overall plasma remains neutral but that there will be small spatial and temporal changes on scales less than λ_D which can be described as

$$\begin{aligned} n_e &= n_0 + n_1 \\ p &= p_0 + p_1 \\ \mathbf{E} &= \mathbf{E}_0 + \mathbf{E}_1 \end{aligned} \tag{2.12a}$$

By setting the $T = 0$ (leading to $p = 0$) $B = 0$ and seeking a solution which will be proportional to $\exp[i(\omega t - \mathbf{k}\dot{\mathbf{x}})]$, then from a combination of equations 2.10-2.12

$$m_e i\omega \mathbf{u} = -e\mathbf{E}$$

with the small perturbations in electron number given as

$$n_1 = -\frac{n_0 e}{m_e \omega^2} \nabla \cdot \mathbf{E} \tag{2.13}$$

By substituting in equation 2.11a, the plasma frequency is found to be

$$\boxed{\omega_p^2 = \frac{n_0 e^2}{m_e \epsilon_0}} \tag{2.14}$$

The plasma frequency is implies the presence of oscillations which are in the most part due to electromagnetic forces within the plasma. This behaviour is unique to plasmas and due to it's implications is of great importance for physicists in the field. For an ionised gas to be considered a plasma $T \gg \tau$ where T is the time observing the dynamics and $\tau = 2\pi/\omega_p$.

2.1.4 *Collisionality and Collision-Less Limit*

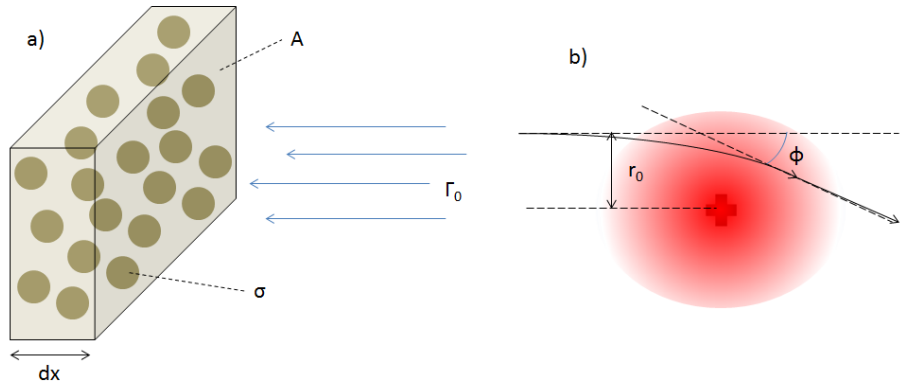

Fig. 2.1: The collisional cross section of electrons on a material slab and the Coloumb collisions.

In general, when an electron collides with an ion, it may lose a fraction of its initial momentum. If there are n_i ions per cm^3, each with a cross-section given by σ, then the flux Γ of electrons propagating through a slab of area A and thickness element dx (as seen in figure 2.1(a))is

$$\Gamma' = \Gamma(1 - n_i \sigma dx) \tag{2.15}$$

This means that Γ is an exponentially decaying term

$$\Gamma = \Gamma_0 e^{-n_i \sigma x} \tag{2.16}$$

Using this, one can see that the mean free path between collisions can be given as $\lambda_{mf} = 1/n_i\sigma$. For an electron with velocity v_e (in the plasma frame of reference) in the x direction, the mean free time $\tau_{mf} = \lambda_{mf}/v_e$. Thus, dropping the subscript i as $n_i = n_e$, the collision frequency

$$\nu_c = n\sigma v_e \tag{2.17}$$

With a plasma described largely as a population of electrons and positively charged ions, the cross section for Coulomb collisions are generally much larger than that of atom-atom interactions occurring in more conventional fluids. Looking at figure 2.1(b), one can see that by simple consideration of the Coulomb force and assuming that the time of

interaction can be simply given as $T = r_0/v_e$, for a collision causing a change of trajectory $\phi \geq 90^o$ the impulse for the interaction becomes

$$\Delta(mv) \approx \frac{e^2}{4\pi\epsilon_0 r_0 v_e} \tag{2.18}$$

From the impulse, and consideration of the cross section ($\sigma = \pi r_0^2$), the collision frequency becomes given in equation 2.17 becomes

$$\nu_c = \frac{ne^4}{16\pi\epsilon_0^2 m v^3} \equiv \frac{\pi n e^4}{(4\pi\epsilon_0)^2 m^{1/2}(KT_e)^{3/2}} \tag{2.19}$$

Here, the electron velocity has been related to the temperature of the plasma for electrons with a Maxwellian distribution $KT_e/m = v^2$ where K is Boltzmann's constant. While this equation describes the large angle collisions, it should be no surprise that the small angle collisions are much more common. Using the Spitzer equation, we need only multiply equation 2.19 by $\ln\Lambda$ to complete the description of the collision frequency. As $\Lambda = \lambda_D/r_0 = 12\pi n\lambda_D^2$, the maximum impact parameter is of course λ_D. This is because the electrons will significantly screen out the ions over long distances.

If one considers a plasma where $2\pi\nu_c \ll \omega_p$, the plasma may be considered 'collisionless' as the effects of collisions are not playing a significant role on the overall plasma dynamics. Looking back at equation (2.19), one can see that collisionless plasmas are likely to be formed if there is a lower number density in the plasma and a high temperature with the later parameter playing a much more significant role in deciding the fact. This is due to the consideration that electron with significant velocity spend a very short amount of time in the cross-section of the ions regardless of their numbers. For collisional plasmas, it is useful to define the resistivity of the plasma.

$$\mathrm{H} = \frac{m}{ne^2}\nu_c = \frac{\pi e^2 m^{1/2}}{(4\pi\epsilon_0)^2(KT_e)^{3/2}}\ln\Lambda \tag{2.20}$$

Unlike conventional solid-state resistors, plasmas are seen to have a resistivity independent of the number of charge carriers. This is because as the number of ions increase, so too does the number of electrons present. The overall result is to cause cancellation of the two effects. This unique property of plasmas means that a sufficient electric field may be applied to the plasma which can accelerate the electron so they never make a collision. There is thus, the possibility of these fast electrons becoming detached from the main body of the distribution [49, 52].

2.2 The Interaction of Electromagnetic Fields with Plasmas

In the previous section, perturbations from the overall neutrality were demonstrated to play a significant role in the dynamics of the plasma. It thus, follows that the propagation of an electromagnetic (EM) wave through a plasma is of significant interest as it responds to the presence of ocsillating EM-fields.

2.2.1 Refractive Index of a Plasma

To simplify the complexity, a wave incident on a collisioness plasma with number density n and no ambient magnetic field can be considered. From Maxwell's equations, specifically substituting 2.11(c) into the time derivative of 2.11(d), one obtains the result

$$c^2\nabla\times(-\nabla\times\mathbf{E_1}) = \frac{1}{\epsilon_0}\frac{\partial\mathbf{J_1}}{\partial t} + \frac{\partial^2\mathbf{E}}{\partial t^2} \tag{2.21}$$

Where the subscript 1 assumes only perturbations from equilibrium. As the description is a wave-like, one can assume solution in the form $\exp[i(\mathbf{k}\cdot\mathbf{r}-\omega t)]$ where ω is the frequency of the incident electromagnetic wave and $\mathbf{k}$ is its wavenumber, meaning equation 2.21 can be linearised to become

$$-\mathbf{k}(\mathbf{k}\cdot\mathbf{E_1}) + k^2\mathbf{E_1} = \frac{i\omega}{\epsilon_0 c^2}\mathbf{J_1} + \frac{\omega^2}{c^2}\mathbf{E_1} \tag{2.22}$$

As the electric field is perpendicular to the first term of the equation becomes zero. Equation 2.10(a) for a plasma with $T = 0$ can also be linearised leading to the solution

$$(\omega^2 - c^2k^2)\mathbf{E_1} = \frac{n_0e^2}{\epsilon_0 m}\mathbf{E_1} \tag{2.23}$$

The right had side of this equation is the plasma frequency; hence, the dispersion relation for electromagnetic waves in plasmas is written as

$$\omega^2 = \omega_p^2 + c^2k^2 \tag{2.24}$$

From equation 2.24, the phase velocity is given as

$$v_\phi^2 = \frac{\omega^2}{k^2} = c^2 + \frac{\omega_p^2}{k^2} > c^2 \tag{2.25}$$

From the phase velocity, the group velocity can be determined as

$$v_g = \frac{d\omega}{dk} = \frac{c^2}{v_\phi} \tag{2.26}$$

From the equation 2.26 it follows that the refractive index of a plasma η is given by the equation

$$\eta = \left(1 - \frac{\omega_p^2}{\omega^2}\right)^{1/2} \tag{2.27}$$

2.2.2 Plasma Skin Depth

From equation 2.27, it can be seen that when $\omega \leq \omega_p$, η becomes imaginary. This indicates that the electrons can respond on a fast enough timescale to screen the plasma from the field of the incident electromagnetic wave. The frequency where $\omega = \omega_p$ is known as the 'critical' frequency. Consequently, can be seen that for each value of ω, there us a 'critical density' above which the plasma prevents further propagation. This is given by

$$n_c = \frac{\omega^2 \epsilon_0 m_e}{e^2} \tag{2.28}$$

If an electromagnetic wave with a frequency lower than the critical frequency is incident on a plasma, it is not simply reflected at the interface of the plasma, rather the wave is attenuated exponentially as $(e^{-x/\delta})$, where δ is the skin depth of the plasma given by

$$\delta = \frac{c}{(\omega_p^2 - \omega)^{1/2}} \tag{2.29}$$

The skin depth gives a useful way for the density of laboratory plasmas to be measured but it also gives a means of coupling electromagnetic energy into a plasma for the purposes of for example, heating it [49] (see Section2.2).

A final plasma parameter to consider is the plasma wavelength. This is given simply by

$$\lambda_p = \frac{2\pi c}{\omega_p} \tag{2.30}$$

The plasma wavelength can give important information regarding the bunch length of electrons that may be created in the plasma.

2.2.3 Coupling Energy into Plasmas by the Action of Electromagnetic Radiation

With the electrons within a plasma responding to the action of electromagnetic waves, it is logical that one can use this action to couple energy into a plasma. This is achieved

by a variety of mechanisms, the most simple mechanism being 'collisional absorption' or 'inverse Bremsstrahlung'. This mechanism can be understood by simplifying the laser field to a plane sine wave which the electron responds to with velocity $u_e = u_{osc}\sin(\omega t)$, transverse to the direction of laser propagation. The energy the electron now has can be transferred to other atoms through collisions. This can cause heating of ions in the plasma or further ionisations [51, 52].

Another method of laser-plasma energy coupling is 'resonance absorption'. This method can be used to couple laser energy into a plasma which is below the critical density. In this case the laser is obliquely incident on the plasma. As oscillations of the electric field are perpendicular to the direction of propagation, the electrons are driven into the ambient plasma, causing local electron densities to approach the critical density. When this occurs, the plasma resonantly excites a wave and as a result, energy is transferred into the plasma. The process gives energy to a relatively small number of the electrons. These 'hot' electrons move through and deposit their energy into the rest of the plasma or material. As this process is dependent on the angle which the laser pulse propagates into the plasma at ($\propto \cos^2\theta$), its effects can be suppressed or enhanced by selection of an of pulse orientation [51, 52]. Many mechanisms by which high-intensity, short pulse electromagnetic radiation is coupled into a plasma are analogous to the resonance absorption mechanism in terms of the density profile steepening [52].

As the intensity of electromagnetic radiation incident on the plasma increases, the individual electrons are forced to oscillate whose spatial variation can be so great that its effects must me considered when describing the electron dynamics. Looking back at equations 2.10a-c, where the temperature is neglected and considering the temporal variation of the electric field as being sinusoidal, the Lorentz force for a single electron is now given as

$$\frac{\partial \mathbf{u_e}}{\partial t} + \mathbf{u_e}\cdot\nabla\mathbf{u_e} = -\frac{e}{m_e}\Big(\mathbf{E}(x)\sin(\omega t)\Big) \tag{2.31}$$

For electrons oscillating in the local electric field transversely to the direction of the laser pulse propagation, the velocity of the electrons is given by

$$\mathbf{u_e} = \frac{e\mathbf{E}(x)}{m_e\omega}\cos(\omega t) \tag{2.32}$$

Averaging the motion over time for high frequency oscillations and substituting equation 2.32 into 2.31, the Lorentz force becomes

$$\begin{aligned} m_e\frac{\partial\langle\mathbf{u_e}\rangle}{\partial t} + m_e\langle\mathbf{u_e}\cdot\nabla\mathbf{u_e}\rangle &= -e\langle\mathbf{E}\rangle \\ m_e\frac{\partial\langle\mathbf{u_e}\rangle}{\partial t} &= -e\langle\mathbf{E}\rangle - \frac{1}{4}\frac{e^2}{m_e\omega^2}\nabla E^2(x) \end{aligned} \tag{2.33}$$

the final term in equation 2.33 is known as the ponderomotive force:

$$\mathbf{F_P} = -\frac{1}{4}\frac{e^2}{m_e\omega^2}\nabla E^2(x) \tag{2.34}$$

The ponderomotive force plays a similar role to thermal pressure in that it can drive electrons out of the regions of high energy density that are caused by the presence of the intense laser field [52]. This mechanism can be used to couple energy directly from an intense laser to a plasma (specifically the electrons of a plasma) and becomes significant when laser intensities exceed 10^{15} Wcm^2 for a 1 μm laser wavelength [51] and as the chirped pulse amplification laser can generate ultra-short pulses (~fs), one can consider the ions as stationary during the laser pulse. This means that an intense laser propagates through a plasma driving electrons forward, a significant potential difference will be present in it's immediate wake.

As laser technology continues to improve, the intensities of which they can achieve increases and the possibility of accelerating an electron to relativistic velocities (energy equal to or above the rest energy of the electron) within one laser time period becomes viable. The a_0, or non-linearity parameter is the ratio of the force of the electric field in a single time period to the rest mass of the electron and is used to define the intensity of a laser in terms of this condition.

$$a_0 = \frac{eE_l^2}{m_e\omega_l} \tag{2.35}$$

Where E_l is the electric field (primarily associated with a laser) and ω_l is the frequency of the radiation. Above unity, the equation indicates that the magnetic component of the Lorentz force will be comparable to the to the electric field component. The behaviour of the electron becomes highly non-linear. If a laser possesses $a_0 \geq 1$, it is said to be relativistically intense. In order to study the behaviour in this state, one must consider the Lorentz factor

$$\gamma = \frac{1}{\sqrt{1 - \frac{u_e^2}{c^2}}} \tag{2.36}$$

Looking at equations 2.34 and 2.35, one can see that $\mathbf{F_P} \sim \nabla a_0^2$; hence, the ponderomotive force begins to dominate the behaviour of the plasma as a_0 increases above unity.

2.2.4 Self-Focussing

As the ponderomotive force results in the attainment of relativistic velocities by the electrons, it follows that modifications to the mass of the electron begin to impact on the

dynamics of the plasma. The plasma frequency in these ranges is modified to become

$$\omega_{p'}^2 = \frac{ne^2}{\gamma \epsilon_0 m_e} \tag{2.37}$$

From equations 2.27 and 2.37, it if clear that the refractive index becomes modified by the action of the intense electromagnetic wave in the plasma. If this effect is localised, result is that the pulse will be slower in the most intense region (centre) while propagating faster in the region of lower intensity (towards the edge of the beam). This caused the plasma to act like a convex lens with the effect itself being known as self-focussing [49, 52, 53].

2.2.5 Self-Phase Modulation

With large electric-fields present within the plasma, one is required to modify the equation for the refractive index beyond the consideration resulting from the increased mass observed in relativistic electrons (η_0). For relativistically intense lasers, one must also consider the second correction so that $\eta = \eta_0 + \eta_2 I$. This modulates the phase according to the equation

$$\phi(x,t) = -\frac{\omega}{c} = \int [\eta_0 + \eta_2 I(x,t)] dx \tag{2.38}$$

However, in the case of a laser pulse, there is also a temporal aspect to consider in the intensity which becomes $I = I_0(x)I(t)$.

$$\Delta\omega = -k_0 \int \frac{\eta_2}{\eta_0} I_0(x) \frac{\partial I(t)}{\partial t} dx \tag{2.39}$$

For laser produced plasmas, the resulting effect is for a blue shift due to the plasma's expansion towards the laser [54].

2.3 Laser Wakefield Acceleration

2.3.1 Plasma Accelerators

Knowledge of the ponderomotoive force and the non-linear behaviour of electrons which occurs at high intensities ($\sim 10^{18}$ Wcm^{-2}), provided inspiration for the plasma based accelerator [55] although the idea of plasmas acting as an accelerating medium preceded this discovery [56]. Plasmas have the unique ability to sustain accelerating gradients of 100's GVm^{-1} and while conventional accelerators would be undergo breakdown due to the large energies required to sustain these potentials, plasmas are not subject such problems (as they already exist in a 'broken-down' state). The potential accelerating

field is determined the equation

$$E_l(\mathrm{V/m}) = \frac{cm_e\omega_p}{e} \tag{2.40}$$

Equation 2.40 shows that increasing the density (proportional to $\omega^{1/2}$) has the potential to produce increasingly large accelerating gradients. This in turn, can reduce the overall size of accelerators from the km scale down to the cm scale. Electrons accelerated in these fields are produced in extremely short bunches in the order of the plasma wavelength (equation 2.30), with durations of τ_p [22]. If a laser has a pulse length $L_l \sim \lambda_p$, then electron bunches can be efficiently created via the LWFA mechanism.

2.3.2 The basic Principle of Laser Wakefield Acceleration

It has been shown in the previous section, that when an ultra-short, relativistically intense laser pulse propagates through an underdense plasma $(\lambda_l/\lambda_p)^2 \ll 1$, the ponderomotive force associated with the laser pulse envelope will drive electrons away from the pulse. If the laser has sufficient intensity to expel the majority of electrons from the focal spot of the laser then a highly charged region of positive charge remains in the wake of the laser. This blowout of the electrons becomes matched to the plasma where $k_p w_0 = 2\sqrt{a_0}$ where w_0 is the laser waste [35]. As the laser continues along it's axis of propagation, the electrons are injected into the positively charged cavity and begin to accelerate through it as shown in figure 2.2.

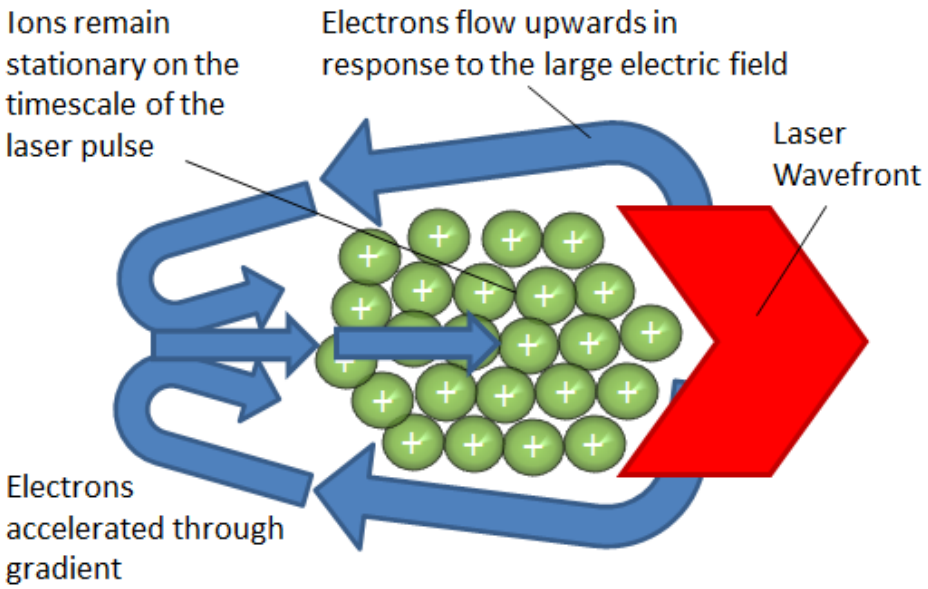

Fig. 2.2: A simplified diagram of the process of LWFA.

This process is continued as the laser propagates through the plasma resulting in a

series of waves being setup which travel with a phase velocity approximately equal to the group velocity of the laser pulse [22]. The result is the creation of a bunch or bunches of electrons with relativistic velocities that can exit the plasma. This effect has been directly observed by optical probes as presented in figure 2.3.

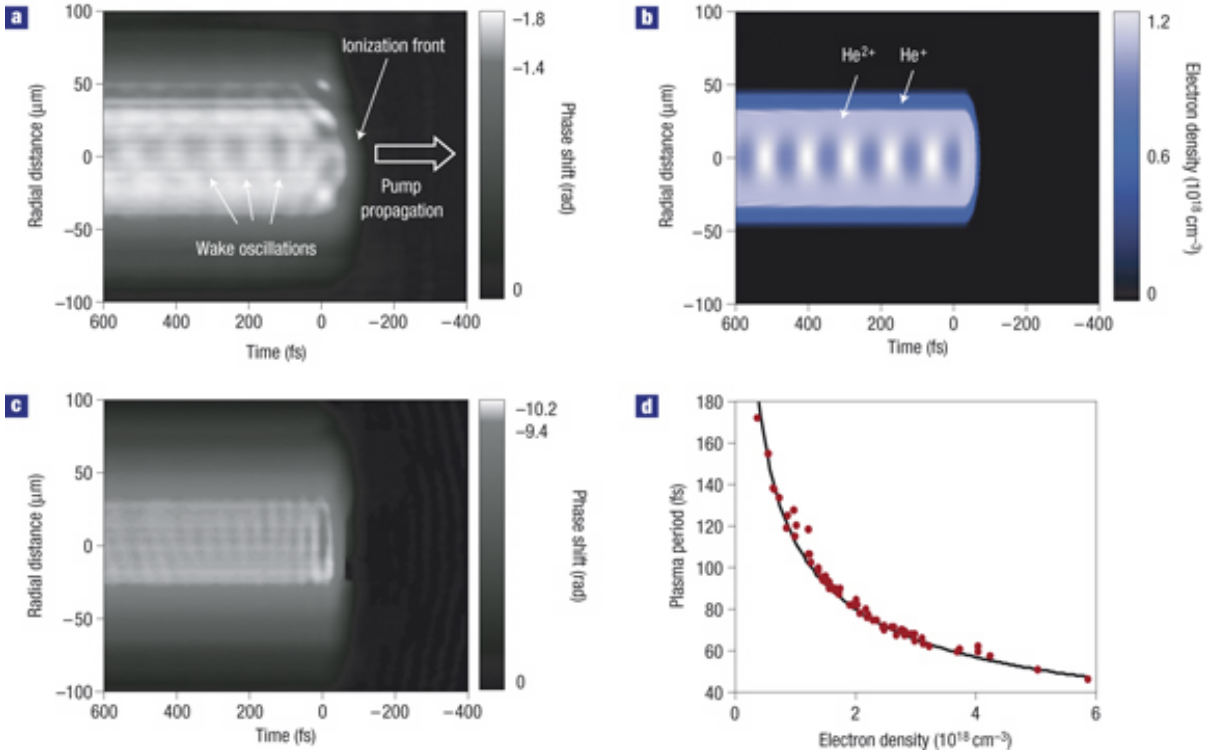

Fig. 2.3: Results obtained in reference [57] where the LWFA is directly observed.

As shown in figure 2.3(a), direct observations of a laser wakefield propagating through a plasma of Helium have been made. The probe phase-shift profile produced by an approx 10 TW, 30 fs pump centred at zero on the horizontal scale for a electron density of $n_e = 0.95 \times 10^{18}$ cm^{-3}, figure 2.3(b)shows the comparison with simulations. Figure 2.3(c) The same observation for an electron density of $n_e = 5.9 \times 10^{18}$ cm^{-3} and figure 2.3(d) gives a comparison of the theoretical and experimental plasma periods obtained [57].

2.3.3 Trapping or Injecting Electrons into the Wakefield

Of course it is not possible to create a channel in which all of the electrons propagate. Electrons are required to be trapped in, or injected into the wake itself. In the most basic example of a laser plasma injector, a single laser pulse is used to self-trap the electron in the plasma it generates in a process known as shock injection. This self-modulated LWFA creates bunches that tend to have large charge ($\approx$ 10 nC) and energy spread characterised by a multi-MeV Boltzmann distribution. The approach employs a large amplitude plasma wakefield. As discussed previously, the intense laser pulse drives the

electrons out of the pulse waist and leaves behind a spherical cavity in which electrons may be injected into [35]. In addition, the ponderomotive force gives momentum to the electrons parallel to the pulse propagation vector. The combined effect is that some of the electons become trapped in the wake of the laser, accelerating towards the pulse. As the velocity for the pulse is lower than it would be in a vacuum, there is a chance that the electrons gain enough kinetic energy to outrun the pulse and cause de-phasing which destroys the wake [22]. Hence, a suitable length and density of gas must be selected.

In order to narrow the energy spread other injection techniques have been suggested. For example using a two-stage gas cell in which the first stage contains a large Z gas such as krypton to generate and shock inject the electron bunches, and a second stage containing a lower Z gas such as helium to create a stable accelerating cavity could result in more stable mono-energetic beams.

Another injection technique is ponderomotive injection in which an initial laser pulse creates the bubble and a second pulse shortly after this, injects electrons into the cavity. Another method is the colliding pulse injection where injection results due to the slow beat wave of the two interacting pulses which are counter-propagating. This process may make the level of acceleration and hence, the electron energy, tunable. Both of these techniques are arguably more technically challenging but may be the next step in beam quality.

3. SYNCHROTRON RADIATION AND THE UNDULATOR AND WIGGLER

It is a well establish phenomena that an accelerating charge will emit electromagnetic radiation. When a particle moves with a constant velocity in a circular arc, the term 'synchrotron radiation' is considered apt. Qualitatively, synchrotron radiation has its origin in the fact that if an electron moves with relativistic velocity (kinetic energy greater than or equal to the rest mass of the electron) towards an observer, the radiation emitted propagates at a velocity comparable to the electron; hence, the fields are created by the charge over a much longer time than the time taken to receive them. It is this time compression that determines the spectrum of the synchrotron radiation. In order to describe the radiation emitted by a relativistic electron and correspondingly, relate radiation observed back to the electron motion, one must invoke the retarded potentials and fields which is discussed in this chapter [58].

3.1 The Fields of a Dynamic Electron

3.1.1 Charge Motion and Retarded Time

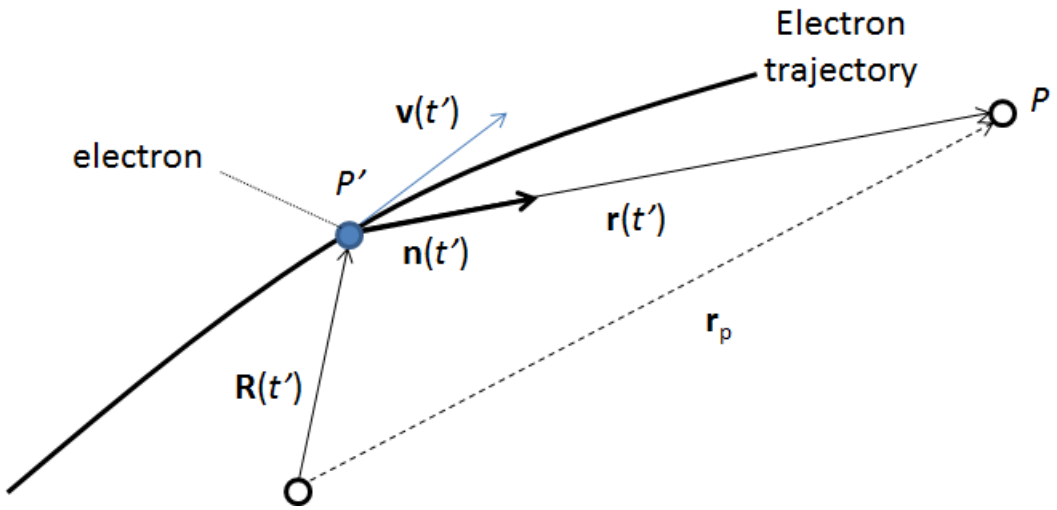

Fig. 3.1: Electron with trajectories with respect to an observer [58].

In this section, the approach followed will closely match those outlined in the book

'The Physics of Synchrotron Radiation' and references contained therein (A. Hofmann 2004 [58]). Consider an electron moving with a velocity on a particular trajectory as in figure 3.1. If an observer at a point P is to calculate the fields measured at a time t, the position and motion of the charge at the earlier time of t' must be known. The electron travelling on this trajectory with a displacement from origin (O) given by $\mathbf{R}(t')$, with a position P' at time t', has an electric field $\mathbf{E}$ and generates a magnetic field $\mathbf{B}$. For the observer at point P, the vector $\mathbf{r}_p$ (with absolute value r) points from O to P, while the vector $\mathbf{r}(t')$ points from the electron at P' to P. At time t, the observer will receive the field that propagated with finite velocity c at the earlier time of t' (see figure 3.1). The relationship between these factors is given by

$$t = t' + \frac{r(t')}{c} \tag{3.1}$$

This means that prior knowledge of the electron's position and velocity ($\mathbf{u_e}(t') = \mathbf{R}/dt'$) of the electron at t'. As the pointing vector from the origin ($\mathbf{r}_p$) is fixed, then it can be stated that

$$\mathbf{R}(t') + \mathbf{r}(t') = \mathbf{r}_p = \text{constant} \tag{3.2}$$

Differentiating equation 3.2 with respect to t' yields the relation to the change of $\mathbf{r}$

$$\frac{d\mathbf{r}(t')}{dt'} = -\frac{d\mathbf{R}}{dt'} = -\mathbf{v} = -\boldsymbol{\beta}(t') \tag{3.3}$$

As $\mathbf{r}$ is an absolute quantity it can be shown that

$$\mathbf{r}\frac{d\mathbf{r}}{dt'} = \frac{1}{2}\frac{d\mathbf{r}^2}{dt'} = r\frac{dr}{dt'} = -(\mathbf{r}\cdot\mathbf{v}) \tag{3.4}$$

If the unit vector $\mathbf{n} = \mathbf{r}/r$ is introduced, then equation 3.4 gives the relative velocity to the observer as

$$\frac{dr}{dt'} = -(\mathbf{n}\cdot\mathbf{v} = -c(\mathbf{n}\cdot\boldsymbol{\beta})) \tag{3.5}$$

The relationship between time and the retarded time is now given as

$$\boxed{dt = \left(1 + \frac{1}{c}\frac{dr}{dt'}\right)dt' = (1 - \mathbf{n}\cdot\boldsymbol{\beta})dt'} \tag{3.6}$$

3.1.2 Retarded Electromagnetic Fields

With equation 3.6 establishing the retarded time, it is now possible to determine the electromagnetic potentials ($V(t)$ for electric potential and $\mathbf{A}(t)$ for magnetic potential, where the Lorentz convention $\nabla \cdot \mathbf{A} = -\dot{V}/c^2$ is used) that will be observed at P by the charge. Equations 2.11 show Maxwell's equations. Modifying these to determine the show the relation of the potentials to the electromagnetic fields

$$\mathbf{E} = -\nabla V - \frac{\partial \mathbf{A}}{\partial t} \tag{3.7a}$$

$$\mathbf{B} = [\nabla \times \mathbf{A}] \tag{3.7b}$$

From equations 3.7, it is clear that the electromagnetic potentials are both time dependant. With charge density $\rho(t')$ and current density $\mathbf{J}(t')$, the potentials can be given as

$$\begin{aligned} V(t) &= \frac{1}{4\pi\epsilon_0} \int \frac{\rho(t')}{r(t')} dx'dy'dz' \\ \mathbf{A}(t) &= \frac{\mu_0}{4\pi} \int \frac{\mathbf{J}(t')}{r(t')} dx'dy'dz' \end{aligned} \tag{3.8}$$

As an electron has elementary charge e and radius b, the field can be considered to have been emitted over the time the electron was stationary i.e., $\Delta t'_0 = 2b/c$ which is constant. As the electron is moving with $\mathbf{v}$, which has a component of $v_r = \mathbf{n} \cdot \mathbf{v}$ towards the observer. This means that it contributes to the field over a time $\Delta t'_v = 2b/(c(1 - \mathbf{n} \cdot \boldsymbol{\beta}))$. The ratio between $\Delta t'_v$ and $\Delta t'_0$ is $(1 - \mathbf{n} \cdot \boldsymbol{\beta})^{-1}$ and the potentials become

$$V(t) = \frac{e}{4\pi\epsilon_0} \frac{1}{r(t')(1 - \mathbf{n}(t') \cdot \boldsymbol{\beta}(t'))} \tag{3.9a}$$

$$\mathbf{A}(t) = \frac{\mu_0 e}{4\pi} \frac{\mathbf{v}(t')}{r(t')(1 - \mathbf{n}(t') \cdot \boldsymbol{\beta}(t'))} \tag{3.9b}$$

By dropping the notation t' from these equations, the Liénard-Wiechert potentials are given. As expected, these potentials decay with $1/r$.

$$V = \frac{e}{4\pi\epsilon_0} \left\{ \frac{1}{r(1 - \mathbf{n} \cdot \boldsymbol{\beta})} \right\}_{\text{ret}} \tag{3.10a}$$

$$\mathbf{A}(t) = \frac{\mu_0 e}{4\pi} \left\{ \frac{\mathbf{v}}{r(1 - \mathbf{n} \cdot \boldsymbol{\beta})} \right\}_{\text{ret}} \tag{3.10b}$$

From equations 3.7, one can substitute the retarded potentials given in equation 3.10. Once again, the retarded time becomes relevant to the discussion. As $dt = (1 - \mathbf{n} \cdot \boldsymbol{\beta})dt'$,

one can let

$$\frac{\partial \mathbf{A}}{\partial t} = \frac{dt'}{dt}\frac{\partial \mathbf{A}}{\partial t'} = \frac{1}{1-\mathbf{n}\cdot\boldsymbol{\beta}}\frac{\partial \mathbf{A}}{\partial t'}$$

So the derivative of the vector potential $\mathbf{A}$ with respect to t is written as

$$\frac{\partial \mathbf{A}}{\partial t} = \frac{\mu_0 ec}{4\pi}\frac{1}{(1-\mathbf{n}\cdot\boldsymbol{\beta})}\left(\frac{\dot{\boldsymbol{\beta}}}{r(1-\mathbf{n}\cdot\boldsymbol{\beta})} - \frac{\boldsymbol{\beta}\partial(r-\mathbf{r}\cdot\boldsymbol{\beta})/\partial t'}{r^2(1-\mathbf{n}\cdot\boldsymbol{\beta})^2}\right) \tag{3.11}$$

$\partial(r-\mathbf{r}\cdot\boldsymbol{\beta})/\partial t'$ given by $-c(\mathbf{n}\cdot\boldsymbol{\beta}) + c\beta^2 - \mathbf{r}\cdot\dot{\boldsymbol{\beta}}$ meaning equation 3.11 becomes

$$\frac{\partial \mathbf{A}}{\partial t} = \frac{\mu_0 ec}{4\pi}\left\{\frac{\dot{\boldsymbol{\beta}}}{r(1-\mathbf{n}\cdot\boldsymbol{\beta})^2} + \frac{c(\mathbf{n}\cdot\boldsymbol{\beta}) - c\beta^2 + (\mathbf{r}\cdot\dot{\boldsymbol{\beta}})}{r^2(1-\mathbf{n}\cdot\boldsymbol{\beta})^3}\boldsymbol{\beta}\right\}_{ret} \tag{3.12}$$

To determine the retarded electric field from equation 3.7, one requires the gradient of the scalar potential ∇V.

$$\nabla V = \frac{e}{4\pi\epsilon_0}\nabla\left(\frac{1}{r(1-\mathbf{n}\cdot\boldsymbol{\beta})}\right) = \frac{e}{4\pi\epsilon_0}\frac{\nabla(r-\mathbf{r}\cdot\boldsymbol{\beta})}{r^2(1-\mathbf{n}\cdot\boldsymbol{\beta})^2} \tag{3.13}$$

With the electron generating a field over a time interval in which the observers position is changing, a new level of complexity is introduced and shown in figure 3.2.

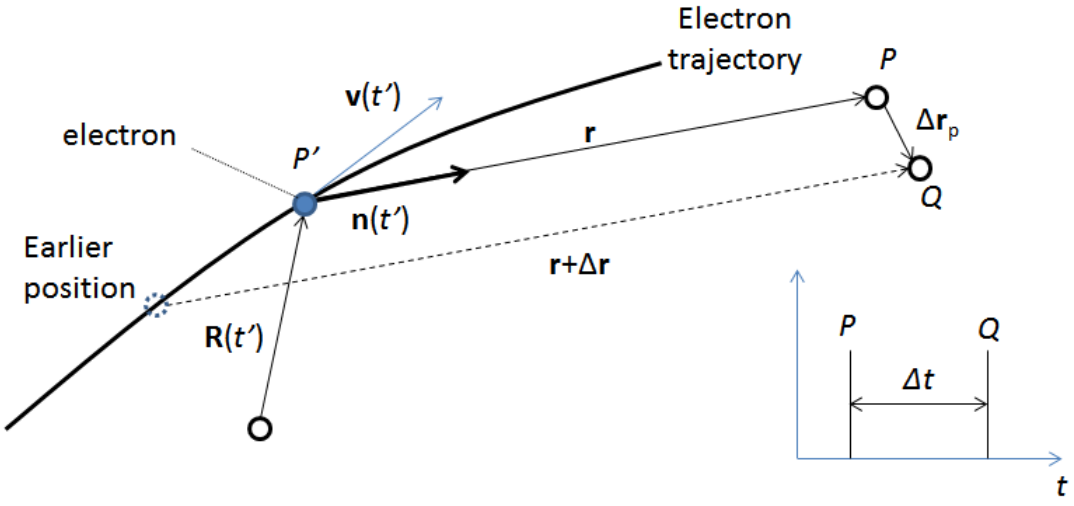

Fig. 3.2: The electron trajectory and the subsequent modifications made over a small time element Δt [58].

The term $\nabla V \cdot \Delta\mathbf{r}_p$ describes this change occurring in the time period t' where $\Delta\mathbf{r}_p$ is the change in position. The displacement vector from the electron at the time of the observer P of $\mathbf{r}$ but at some earlier time, it occupied a position which gives a displacement vector to

a second observer placed at Q, of $\mathbf{r}+\Delta\mathbf{r}$. If the observers are separated by a displacement of $\Delta\mathbf{r}_p$ and observer two photons at the same time t, there are two contributions to the change in the position of the fields; the separation in space of the observers $\Delta\mathbf{r}_p$ and the change in the times that the photons were first generated due to the difference in the displacements to the respective observers $\Delta\mathbf{r} = (\partial\mathbf{r}/\partial t')\Delta t'$.

With $(\partial\mathbf{r}/\partial t') = -c\boldsymbol{\beta}$, Δr is defined written as

$$\Delta\mathbf{r} = \Delta\mathbf{r}_p - c\boldsymbol{\beta}\Delta t'$$

rearranging this for $\Delta t'$ and comparing with $\Delta t' = \nabla t'\Delta\mathbf{r}$, we can determine the gradient of t' to be

$$\nabla t' = -\frac{\mathbf{n}}{c(1-\mathbf{n}\cdot\boldsymbol{\beta})} \tag{3.14}$$

Looking at the denominators of equations 3.10(a & b)

$$\begin{aligned}\Delta(r-\mathbf{r}\cdot\boldsymbol{\beta}) &= \Delta r - \Delta\mathbf{r}\cdot\boldsymbol{\beta} - r - \Delta\mathbf{r}\cdot\Delta\boldsymbol{\beta}\\ &= -c\Delta t' - (\Delta\mathbf{r}_p\cdot\boldsymbol{\beta}) + x\beta^2\Delta t' - (\mathbf{r}\cdot\dot{\boldsymbol{\beta}})\Delta t'\end{aligned}$$

$$\Delta(r-\mathbf{r}\cdot\boldsymbol{\beta}) = \left(-\boldsymbol{\beta} + \frac{(1-\beta^2)c + (\mathbf{r}\cdot\dot{\boldsymbol{\beta}})}{c(1-\mathbf{n}\cdot\boldsymbol{\beta})}\mathbf{n}\right)\Delta\mathbf{r}_p \tag{3.15}$$

Using this equation, the comparison $\Delta(r-\mathbf{r}\cdot\boldsymbol{\beta}) = \nabla(r-\mathbf{r}\cdot\boldsymbol{\beta})\cdot\Delta\mathbf{r}_p$ is used to alter the scalar potential V given in equation 3.10 to

$$\nabla V = -\frac{e}{4\pi\epsilon_0}\left(\frac{\nabla r(1-\mathbf{n}\cdot\boldsymbol{\beta})}{r^2(1-\mathbf{n}\cdot\boldsymbol{\beta})^2}\right) \tag{3.16}$$

Rearranging the comparison of equation 3.15 into the one above and including equation 3.12, equation 3.7 can now yield an equation for the retarded electric field.

$$\mathbf{E} = \frac{e}{4\pi\epsilon_0}\left\{\frac{(1-\beta^2)(\mathbf{n}-\boldsymbol{\beta})}{r^2(1-\mathbf{n}\cdot\boldsymbol{\beta})^3} + \frac{(\mathbf{n}\cdot\dot{\boldsymbol{\beta}})(\mathbf{n}-\boldsymbol{\beta}) - (1-\beta^2)(1-\mathbf{n}\cdot\boldsymbol{\beta})\dot{\boldsymbol{\beta}}}{cr(1-\mathbf{n}\cdot\boldsymbol{\beta})^3}\right\}_{\text{ret}} \tag{3.17}$$

To simplify this equation , the triple vector product is employed and equation 3.17 becomes

$$\boxed{\mathbf{E}(t) = \frac{e}{4\pi\epsilon_0}\left\{\frac{(1-\beta^2)(\mathbf{n}-\boldsymbol{\beta})}{r^2(1-\mathbf{n}\cdot\boldsymbol{\beta})^3} + \frac{([\mathbf{n}\times[(\mathbf{n}-\boldsymbol{\beta})\times\dot{\boldsymbol{\beta}}]]}{cr(1-\mathbf{n}\cdot\boldsymbol{\beta})^3}\right\}_{\text{ret}}} \tag{3.18}$$

Equation 3.18 is the Liénard Wiecnhert expression for describing the electric field of a moving charge.

For the magnetic field, taking the curl of equation 3.10(b) and applying the relation $[\nabla \times (a\mathbf{C})] = a[\nabla \times \mathbf{C}] + [\nabla a \times \mathbf{C}]$, the magnetic field can be determined. $[\nabla \times \mathbf{A}]$ becomes

$$[\nabla \times \mathbf{A}] = -\frac{\mu_0 ec}{4\pi}\left(\frac{[\nabla \times \boldsymbol{\beta}]}{r(1-\mathbf{n}\cdot\boldsymbol{\beta})} - \frac{\nabla(r-\mathbf{r}\cdot\boldsymbol{\beta})\times\boldsymbol{\beta})}{r^2(1-\mathbf{n}\cdot\boldsymbol{\beta})^2}\right) \tag{3.19}$$

Because the velocity is dependant on the observer (see figures 3.1 & 3.2), a similar argument is used as was previously that allows one to write: $\Delta\boldsymbol{\beta} = \dot{\boldsymbol{\beta}}\Delta t'$. This gives the magnetic field to be

$$\mathbf{B}(t) = \frac{\mu_0 ec}{4\pi}\left\{\frac{(1-\beta^2)(\mathbf{n}\times\boldsymbol{\beta})}{r^2(1-\mathbf{n}\cdot\boldsymbol{\beta})^3} + \frac{(\mathbf{n}\cdot\dot{\boldsymbol{\beta}})[\mathbf{n}\times\boldsymbol{\beta}] + (1-\mathbf{n}\cdot\boldsymbol{\beta})[\mathbf{n}\times\dot{\boldsymbol{\beta}}]}{cr(1-\mathbf{n}\cdot\boldsymbol{\beta})^3}\right\}_{\text{ret}} \tag{3.20}$$

This can be related back to the electric field to give

$$\boxed{\mathbf{B}(t) = \frac{[\mathbf{n}_{\text{ret}}\times\mathbf{E}]}{c}} \tag{3.21}$$

Equation 3.21 is the Liénard Wiecnhert expression for describing the magnetic field of a moving charge. As can be seen and of course, expected, the magnetic field is perpendicular to the electric field and the vector $\mathbf{n}_{\text{ret}}$. It can be seen that for a case where the electron is at rest, Coulomb's law is recovered from equation 3.18 and $\mathbf{B} = 0$ is recovered from equation 3.21. Now however, when $\dot{\boldsymbol{\beta}} \neq 0$, the second term of equation 3.18 increases. It is useful to divide equation 3.18 into two parts, the near field which does not require an acceleration and the far field which does. Only the second term contributes to radiation observed at a distance and this allows one to simplify Liénard Wiecnhert equation to become [58].

$$\mathbf{E}(t) = \frac{e}{4\pi\epsilon_0}\left\{\frac{[\mathbf{n}\times[(\mathbf{n}-\boldsymbol{\beta})\times\dot{\boldsymbol{\beta}}]]}{cr(1-\mathbf{n}\cdot\boldsymbol{\beta})^3}\right\}_{\text{ret}} \tag{3.22}$$

With the establishment of the Liénard Wiecnhert equations for the time dependant electric and magnetic fields due to a relativistic electron, it is possible to predict the spectra of photons emitted.

3.2 Spectrum and Power of Emitted Radiation in the Case of Relativistic Acceleration

Radiation emitted from an accelerating electron has been shown to be caused by variations in the relevant electric field describing it's far field given in equation3.22. Using this and

equation 3.21 (while dropping the notation 'ret'), the power flux can be obtained via the Poynting vector.

$$\mathbf{S} = \frac{1}{\mu_0}[\mathbf{E} \times [\mathbf{n} \times \mathbf{E}]] = \frac{1}{\mu_0}\Big(E^2\mathbf{n} - (\mathbf{n} \cdot \mathbf{E})\mathbf{E}\Big) \tag{3.23}$$

And with $\mathbf{E} \cdot \mathbf{n} = 0$, the pointing vector becomes

$$\mathbf{S} = \frac{E^2}{\mu_0 c}\mathbf{n} \tag{3.24}$$

It is important to note at this stage that the fields that were derived in the previous section were the ones seen by an observer at a observed time t. This means that the Poynting vector is a representation of the energy (U) received by the observer per unit area per unit time interval Δt. This explains the Poynting vector only having a radial component $S_r = \mathbf{n} \cdot \mathbf{S}$.

$$\mathbf{S} = \frac{1}{r^2}\frac{d^2U}{d\Omega dt}\mathbf{n} = \frac{1}{r^2}\frac{dP}{d\Omega}\mathbf{n} \tag{3.25}$$

As the Poynting vector gives the rate of energy transfer per unit area (specifically here in the time interval $\Delta t'$), the irradiated power per unit solid angle becomes

$$\frac{dP}{d\Omega} = \frac{d^2U}{d\Omega dt'} = \frac{d^2U}{d\Omega dt}\frac{dt}{dt'} = \frac{r^2\,|\mathbf{E}|^2}{\mu_0 c}(1 - \mathbf{n} \cdot \beta) \tag{3.26}$$

The integration of equation 3.26 with respect to time and angle yields the energy emitted [58]

$$U = \frac{r^2}{\mu_0 c}\int_{-\infty}^{+\infty} dt \int_0^{2\pi} d\phi \int_{-\pi/2}^{\pi/2} E^2(t)\sin\theta d\theta \tag{3.27}$$

3.2.1 Angular Distribution

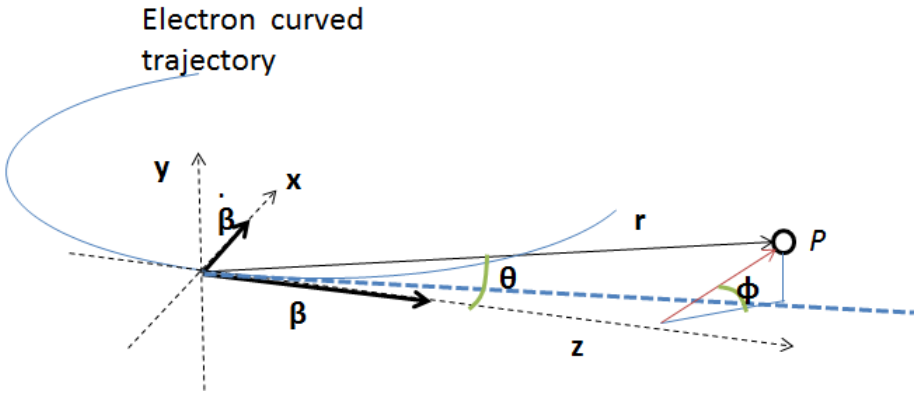

Fig. 3.3: The curved trajectory of the electron moving in a constant magnetic field [58].

In order to determine the angular distribution of the radiation emitted by an accelerating electron, the simple example of circular motion is taken (see figure 3.3). Consider an electron moving in a magnetic field of strength $\mathbf{B}$; the radius of curvature ρ is given by the equation

$$\frac{1}{\rho} = \frac{e\mathbf{B}}{m_e c\beta\gamma} \tag{3.28}$$

If the electron has velocity $\boldsymbol{\beta}$ in the z direction with acceleration $\dot{\boldsymbol{\beta}}$ in the x direction, an observer at a point P along the vector $\mathbf{r}$ with angles θ and ϕ relative to the electron, then equation 3.22 can be used to determine the radiation field. In spherical coordinates, this becomes

$$\begin{aligned}\mathbf{E}_{[\theta,\phi,r]}(t) &= \frac{e}{4\pi\epsilon_0 c}\left\{\frac{[\mathbf{n}\times[(\mathbf{n}-\boldsymbol{\beta})\times\dot{\boldsymbol{\beta}}]]}{r(1-\mathbf{n}\cdot\boldsymbol{\beta})^3}\right\} \\ &= -\frac{e\beta^2}{4pi\epsilon_0 r\rho}\times\frac{[(\cos\theta-\beta)\cos\phi, -\sin\phi(1-\beta\cos\theta), 0]}{(1-\beta\cos\theta)^3}\end{aligned} \tag{3.29}$$

This gives an angular power distribution of

$$\frac{dP_T}{d\Omega} = \frac{e^2\dot{\boldsymbol{\beta}}^2}{(4\pi)^2\epsilon_0 c}\frac{(1-\beta\cos)^2-(1-\beta^2)\sin^2\theta\cos^2\phi}{(1-\beta\cos\theta)^5} \tag{3.30}$$

An integration of equation 3.30 over the full solid angle gives the total power to be

$$P_{T0} = \frac{2e^2\dot{\boldsymbol{\beta}}^2\gamma^4}{12\pi\epsilon_0 c} \tag{3.31}$$

Meaning that equation 3.30 becomes

$$\frac{dP_T}{d\Omega} = \frac{3P_{T0}}{8\pi\gamma^4}\frac{(1-\beta\cos)^2-(1-\beta^2)\sin^2\theta\cos^2\phi}{(1-\beta\cos\theta)^5} \tag{3.32}$$

The consequences of this is that as β increases, the distribution begins to peak in the forward direction. It can be seen from equation 3.32 that there at the angle where $\sin\phi = 0$, no radiation will be emitted. This means that the radiation will be contained in a cone of angle $\theta_0 = \cos^{-1}\beta$ or in the ultra-relativistic case

$$\theta_0(\gamma\to\infty) = 1/\gamma \tag{3.33}$$

In the ultra-relativistic case, it can be useful to repeat the steps above with approxima-

tions of

$$\beta \approx 1 \text{ and } \gamma \gg 1$$

leading to

$$\mathbf{E}_{[\theta,\phi,r]}(t) = -\frac{e\gamma^4}{\pi\epsilon_0 r\rho}\frac{[(1-\gamma^2\theta^2)\cos\phi, -(1+\gamma^2\theta^2)\sin\phi, 0]}{(1-\gamma^2\theta^2)^3} \tag{3.34}$$

The emitted radiation in the forward direction only has an x-component. The total radiated power of the electron becomes

$$P_{T0} = \frac{2ce^2\gamma^4}{12\pi\epsilon_0\rho^2} \tag{3.35}$$

Which allows the angular power distribution to be expressed as

$$\frac{dP_T}{d\Omega} = \frac{3P_{T0}\gamma^2}{\pi}\frac{1-\gamma^2\theta^2\cos(2\phi)+\gamma^4\theta^4}{(1+\gamma^2\theta^2)^5} \tag{3.36}$$

Clearly there is a strong dependence on the Lorentz factor of the electron emitting the radiation. An integration over the solid angle yields the results that the opening angle becomes $\theta = 1/\gamma$ [58].

3.2.2 Synchrotron Spectrum

In order to determine the spectrum received by an observer from an accelerating charge, one must take the inverse Fourier transform of this equation. Hence, this is written as

$$\tilde{\mathbf{E}}(\omega) = \frac{1}{\sqrt{2\pi}}\int_{-\infty}^{\infty}\mathbf{E}(t)e^{-i\omega t}dt \tag{3.37}$$

Which becomes

$$\tilde{\mathbf{E}}(\omega) = \frac{e}{4\pi\epsilon_0}\frac{1}{\sqrt{2\pi}}\int_{-\infty}^{\infty}\left(\frac{[\mathbf{n}\times[(\mathbf{n}-\boldsymbol{\beta})\times\dot{\boldsymbol{\beta}}]]}{cr(1-\mathbf{n}\cdot\boldsymbol{\beta})^3}\right)e^{-i\omega(t'+r(t')/c)}dt' \tag{3.38}$$

If the observer is at a sufficient distance away so that $r \gg 2\rho/\gamma$ (where ρ is the radius of curvature of the electron trajectory), with for the ultra-relativistic case where $\gamma \gg 1$ the

integration becomes

$$\tilde{\mathbf{E}}(\omega) = \frac{i\omega e}{4\pi\sqrt{2\pi}\epsilon_0 cr}\int_{-\infty}^{\infty}[\mathbf{n}\times[\mathbf{n}\times\boldsymbol{\beta}]]e^{-i\omega(t'+r(t')/c)}dt' \tag{3.39}$$

In order to determine the angular power density spectrum, the synchrotron energy equation 3.27 is integrated over the solid angle; however, this time equation 3.37 is substituted in, in order to determine the angular distribution of the emitted spectrum. As this yields the result

$$\frac{dU}{d\Omega} = \frac{r^2}{\mu_0 c}\int_{-\infty}^{+\infty}\left|\tilde{\mathbf{E}}(\omega)\right|^2 d\omega = \frac{2r^2}{\mu_0 c}\int_{0}^{+\infty}\left|\tilde{\mathbf{E}}(\omega)\right|^2 d\omega \tag{3.40}$$

Differentiating equation 3.40 with respect to ω gives the angular spectral energy distribution

$$\frac{d^2U}{d\Omega d\omega} = \frac{2r^2\left|\tilde{\mathbf{E}}(\omega)\right|^2}{\mu_0 c} \tag{3.41}$$

Equation 3.41 gives the energy that is received by an observer per unit frequency per unit solid angle. It can be noted that the time t does not appear in the equation. Extracting the timing information from this is quite difficult however, if the energy radiated per unit time is on average a constant like it would be for a particle in a closed circular orbit (or later in an oscillating system), this is a useful quantity to determine [58].

While the energy spectra are useful to obtain, it is important to relate this to the quanta of radiation. With the energy of photons given by $E_\gamma = \hbar\omega$, where $\hbar$ is planks constant divided by 2π, one can begin to look at the spectra in terms of photon numbers. For the power element $dP(\omega)$ centred around ω in the interval $d\omega$

$$dP(\omega) = E_\gamma d\dot{\mathrm{N}} \tag{3.42}$$

Here, as $d\dot{\mathrm{N}}$ is the number of photons emitted per second, once the power spectrum is determined, it becomes more straight-forward to predict the number of photons emitted in a particular bandwidth.

3.3 Emission of Undulator and Wiggler Systems and the Analogy to Synchrotron Radiation

Up to now, a case has been presented in which an electron is moving in circular motion but this need not be the case for the expressions to be valid. Any accelerating force on

a charge can be given a similar treatment with a few modifications. In the derivations given previously, emission was considered over a short duration which represented a small portion of the overall motion of the electron in it's orbital trajectory. Now the case which the electron moves along a straight trajectory along which it undulates will be considered.

In general, an undulator is a spatially periodic magnetic structure designed to produce a quasi-monoenergetic spectrum of synchrotron radiation from a relativistic bunch of charge (electrons). However, any system that can cause a periodic oscillation of the electron as it propagates can be considered analogus to the original undulator setup.

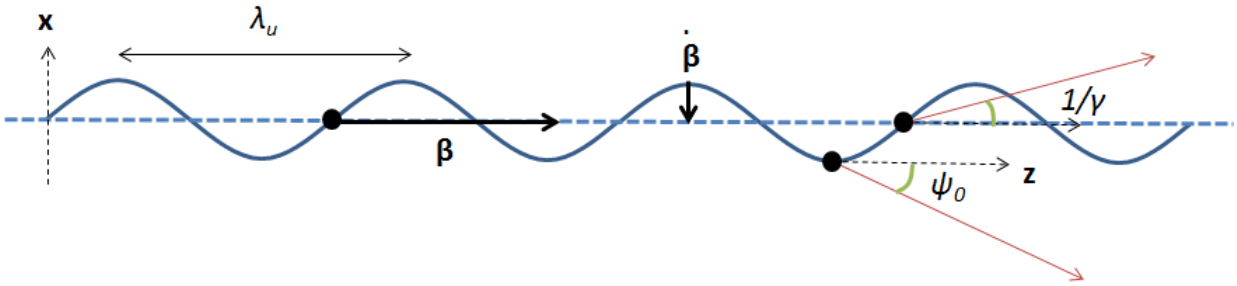

Fig. 3.4: An electron undulates with amplitude in the x axis as it propagates along the z axis [58].

Figure 3.4 shows the characteristic motion of an electron with velocity $\boldsymbol{\beta}$ which is oscillating as it propagates along the z axis. The restoring acceleration is in the x axis and is given by $\dot{\boldsymbol{\beta}}$. The spatial period of oscillation is given by λ_u. The maximum deflection angle with respect to the z axis is given by ψ_0. The ratio of ψ_0 compared with the natural deflection angle given in equation3.33 $(1/\gamma)$ gives the undulator strength parameter $K_u = \gamma\psi_0$. If $K_u < 1$ then the value of ψ_0 is lower than the value of the natural opening angle and the system is said to be in the undulator regime. If $K_u > 1$ then the value of ψ_0 is larger than the value of the natural opening angle and the emission is in the wiggler regime [35, 58].

3.3.1 Unduators

With $\psi_0 < 1/\gamma$, an electron which traverses an undulator setup emits a smoothly modulated field with quasi-monoenergitic properties. In the ultra-relativistic case, it can be straightforward to determine the energy of photons emitted in the undulator regime. Considering an electron which is driven to oscillate by a magnetic fields spaced as described above so that $\mathbf{B} = B_0[0, \cos(k_u z), 0]$, the equation of motion is given as

$$\mathbf{F} = e[\mathbf{v} \times \mathbf{B}] = m_e\gamma[\ddot{x}, \ddot{y}, \ddot{z}] = eB_0[-\cos(k_u)\dot{z}, 0, cos(k_u z)\dot{x}], \tag{3.43}$$

Hence, two differential equations can be formed

$$\frac{d^2x}{dt'^2} = -\frac{eB_0}{m_e\gamma}\cos(k_u)\dot{z}, \qquad \frac{d^2z}{dt'^2} = -\frac{eB_0}{m_e\gamma}\cos(k_u)\dot{x} \tag{3.44}$$

which upon integration of the first equation gives

$$\dot{x} = -\frac{eB_0}{m_e\gamma k_u}\sin(k_u) = -\frac{cK_u}{\gamma}\sin(k_u z) \tag{3.45}$$

Consideration of the conservation of energy, can yield the result

$$\dot{z} = \beta c\sqrt{1 - \frac{\dot{x}^2}{\beta^2 c^2}} \tag{3.46}$$

This is an obvious result as c is a limiting factor of the velocity, any acceleration in the x direction will cause a reduction in the velocity in the z direction.

As the undulator regime deals with only small periodic perturbations from the electrons initial trajectory, $\dot{x}$ is small and equation 3.46 can be approximated to $\dot{z} \approx \beta c$. As a result, the angle of emission in this regime remains at $\psi_0 \approx 1/\gamma$. In addition, with $\dot{z} \approx \beta c$, one can write $z = \beta c t'$.

With these approximations, the treatment of the time varying fields remains largely consistent with that of those obtained for synchrotron emission. As the periodicity of the electron in the undulator is given as $2\pi\beta c/\lambda_u = \Omega_u$ and for the ultra-relativistic case, the frequency of photons emitted becomes

$$\omega = \frac{2\gamma^2}{1 + \gamma^2\theta^2}\Omega_u \tag{3.47}$$

For determining the number of photons emitted per electron in an undulator scenario, again the treatment is similar to that of in the previous section. This time however, the number of photons produced is twice that of those presented in equation 3.42 due to the electron having two observable phases of acceleration within a single oscillation $\dot{\mathrm{N}} = 2P(\omega)/E_\gamma$. As the number of undulator components n_u increases, the number of photons intuitively increases. Using the total power presented in equation 3.35, and introducing the fine structure constant $\alpha = e^2/(2\epsilon_0 ch)$, the number of photons produced per undulator component becomes

$$\frac{N_{\gamma u}}{n_u} = \frac{2\pi\alpha K_u^2}{3} \tag{3.48}$$

From this it can be seen that for the undulator regime, there is a squared dependence

for the number of photons generated on the undulator strength parameter K_u. As the $K_u < 1$ for an undulator, one can conclude that the emission of photons becomes very low as $K_u \to 0$. This is fitting with the expectations presented in Section 3.2 [35, 58].

3.3.2 Wigglers

With $\psi_0 > 1/\gamma$, an electron which traverses an wiggler setup is strongly modulated and emits a much broader spectrum which contains many harmonics up to a maximum cut-off energy.

In the treatment of the undulator, as the perpendicular deviation from the trajectory induced by the undulator was low, the variation in x motion and its effect on the z motion could be neglected. For $K_u > 1$, this can no longer be the case and equation 3.46 becomes

$$\dot{z} = \beta c \sqrt{1 - \frac{K_u^2}{\beta^2 \gamma^2} \sin^2(k_u z)} \tag{3.49}$$

This time the ratio between the time varying components of x and z can now be described.

$$\frac{\dot{x}}{\dot{z}} = -\frac{K_u \sin(k_u z)}{\beta\gamma \sqrt{1 - \frac{K_u^2}{\beta^2\gamma^2} \sin^2(k_u z)}} \tag{3.50}$$

For an ultra-relativistic electron $K_u \ll \gamma$, the denominator tends to 1 and hence a sinusoidal solution of the motion appears which peaks at K_u/γ. This results in a larder opening angle of $\psi_0 = K_u/\gamma$. In this regime, the resulting helical motion (demonstrated by equation 3.50) may contain harmonic modes. A simple treatment modifies equation 3.47 to become

$$\omega_w = m\omega = \frac{2m\gamma^{*2}}{1 + \gamma^{*2}\theta^2} \Omega_u \tag{3.51}$$

where m is the mode number and γ^* is the Lorentz factor modified to take into account the normalised drift velocity β^* i.e., $\gamma^* \approx \gamma/\sqrt{1 - K_u^2/2}$; however, for most ultra-relativistic cases, this can be approximated as $\gamma^* \approx \gamma$.

Clearly it is not possible for the modes to extend to infinity; thus, a critical cut-off frequency must exist. As the oscillations can be considered locally as a portion of the circle of radius ρ (as previously considered in Section 3.2), the electron can cover a distance $d_e = \rho/\gamma$ in a time interval $\Delta t = d_e/\beta c$. From geometric considerations, the radiation covers a distance $d_\gamma = 2\rho \sin(1/2\gamma)$ in the same time duration. The propagation time seen by a stationary observer becomes $t_\gamma = d_\gamma/c$. The burst duration τ received

becomes

$$\tau = t_e - t_\gamma \cong \frac{13\rho}{24\gamma^3 c} \tag{3.52}$$

Harmonics will thus be seen up to the value

$$\omega_c \approx 1/\tau \approx \gamma^3 \frac{c}{\rho} \tag{3.53}$$

With the sinusoidal variation in the trajectory of the particle, the radius of curvature varies with the position on the z axis as

$$\rho(z) = \rho_0 \frac{[1 + \psi^2 \cos^2(k_u x)]^{3/2}}{[\sin(k_u z)]} \tag{3.54}$$

Equation 3.53 is largest when $\rho = \rho_0$, this occurs when the electron is at it's peak position in x. At this point $\rho_0 = \gamma\lambda_u/2\pi K_u$; hence, the critical frequency is

$$\omega_c = \frac{3}{2} K_u \gamma^2 2\pi c/\lambda_u \tag{3.55}$$

It can be noted that for a wiggler system, the variation of ρ will result in a broad band of frequencies being observed up to the critical frequency. Using this critical frequency and recalling that the number of photons can be determined by $\dot{\mathrm{N}} = 2P(\omega)/E_\gamma$, the number of photons produced is given to be

$$\frac{N_{\gamma w}}{n_u} = \frac{5\sqrt{3}\pi\alpha K_u}{6} \tag{3.56}$$

From this it can be seen that for the wiggler regime, there is a linear dependence for the number of photons generated on the undulator strength parameter K_u. As the $K_u > 1$ for an wiggler, one can conclude that the emission of photons becomes higher $K_u \to \infty$. This will be accompanied by an increase in the angle of emission [35, 58].

3.4 Synchrotron Emission in the context of Lasers

In most conventional systems such as Linacs, the undulation of electrons are done by strong stationary magnets [21]. However, the large intensities currently available in the laser lab (see Chapter 4) means that an optical undulator provides a more compact and potentially effective means of generating high energy photons. Compton (or Thompson for non-quantum effects) scattering provides one of the key mechanisms by which lasers can begin to generate high energy photons.

3.4.1 Modified Equations (Classical)

To describe this interaction in the context of synchrotron radiation, a number of key elements require modification. The laser wavelength is λ_l and it's wavenumber $k_l = 2\pi/\lambda_l$. This means the frequency is $\omega_l = k_l c$ and energy $E_l = \hbar\omega_l$. The relativistic laser intensity parameter given in Chapter 2 equation 2.35 can be directly related to the undulator strength parameter K_u becomes

$$K_u = a_0 = 0.855\sqrt{I[10^{18}\mathrm{w/cm}^2]\lambda_L^2[\mu\mathrm{m}]} \tag{3.57}$$

For a counter-propagating geometry, as an ultra-relativistic electron advances through an intense laser field, it experiences both electric and magnetic fields resulting in an oscillation of Ω_u which is twice the laser light frequency. Given this, the frequency emission also becomes

$$\omega = \frac{2\pi c}{\lambda_l}\frac{4\gamma^2}{1 + a_0^2/2 + \gamma^2\theta^2} \tag{3.58}$$

The enhancement in the frequency is shows a factor 4 upshift rather than a factor 2, this can be thought of as the electrons response to both the elecctric an magnetic fields of the wave. The extra term in the denominator reflects ration of the laser intensity to the energy of the electron. In the case of Compton scattering this must be taken into account; however, if $\gamma \ll a_0$ then the interaction can be describes as Thomson scattering and this term can be neglected leaving the solution in it's much more familiar equation 3.47 form [35, 58].

3.4.2 Modified Equations (Quantum)

In quantum electrodynamics (QED) aims to marry the quantum framework with classical electodynamics [59]. So far, the discussion has viewed the laser field as a time varying electric field i.e., a classical treatment; however, it is well established that the laser may be viewed as a plethora of individual photons propagating along a common vector. In addition, electric fields around electrons given a quantum treatment can be considered as a small charge surrounded by a region of virtual photons. This quantisation of electric fields leads to some interesting consequences such as the possibility of generating an electron and positron from a vacuum by the photon-photon interactions or the introduction of the Schwinger limit of the field QED which indicates that given a strong enough field strength, a laser can produce electron-positron pairs from a vacuum ($E_L = 1.3 \times 10^{18}$ Vm^{-1}[59]). In addition, looking again at the a_0 parameter, one can now consider this as the average number of photons an electron will interact with within the laser field when $a_0 < 1$ [26].

In QED with the electron's field being quantised, when it propagates atultra- relativistic velocities, the quantised field becomes somewhat compressed in the propagation direction when observed in the labratory frame of reference and the relative number of photons at this front is increased. A laser pulse interacting with such a field has an enhanced probability of scattering with one of the virtual photons making the field up in what would be an exclusively quantum effect. A measure of the importance of quantum effects was eluded to in Chapter 9 and is known as χ or the quantum parameter.

$$\chi \approx 6.1 \times 10^{-6} \gamma a_0 \tag{3.59}$$

The introduction of QED effects has some interesting consequences for predicting the radiation is generated by using an intense laser as a wiggler. In Section 3.4, equation 3.58 is modified to become

$$\omega_B = \frac{4\gamma^2 \omega_L N_{ABS}}{1 + (\gamma\theta)^2 + \frac{a_0^2}{2} + 2\frac{N_{ABS}\chi}{a_0}} \tag{3.60}$$

Here ω_B is the boosted photon emitted by the undulator/wiggler (i.e. the laser). The two additional modifications seen in the denominator of Eq. 3.60 are $a_0^2/2$ which represents the depletion of the laser pulse as electrons propagate through it, and $2N_{ABS}\chi/a_0$ which introduces the χ parameter. The first correction becomes significant at $a_0 > 1$ i.e., the wiggler regime however, the second correction is very much a QED consideration and need only be considered at extreme intensities or ultra-high relativistic velocities [26].

3.4.3 Current Optical Undulator Results

Work in this field is already under way and various groups have demonstrated successfully the generation of high energy photons from optical interactions. Using a laser pulse to generate an electron beam through LWFA, a second off-axis laser pulse of $a_0 < 1$ was collided with the bunch. The resulting spectra was measured at 3×10^{18} photons s^{-1} mm^{-2} $mrad^{-2}$ per 0.1% BW [27]. Figure 3.5 shows that for the undulator regime, the pattern of the photons generated follows closely that of the electron spectra. This is typical of the linear nature of the interaction. With $\gamma_{max} = 160$ for the electrons and a laser intensity $a_0 \approx 0.25$, the peak energies of photons produced is shown to be 100 keV [27].

As the intensity becomes sufficient for exploration of the onset of the non-linear regime, the spectra produced become somewhat broader [44].

In figure 3.6, one can see the electron spectra are presented on the left and corresponding photon spectra on the right. Each horizontal trace shows a single laser shot. The

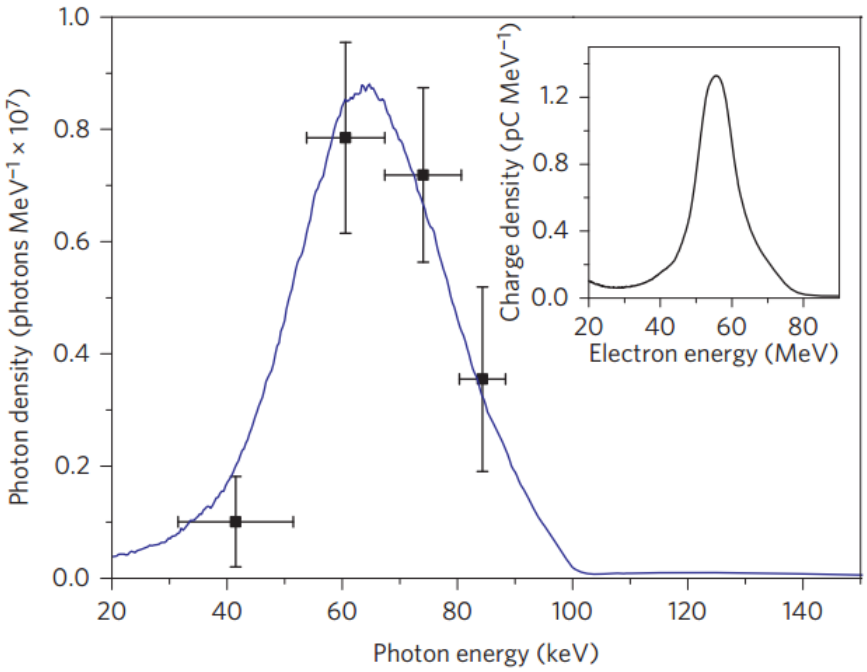

Fig. 3.5: X-ray spectral distribution (black squares) measured, for a single shot by Ross-filter pairs [27].

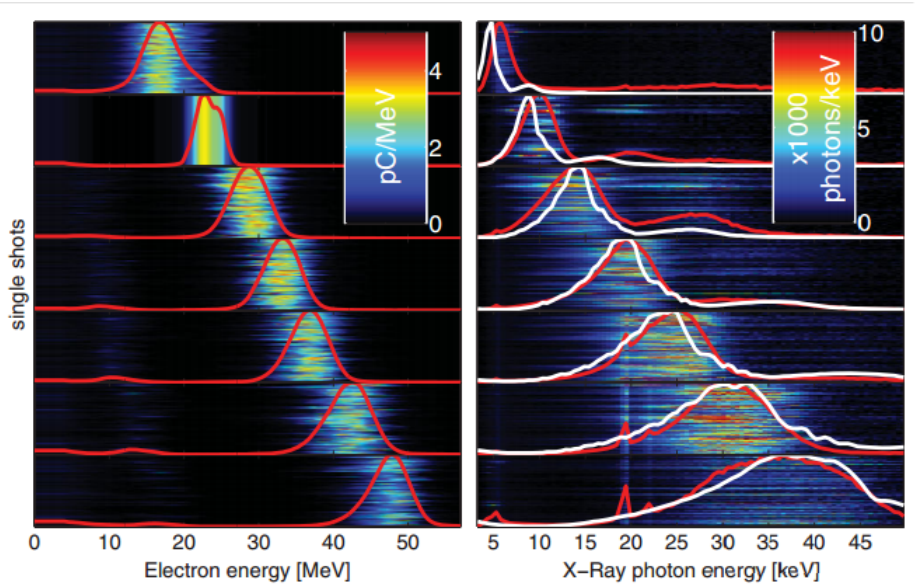

Fig. 3.6: The electron spectra are presented on the left and corresponding photon spectra on the right [44].

LWFA was tuned by use of a razor-blade in a variety of positions to increase the length of plasma the pulse propagated through while simultaneously exposing the laser to sharp density gradient. Run-averaged spectra are shown in red, white lines show the expected x-ray spectrum for each averaged electron spectrum. The simulation was performed with

simulation package SPECTRA 9.0, assuming an equivalent undulator model with a peak undulator parameter of $K_u = a_0 = 0.9$ [44]. One can see a strong correlation between the theory and results obtained.

The up-shift in laser photons via Thomson scattering is set to be a mechanism by which the Extreme Light Infrastructure (ELI) [60]. The ELI project aims to represent the pinnacle of laser science providing a peak power of 200 PW. Additionally, the ELI nuclear physics (ELINP) division in Romania aims exploit the properties of an all-optical Compton source to provide users with a stable source of tunable, high-energy photons with energies in the order of 0.219.5 MeV and spectral density of $(0.8-4)\times10^4$ ph $s^{-1}eV^{-1}$. This means that nuclear scientist can conduct experiments using a source with a peak brilliance $10^{20}10^{23}$ $s^{-1}mm^{-2}mrad^{-2}$ 0.1%BW [60, 61]. Already, users of the facility are planing to exploit this unique opportunity to conduct experiments in photofission [62] and particle core couplings in 'doubly magic' nuclei [63].

Part II

DIAGNOSTICS AND TECHNIQUES

4. LASERS

The early in 20^{th} century, represents one of the most exciting periods in modern physics. E. Rutherford's work on α particle scattering in 1911 lead to the understanding that an atom consisted of a highly charged nucleus which contained most of the mass of the atom, while electrons existed in a relatively low density cloud around this core [64]. Building upon this work, N. Bohr's work on the hydrogen atom in which he stated that within atoms, there existed a number of 'allowed' or quantized energy levels that orbiting electrons could occupy and that it is possible for electrons to make transitions between these allowed states provided that a quanta of energy is either absorbed or emitted by the atom [65]. In 1917, A. Einstein suggested that as photons were bosons, it would be possible to stimulate the emission of photons in the same state. A consequence of generating radiation in this way, was that the photons emitted would be identical in all relevant aspects to the incident radiation leading to the possibility of an amplified and coherent source of electrons [66]. It is this principle that forms the basis of the laser.

4.1 Emission of Radiation from Atoms

As the energy levels in an atom are quantized, an electron bound to an atom can only occupy those states which are permitted; however, it is possible for the electron to make transitions from one of these states to another provided the right energy is supplied.

If an atom has two states n_i and n_j with energies E_i and E_i respectively, then an electron in n_i could be supplied with energy $h\nu_{ij} = E_i - E_j$, where h is Plank's constant, in order to make the transition into state n_j. Figure 4.1 shows the possible mechanisms for absorption.

In figure 4.1 a), a particle such as an electron, with energy E interacts with the atom, losing $h\nu_{ij}$ in the process. The bound electron of the atom absorbs the energy and makes a transition to from E_i to E_j. Another absorption mechanism is shown in figure 4.1 b), where a photon of energy $h\nu_{ij}$ is incident on the atom. As the energy of the photon matches the energy required to make the transition, the atom absorbs the photon and the electron moves to the higher energy level. If the photon does not match the energy of the transition, the transition fails to occur (this does not hold for atoms with high photon numbers incident as in the multi-photon ionisation process see section 2.2). In figure 4.1

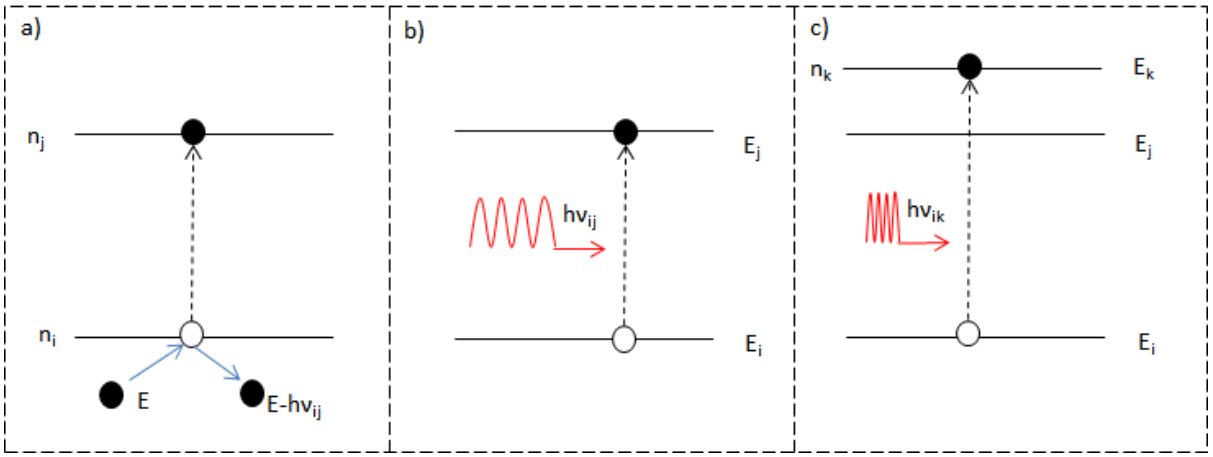

Fig. 4.1: The process of transitioning from lower to higher energy levels by (a) direct collisions or (b-c) photon absorption of allowed energies.

c), the possibility of making the transition between multiple states at once is shown. This may be useful in creating a population inversion. Real transitions of course, are not infinitely sharp as shown. There is a broadening in the range of the photon energies that can be absorbed. If the central frequency of photons absorbed is given by ν_0, frequencies close to this value (of frequency ν) may also be emitted. The rate of absorption is given by

$$\frac{dN_i}{dt} = -N_i B_{ij} \int_{-\infty}^{+\infty} g(\nu_0, \nu)\rho(\nu)d\nu \tag{4.1}$$

Where N_i is the population of electrons in state n_i, B_{ij} is the probability of making a transition from n_i to n_j, $g(\nu_0, \nu)$ is the lineshape function which describes the broadening of the photons emitted and $\rho(\nu)$ is the energy density of the stimulating field.

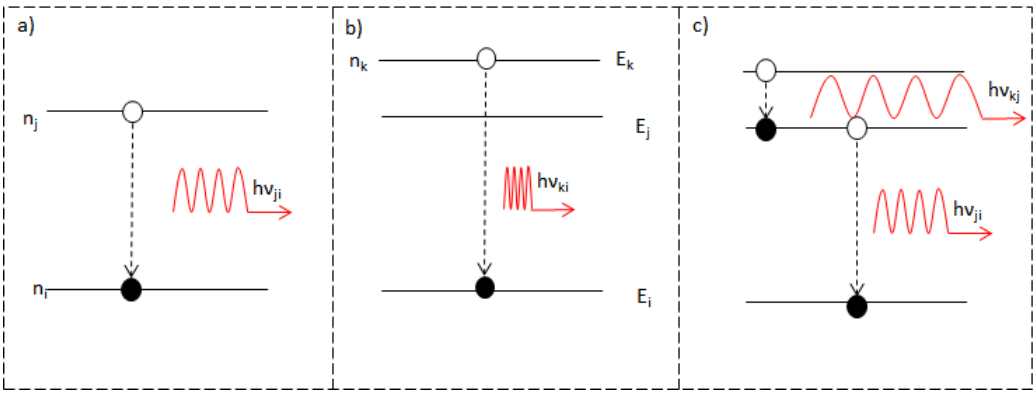

Fig. 4.2: Emission of photons as the electron transits to or towards the ground state.

As atoms with electrons in excited states are by definition unstable, an electron in an this state has a probability of making a spontaneous transition to a lower energy level. Figure 4.2 a) and b) show that the transition from one energy level to another can be

made in a single step. While figure 4.2 c) shows that multiple transitions can be made towards the n_i state. When a transition is made, the energy is manifest in the form of an emitted photon. The process is essentially the reverse of the absorption process.

Photons emitted are done so in a random direction with arbitrary polarization (unless the presence of strong electromagnetic fields needs to be taken into consideration). Likewise, there is an equation which governs the rate of spontaneous emission that may occur.

$$\frac{dN_j}{dt} = -N_j A_{ji} \int_{-\infty}^{+\infty} g(\nu_0, \nu) d\nu \tag{4.2}$$

This time N_j is the population of electrons in state n_j, A_{ji} is the probability of making a transition from n_j to n_i while all other terms have the same meaning. Relating the population of the states, one obtains

$$N_j = N_i e^{-h\nu_{ij}/k_B T} \tag{4.3}$$

As Einstein suggested, electrons can be stimulated into making these transitions by the action of electromagnetic radiation. An incoming photon of energy $h\nu_{ji}$ can cause the emission of a photon identical energy.

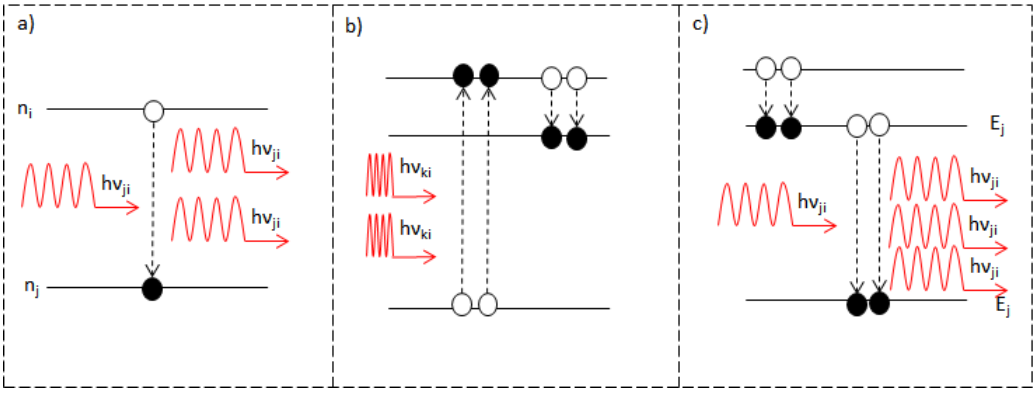

Fig. 4.3: The process of stimulated emission.

As shown in figure 4.3a, the photons generated upon stimulated emission have identical properties to the photons that created them. In figure 4.3b, the process widely used is to excite the atom to a higher energy level than that required. The electrons can then decay to the lower energy level which would be metastable i.e., the half-life of the electron in this state is much longer than other states. In figure 4.3c, a photon which is to be amplified is incident on the excited atom and stimulates the electrons to drop from this state and emit a photon that will be coherent with the original photon. Equation 4.4 describes the rate of emission due to stimulated emission.

$$\frac{dN_j}{dt} = -N_j B_{ji} \int_{-\infty}^{+\infty} g(\nu_0, \nu)\rho(\nu)d\nu \tag{4.4}$$

As expected, equations 4.4 and 4.1 have very similar forms. It is obvious that the radiation density term $\rho(\nu)$ is related to the intensity of the electromagnetic wave incident on the atom [67].

With both the absorption and stimulated emission rates related to the radiation density but moving in different directions, the ratio of population states is given by

$$\frac{N_j}{N_i} = \frac{B_{ij}\rho(\nu)}{A_{ji} + B_{ji}\rho(\nu)} = e^{-h\nu_{ij}/k_B T} \tag{4.5}$$

Equation 4.5 can be solved for the radiation density to give

$$\rho(\nu) = \frac{A_{ji}/B_{ji}}{(B_{ij}/B_{ji})e^{-h\nu_{ij}/k_B T} - 1} \tag{4.6}$$

Since $e^0 = 1$, this becomes maximum when the probability of stimulated emission equals that of the stimulated absorption. Putting this into more usable quantities, the radiation density is related to the intensity by $I_\nu = 4\rho(\nu)/c$ giving the equation

$$I_\nu = \frac{2\pi hc^2}{\lambda^5}\left[e^{-hc/\lambda k_B T} - 1\right]^{-1} \tag{4.7}$$

Because the population ratios presented here are for a system in thermal equilibrium, no lasing would occur. However, if the population was inverted so that $N_i < N_j$ then there would be a net bias towards stimulated emission. It is this that forms the principle of the laser. Equation 4.7 demonstrates the difficulty in that is experienced in generating lasing media for short wavelength lasers [67, 68].

4.2 Putting the Theory of Lasers Into Practice

Since it's realisation in the 1960's, the laser has become an indispensable tool in the study of physics. As the technology becomes increasingly sophisticated, so too do the nature of the discoveries made using it. Not long after its initial implementation, a period of rapid improvement in the technology was experienced as optical effects were discovered and subsequently exploited such as 'Q-switching' and 'mode-locking'. In these operating conditions, the laser pulse is amplified by containing the pulse in the laser cavity and allowing it to pass through a crystal many times. This effect was shown to be an effective way of achieving intensities greater than those obtained in continuous wave operation, but proved ultimately limited by the non-linear optical effects that would manifest as

the intensity grew. The impact a growing intensity has on an optical system can be understood by looking at the well established equation for refractive index

$$\eta = \eta_0 + \eta_2 I \tag{4.8}$$

The refractive index η of a material consists of a fixed term η_0 and a correction η_2 which is intensity dependent. Due to the spatial variation of the laser beam intensity, the wave front of the pulse becomes altered according to the 'B' integral which is given by:

$$B = \frac{2\pi}{\lambda} \int_0^L \eta_1 I dx \tag{4.9}$$

If λ is the wavelength of the pulse, then it is clear that the longer a pulse travels through an amplifying medium, the greater the change to it's wavefront. Higher intensities enhance this effect. The result can be the self focusing of a laser pulse where a single pulse may breakup into many filaments. This occurs above a critical parameter P_{cr}

$$P_{cr} = \frac{\lambda_0^2}{2\pi\eta_0\eta_1} \tag{4.10}$$

For this reason a laser system may be fitted with spatial filters in order to 'clean' the pulse and suppress this effect. To achieve a wave-front distortion of $\lambda/20$, B would need to be less than 0.3; thus, self-focusing remains a severe problem in any optical amplification system. As a result of this limitation, progress in laser technology remained slow until the advent of a new technique known as 'chirped pulse amplification' (CPA).

4.3 The Chirped Pulse Laser

First successfully demonstrated in 1985 by D. Strickland and G. A. Mourou [69], CPA represents the archetypal method of laser construction. The technique involves taking a short laser pulse and stretching it in time using a diffraction grating. This pulse is then amplified and then temporally compressed by a second diffraction grating.

Figure 4.4 shows the principle behind the implementation of CPA. CPA allows one to amplify the pulse safely without building up a sufficient intensity to causing problems such those described in the previous section before compressing it to achieve a higher intensity.

While broadening, amplifying and subsequently re-compressing a pulse will give a boost to the energy of the contained within it, delivering that energy in a short as time as possible is also necessary fo reaching high intensities. In order to achieve this, one must comment the importance of the spectral broadening. As time and frequency are Fourier

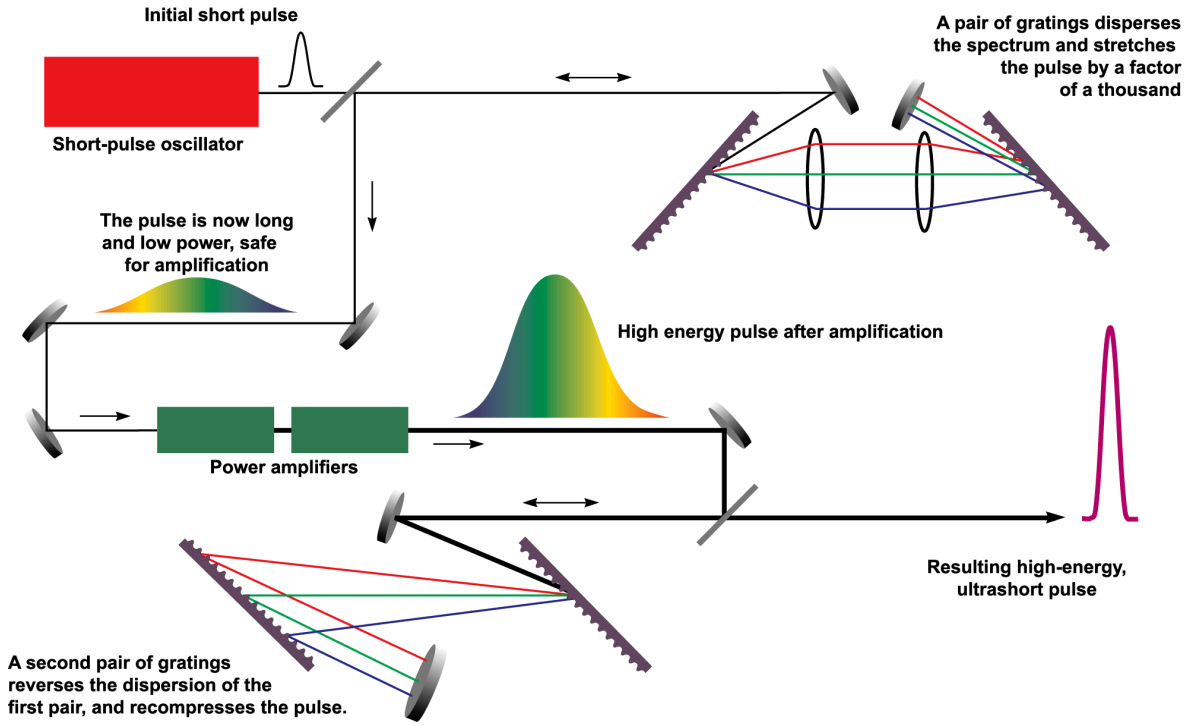

Fig. 4.4: The principles of CPA [70]).

conjugates, it follows that to create a short laser pulse, a large bandwidth is necessary.

Selecting the right lasing material becomes critical. A frequency doubled neodymium-doped yttrium orthovanadate (Nd:glass) mode locked laser provides a stable solution to produce a seed pulse which is of a broad spectrum. Using gratings to stretch the pulse, this seed propagates into a titanium doped sapphire crystal (Ti:sapphire) which amplifies across the entire spectrum in a manner which allows the amplified pulse to retain its relative intensity profile. A grating can then be selected which compresses pulses to 10's of fs.

CPA marks a new exciting period of growth in laser intensities which is demonstrated in figure 4.5 and by focusing laser energy onto a target with powers which exceed the entire output of the UK's national grid [71], it should come as no surprise that by using an intense laser, a sample of matter can be rapidly heated and ionised to form a plasma. The initial formation of the plasma is driven by electrons from the, or closest to the conduction bands of the atoms. The process can be viewed classically as a bulk effect of the electric field of the laser interacting and with the electrical potential of the atom, reducing it's magnitude subsequently, allowing the bound electron to escape [72]. Once this extremely rapid change is complete, the material can now have become a plasma. It was shown in Section 2.1 that the electron density is extremely important in determining the dynamics of the plasma that is formed and that strong electromagnetic fields have

unique . This is also true of how the energy is coupled into the plasma.

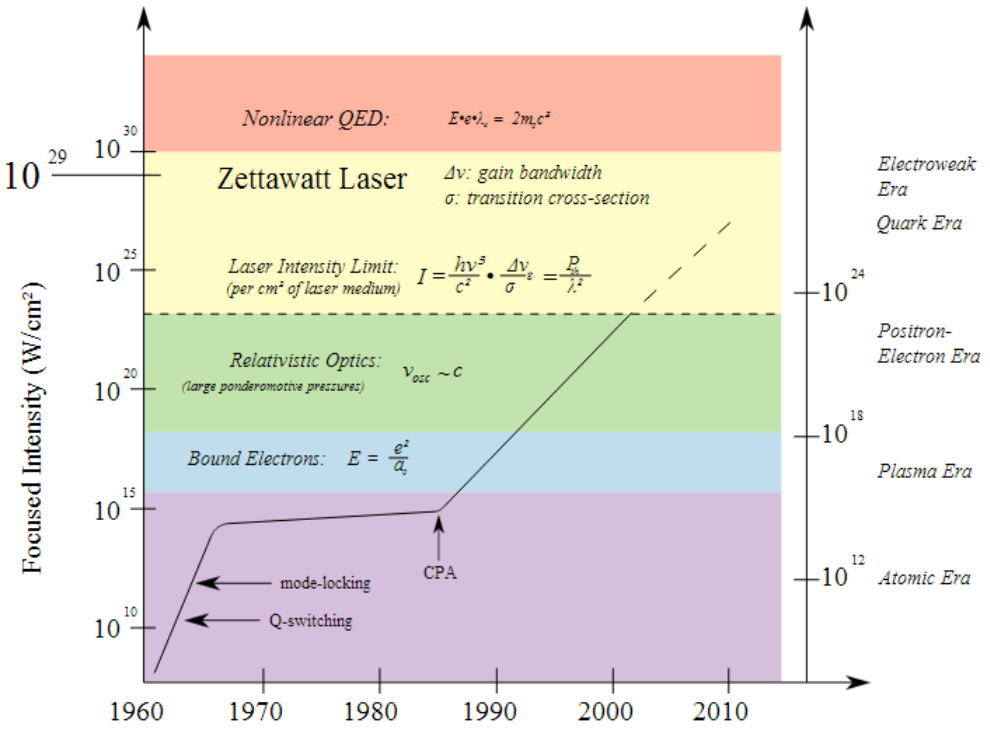

Fig. 4.5: The growth in intensity of laser pulses [70]).

After successful implementation of the CPA concept at millijoule and joule level, it became clear that the technique could be extended to much higher energies. This meant that with remarkably few alterations a TW pulses could now produce petawatt PW pulses [70]. With this, the possibility of investigating high intensity laser-plasma interactions became possible.

4.4 Astra-Gemini

One such laser that can achieve high-intensity ultra-short pulses is the Astra-Gemini laser in Rutherford Appleton Laboratories (RAL) [73, 74, 75, 76]. The Astra-Gemini laser system is a dual-beam petawatt class CPA Ti:sapphire laser system at the Central Laser Facility (CLF) in RAL. Each beam can deliver over 15 J in $<$ 50 femtoseconds in a spot with a diameter in the order of a few μm.

The system is based on two multi-pass Ti:Sapphire amplifiers pumped by 4 beams at the second harmonic of a Nd:glass laser with an energy 25 J in each beam. The input for the amplifiers is the 1.5 J. A train of pulses at 10 Hz is selected from the kHz train using a fast Pockels cell and stretched twice in the existing stretcher to give a 1 ns pulse length in a process similar to that used in a regenerative amplifier. The long pulse duration

aids in the suppression of the non-linear phase integral. The pulse train is incident on 2 large aperture amplifiers which can be fired once every 20 seconds. The 25 J amplified output is compressed in vacuum grating compressors to give 0.5 PW power in each beam [76]. The Astra-Gemini system is able to carry out contrast measurements by using the

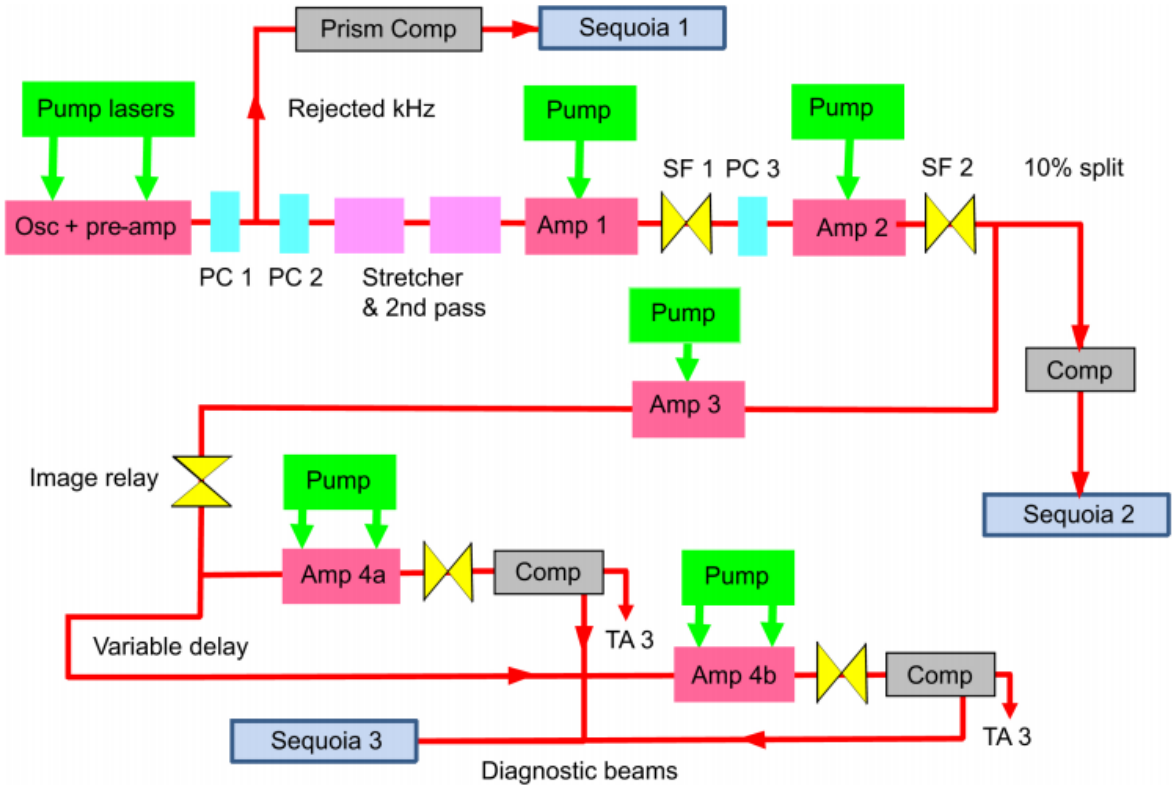

Fig. 4.6: The schematic block diagram of the Astra-Gemini laser system [76].

'Sequoia's' [77] to allow the operators to reduce the effects of the coherent pedestal by grating adjustments. Which are important for mechanisms such as shock injection in LWFA.

The Astra-Gemini laser allows the beams to be introduced to the chamber in two separate positions hence, providing a unique opportunity for experimenters to design and implement experimental geometries that would otherwise impossible.

5. IMPLEMENTATION OF LASER-WAKEFIELD ACCELERATION

5.1 Gas Density

The LWFA technique has been developed over the last few decades and is now regularly employed for the generation of multi MeV electron beams. To create a stable cavity for the acceleration of electrons the gas helium is used. However, with $Z = 2$ helium is not able to produce electron beams with significant charge. A higher Z gas such as nitrogen can be mixed in small quantities ($\sim 3\%$) to the helium to allow a larger number of electrons to be injected into the bubble and enhance the numbers of electrons generated. For petawatt class of lasers firing onto such gas targets, the spectral shape of the electron bunches normally consists of a high energy bunch of electrons with a typically Gaussian spread followed by a lower flat or decaying tail of electrons as the energy decreases. Looking at figure 2.2 one can imagine an optimal point of injection in the centre of the bunch. Electrons here will experience the longest time in the accelerating gradient; however, for a large cavity, there are many non-ideal points of injection in which the electrons will see a shorter gradient and not be accelerated to the highest energies achieved by those ideally injected. Figure 5.1 demonstrates the some of the ongoing work into LWFA and it's dependence on gas densities used employed [78].

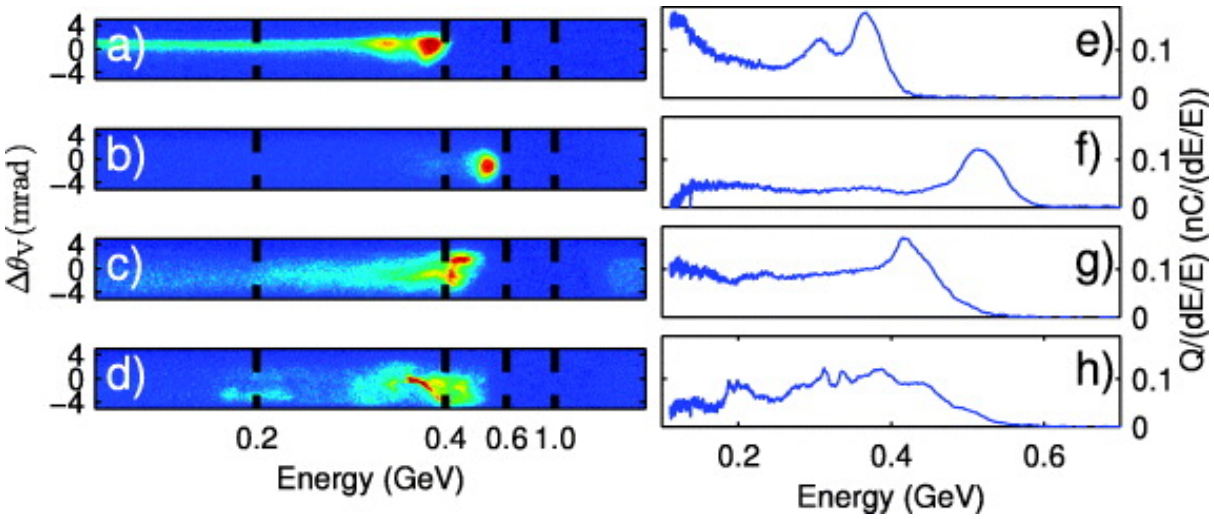

Fig. 5.1: Examples of raw electron energy spectra $(a - d)$ and spectra in units of charge per relative energy spread $(e - h)$ [78].

Figure 5.1 shows examples of raw electron energy spectra $(a-d)$ showing the fluorescence observed on a Lanex screen [79], and spectra in units of charge per relative energy spread $(e-h)$. These were observed ad a range of pressures from 50, 80, 100 and 200 mbar of gases [78].

It can be seen that there is an optimum pressure that exists for each setup that can generate a high-energy, high-quality i.e., beams with large numbers in the forward peak energy and a highly suppressed low energy tail. From figure 5.1, it can be seen that the gas must be dense enough as to have sufficient ion species with which to generate the large accelerating gradient, while not being so dense that the laser group velocity is reduced sufficiently so as to allow de-phasing to occur and destroy the wakefield. In the case above, the optimal was found to be 80 mbar however, it must be noted that as the Ponderomotive force is dependent on a_0, each system will have an optimal pressure that must be found.

5.2 The Effects of Laser Intensity

As the ponderomtive force scales with ∇a_0^2, it follows that using a more intense laser pulse should result in electron beam with higher energies. A prediction of the spectra is presented in figure 5.2. At higher laser intensities from $a_0 = 10$ (black), to $a\_0 = 20$ (blue) and finally $a_0 = 40$ (red), one can see that the spectral shape remains consistent but the peak energies increase significantly with a_0. However, improvements in laser technology are inevitably slower than advancements in computational physics and a increase in intensity will come with a reduction in the focal spot size and thus a smaller Rayleigh range of the laser which is not conducive for the production of stable accelerating cavities. As the approach of increasing the intensity to gain higher energies is currently not technologically feasible, other perhaps more subtle approaches are useful. This is a highly active area of research exploring many avenues such as two stage acceleration, where the injection happens in the first stage and acceleration in the second, and duel pulse where one pulse sets up the cavity and the second injects the electrons into it [22].

5.3 Gas Delivery

In addition to how dense the gas is, how the gas is actually delivered to the laser target area is a crucial parameter. Initially the gas was delivered to the chamber by means of a jet which puffs the gas at supersonic speed into the path of the laser; however, attention has turned towards the use of gas-cells. Gas-cells are used to contain the gas once it is puffed into the chamber in a small cell which has two small holes at either end to allow

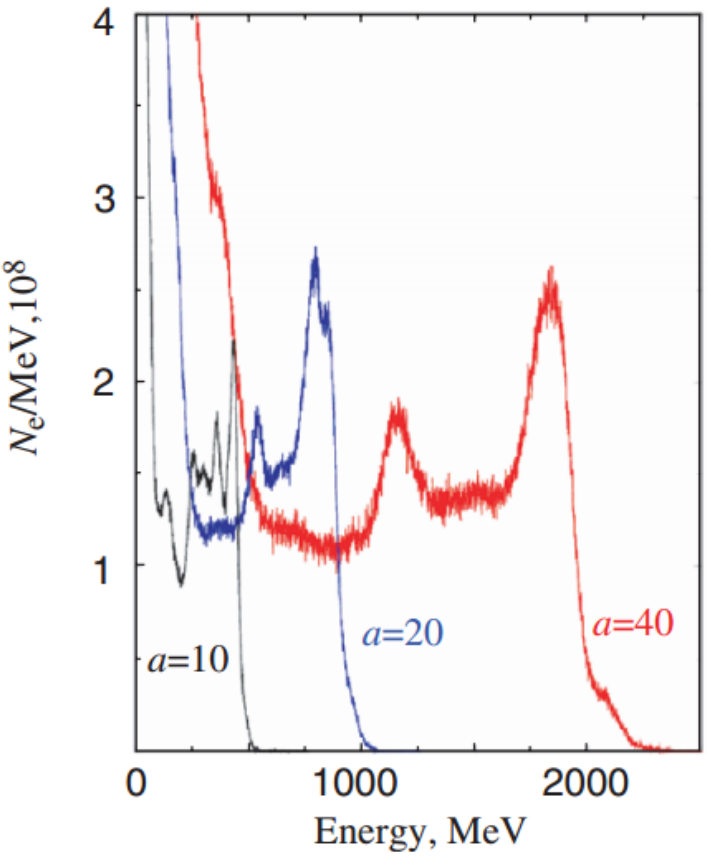

Fig. 5.2: Spectra predicted at higher laser intensities from a_0 = 10 (black), to a_0 = 20 (blue) and finally a_0 = 40 (red) [80].

the laser to propagate through the gas. This means that the variation in gas density and turbulence experienced by the laser shot to shot is greatly reduced.

However, as there are two competing processes in the single pulse LWFA i.e., the shock injection which favours a high density and acceleration, which favours a lower density lest the wake outrun the laser and cause de-phasing, the use of two-stage gas cells has been suggested. A comparison between gas-jets and single and two stage gas cells is given in figure 5.3. As can be seen in figure 5.3, the gas-cells tend to out perform the gas jet in each parameter. The single stage gas cell produces bunches with higher charge (a) and can attain the highest peak energies (b), while the two stage cell seems to perform best in producing bunches with lower pointing variations (c), and beam divergence (d) and energy spread (e). In each instance the gas-cell is demonstrated to be superior to the gas jet in all pertinent factors [81]. However, what is also demonstrated is that an experimenter interested in the application of LWFA, must choose which setup to employ dependant on their needs.

The current record for the highest energy of laser-driven electron beams is held by the BELLA laser [82]. Using another method of gas delivery. Implementation of a 10 cm

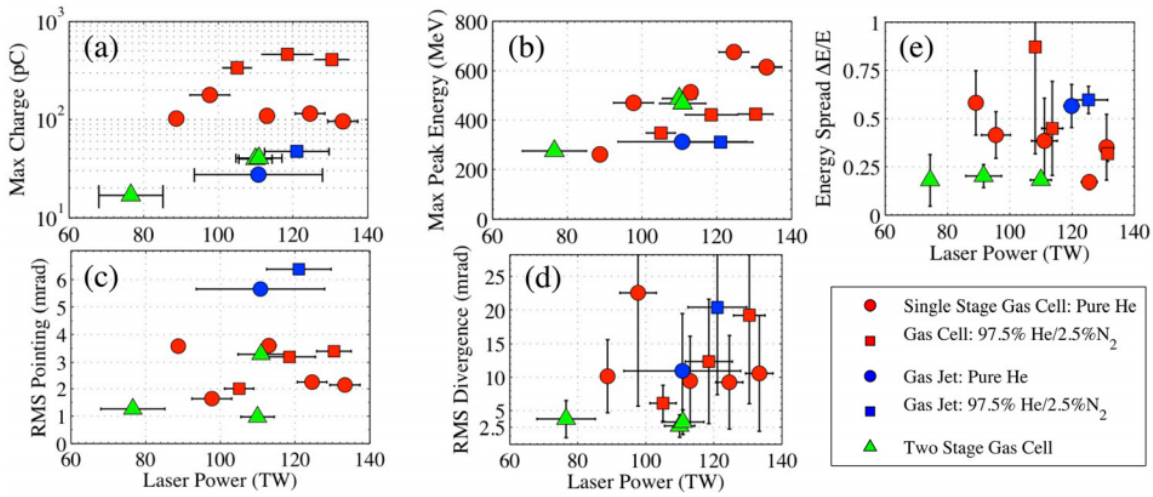

Fig. 5.3: The performance of gas-jets, single stage and two stage gas-cells is compared for a variety of parameters. [81].

capillary, the laser is efficiently guided allowing the electrons to experience a long channel to accelerate in. The results are shown in figure5.4 [82, 83]. While the results presented in

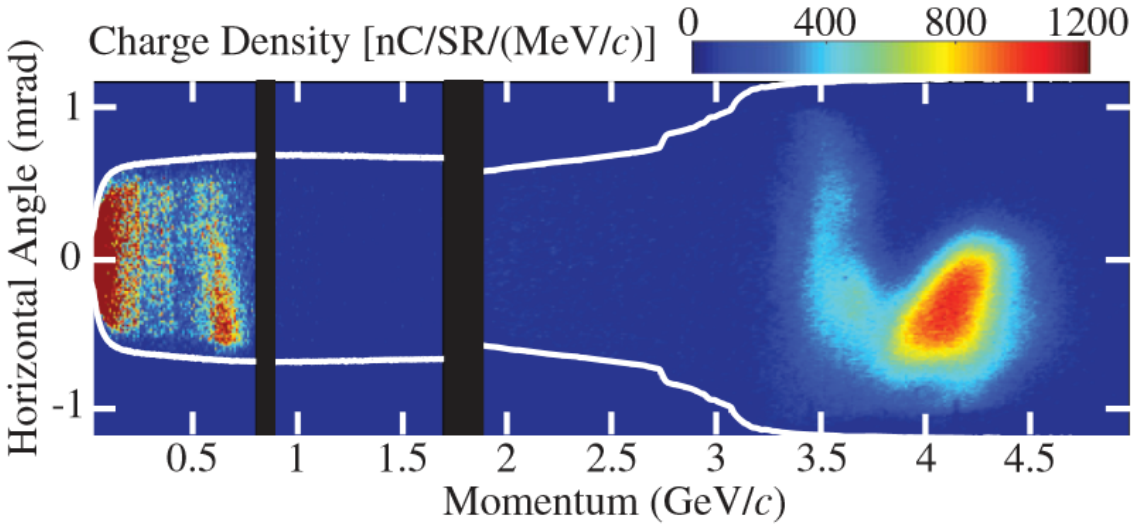

Fig. 5.4: The state of the art LWFA can produce 6 pC beams with an energy spectrum which reaches a 4.2 GeV by employing the use of capillary tubes as waveguides [82, 83].

figure 5.4 are incredibly impressive and mean that BELLA holds the record for electron energy produce via LWFA, the long focal length of the laser required to achieve such stable acceleration may make its implantation unfeasible in some laboratories.

6. DETECTION AND SPECTRAL RESOLUTION RELATIVISTIC ELECTRONS

The detection of relativistic electrons is of clear importance for the study of LWFA and will be shown in Chapter 7 to be required to determine the gamma-ray spectrum produced by non-linear Thomson scattering. In recent years, the use of magnetic spectrometers which employ use of imaging plates [84, 85, 86, 87, 88, 89] or lanex screens [79] as a detection mechanism, has become a staple of the laser-plasma laboratory. Here the basic concept for spectrally resolving electrons is presented before looking at the detection of relativistic electrons.

6.1 Magnetic Spectrometers

If one considers an electron moving through a region of space with $\mathbf{E} = 0$ but $\mathbf{B}_y \neq 0$, it's equation of motion can be given by

$$m_e \dot{\mathbf{u}}_\mathbf{e} = e[\mathbf{u}_\mathbf{e} \times \mathbf{B}] \tag{6.1}$$

For an electron whose velocity is perpendicular to the magnetic field, differentiation of the those components yields the results: $\ddot{u}_{ez} = -(eB/m_e)^2 \dot{u}_{ex}$ and $\ddot{u}_{ex} = -(eB/m_e)^2 \dot{u}_{ez}$ i.e., the electron is in simple harmonic motion with a cyclotron frequency of $\omega_\rho = eB/m_e$. Hence, the solution must be $u_{ez} = u_e e^{i\omega t}$ [49], the differential of which gives the radius of this motion to be

$$\rho_{\text{class}} = \frac{u_e}{\omega_\rho} = \frac{m_e u_e}{eB} \tag{6.2}$$

As we move into the relativistic case, the electrons observed increase in mass effects the cyclotron frequency so $\omega_\rho = eB/\gamma m_e$. The introduction of γ adds a level of complexity to the equation and in order to relate momentum p to the kinetic energy ε, one considers the relationship $p = \sqrt{\varepsilon^2 - m_e^2 c^4}/c$; which allows equation 6.2 to be written

$$\rho = \frac{\sqrt{\varepsilon^2 - m_e^2 c^4}}{ceB} \tag{6.3}$$

Hence, in the ultra-relativistic form ρ becomes

$$\rho_{\text{ult}} = \frac{\varepsilon(\text{eV})}{cB} \tag{6.4}$$

It can be noted at this point that at an energy of 1.2 MeV, the difference in equations 6.3 and 6.4 falls below 10%, with a fall to 1% beyond 3.6 MeV meaning that for most purposes in this body of work, equation 6.4 will be sufficient and help to reduce complexity.

6.1.1 Spectrometer Geometry

With a clear dependence on the energy and magnetic field strength, selecting a suitable length of magnetic field so that $L_m < \rho$ one can disperse a bunch of electrons in terms of their energies. Upon transiting the magnetic field, the electrons will leave with a variety trajectories. Using simple geometric considerations, one can map the location at detector to the energy of electron that transited the magnet. Figure 6.1 shows the concept of a

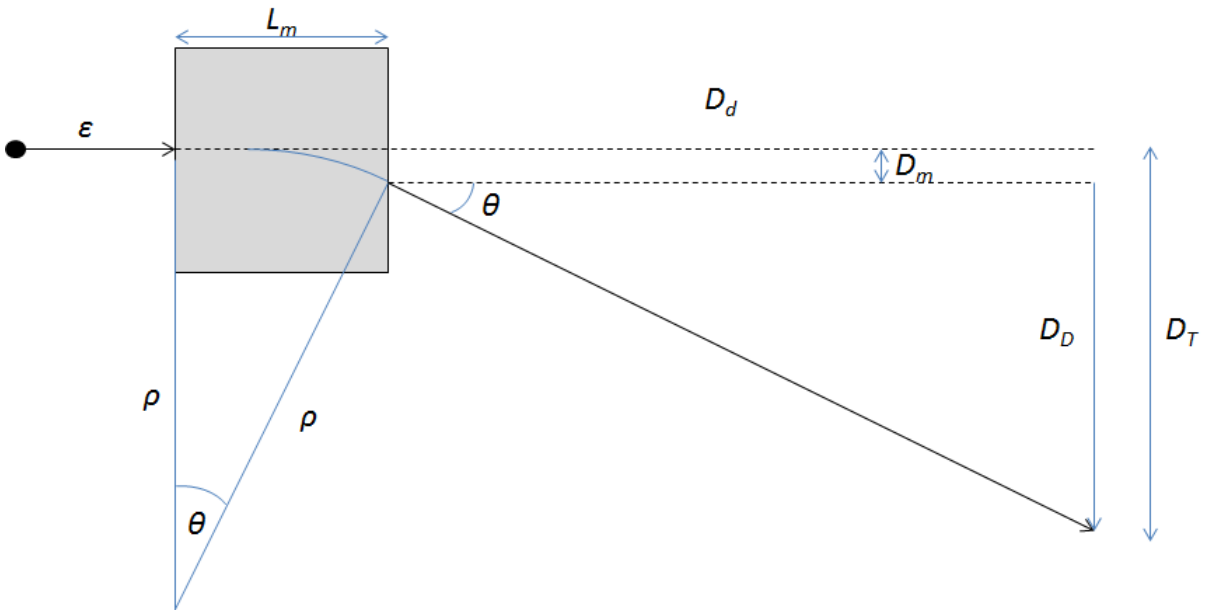

Fig. 6.1: The concept of a magnetic spectrometer.

magnetic spectrometer. The electron enters perpendicular to the magnet field of length L_m and is deflected around the circle of diameter ρ. The electron deflects by D_m within the magnet and exists with angle θ. As it propagates along this new trajectory, it is deflected by D_D from the original trajectory along D_d meaning a total deflection of $D_T = D_d + D_m$.

From geometric considerations; $\theta = \sin^{-1} L_m/\rho$ meaning that $D_D = (D_d - L_m)\tan\theta$. With $D_m = \rho - \sqrt{\rho^2 - L_m^2}$ i.e., the sagitta of the arc drawn out by the electron in the

magnetic field, the total deflection becomes

$$D_T = \left[(D_d - L_m)\tan\theta\right] + \left[\rho - \sqrt{\rho^2 - L_m^2}\right] \tag{6.5}$$

By considering then the well known relationship $\tan\theta = \sin\theta/\cos\theta$ with $\cos\theta = \rho/(\rho - D_m)$, one can rewrite this as

$$D_T = \frac{1}{\rho}\left[\frac{(D_d - L_m)L_m}{\sqrt{1 - L_m^2/\rho^2}}\right] + \left[\rho - \sqrt{\rho^2 - L_m^2}\right] \tag{6.6}$$

Equation 6.6 allows one to reference the points electrons arrive at a deviated from their original path to their energy. Looking at the first term of equation 6.6 and at equations 6.2-6.4, one can see that there is an inverse dependency on the energy of the particle and as expected, if $L_m \leq \rho$, the equation becomes meaningless. At this point, electrons are ejected from the magnetic field. This indicates that detectors of this type will inevitability have a cut-off energy below which it cannot work. In addition, the first term shows a strong dependence on D_d demonstrating the need for sufficient space in the use of these types of detectors if high energy particle are to be detected. The second term demonstrates that for $\rho \gg L_m$ i.e., at larger energies, this corrective term tends to 0. While this term is dependent on the geometry and energy for most MeV detection it can be neglected.

6.1.2 The Effect of Beam Divergence on Resolution

Above, the geometry is considered for a single electron; however, one must consider the natural divergence that will be intrinsic to an electron bunch as this will be the limiting factor to the resolution. For a purely monoenergetic electron beam, the divergence angle would give an elliptic shape on the detector around the mean deviation angle. The spectral resolution of this magnetic spectrometer has been shown to depend upon not only the angular divergence θ_s and distance from the source to the magnet D_s but on ρ. The relative energy resolution $\delta E/E$ of a magnetic spectrometer in the ultra-relativistic case is given by [90, 91]:

$$\frac{\delta E}{E} \approx \frac{\varepsilon(\mathrm{eV})}{cB}\frac{(D_s + D_d)\theta_s}{(D_d - L_m/2)L_m} \tag{6.7}$$

Equation 6.7 shows that the spectral resolution of a magnetic spectrometer improves as B and L_m increase. However, the resolution degrades if the magnet is placed far from the source of electrons or if the distance to the detector becomes large. This is due to the divergence of the source causing the electrons to spread over a range of energies. This spreading is much more detrimental to the resolution at higher energies as the high

energy electrons become less deflected. Hence, careful consideration must be given when designing a spectrometer to these factors. Figure 6.2 shows the variety of factors that

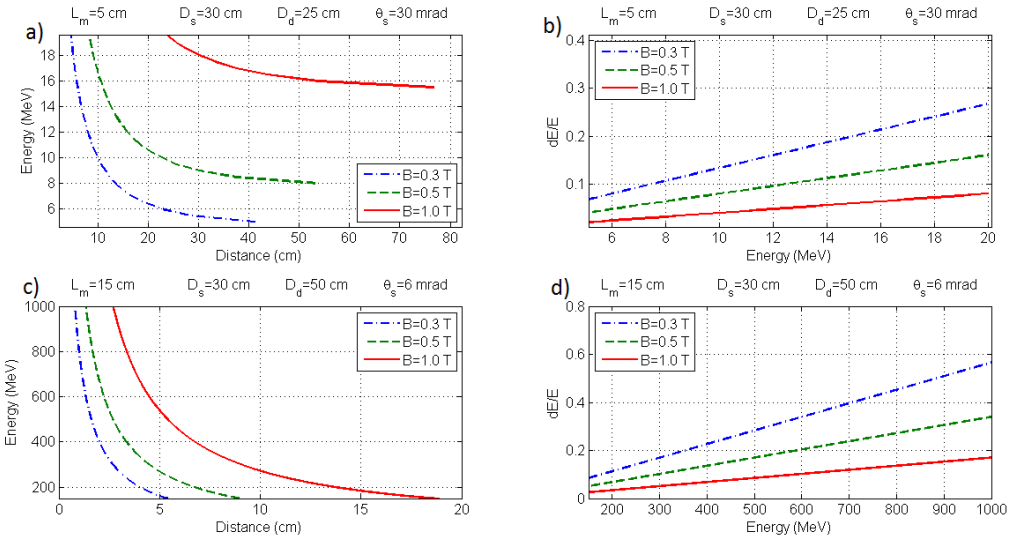

Fig. 6.2: A demonstration of the variety of factors that are considered when designing a magnetic spectrometer.

are considered when designing a magnetic spectrometer. The top figures $(a-b)$ show the arrangement for a 5 cm magnet, 25 cm from a detector with a source 30 cm away with a divergence of 30 mrad. Various magnetic field strengths are applied; 0.3 T (dot-dash blue), 0.5 T (dash green) and 1.0 T (solid red). a shows the distance the electrons are deflected by at the detector for their energy. It can be seen that in order to resolve lower energies, B must decrease in strength; however, b shows the resolution of the detector at each energy which degrades at higher energies.

The bottom figures $(c-d)$ show the arrangement for a 15 cm magnet, 75 cm from a detector with a source 30 cm away with a divergence of 6 mrad. Magnetic field strengths applied as above. c also shows the distance the electrons are deflected by at the detector for their energy. It can be seen that for high energies, B must have sufficient strength to spread the electrons sufficiently for a detector to resolve.

6.1.3 A Note on Practical Implementation

Clearly, one has a variety of parameters that must be carefully selected to complete the task of gaining spectral resolution from this technique; however, what has been presented here is an analytical approach to a practical piece of apparatus which has assumed that the magnetic field is confined to, and uniform within the desired region. This is of course not physical and while one designs a spectrometer using the considerations given above,

the reality is that the most effective method of determining the performance is to map out the magnetic field with a gaussmeter and solve the equations of motion for the electron trajectory for each point through the magnet. This approach ensures that obtaining an accurate description of the electron energy at each point on the detector is achieved.

6.2 Relativistic Electron Detection

Once the electrons are resolved in terms of energy by the magnetic field, the task of detection of these relativistic particles can be achieved in a variety of manners. There are two common approaches whose selection and will depend on the specific requirement of the spectrometer.

6.2.1 Imaging Plates

Developed by 'Fujifilm' for medical imaging [92], X-ray imaging by using storage phosphors has been an established method of taking data on synchrotron x-ray stations [**?**] and are now a staple of many plasma physics laboratories. Image plates (IPs) consist of an x-ray sensitive material made from BaF(Br,I):Eu^{2+} phosphor crystals suspended in a plastic binder. Incident energy cause the ionisation of the Eu^{2+} ions, generating photoelectrons that become trapped in lattice defects created by the absence of halogen ions in the BaF crystals. Upon irradiating the IP with a red laser beam, the electrons recombine, reducing the Eu^{3+} back to Eu^{2+}releasing a blue photon in the process. This photostimulated luminescence (PSL) can then be collected by a photomultiplier, creating a digital image [84].

$$\mathrm{PSL} = \left(\frac{R}{100}\right)^2 \left(\frac{4000}{S}\right) 10^{L[G/(2^B-1)-1/2]} \tag{6.8}$$

Where R is the resolution in μm, S is the sensitivity (given by the scanning device as 1000, 4000 or $10,000$), L is the latitude (given by the scanning device as 4 or 5), B is the dynamic range (8 or 16 bits) and G is the grayscale [84, 89] which can be read out by program such as 'ImageJ' [93]. It can be noted at this point that various scanners will return unique settings and that this has been studied comprehensively and calibration procedures should be applied to an image plate scanner of any make or model before any investigation is carried out [87]. The above settings are for the Fuji model 'FLA-7000' which is used in the CLF at RAL [89].

Once the PSL value is established, the value must be corrected for the fading that occurs due to thermal emission. Figure 6.3 *a*) shows the fading relative PSL value for an image plate over a time period of 120 mins. The decay is rapid at first before it begins to taper off after around 60 mins [85]. Recalling equation 4.3 (which one can assume will

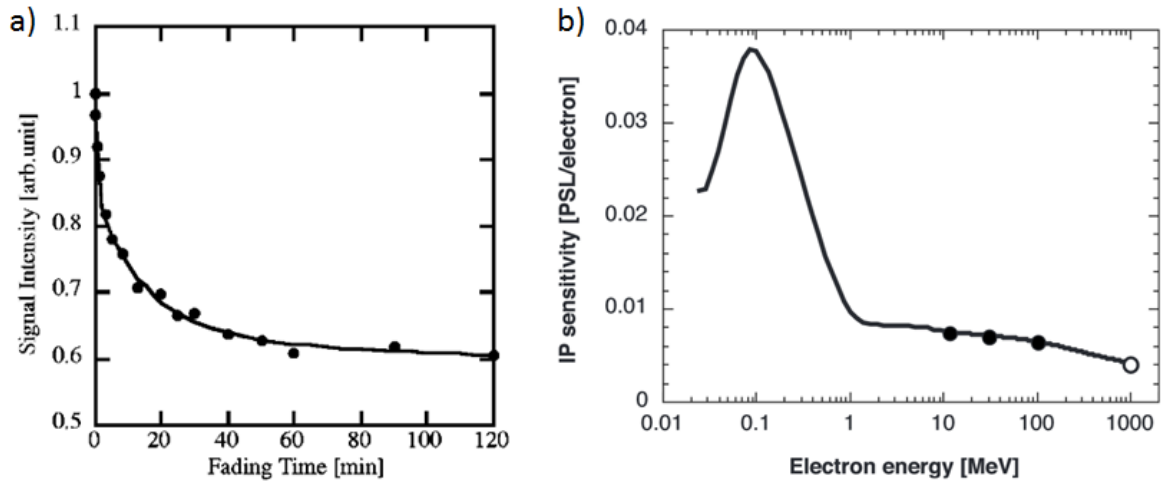

Fig. 6.3: The factors effecting the PSL value of an image plate. (a) the fading relative PSL (b) as well as the PSL over a range of energies [85, 88].

be of a similar form for atomic recombination), one can begin to see that in this excited state, there is a chance of spontaneous decay back to the ground state. The population of Eu^{3+} ions is of course, at a maximum after the sample is irradiated and as the rate of decay is directly proportional to this population, the profile follows an exponential decay curve. It is hence, important for experimenters to keep a detailed record of shot and scan times over the course of a campaign.

Once this data has been established, the PSL value can then be related back to the energy of the electrons that deposited that energy. This was done for electron energies initially up to 100 MeV [85] before being extended up to 1 GeV [88]. Figure 6.3 b) shows the PSL deposited per electron. Electrons with energies in the keV range deposit much more than those with MeV energy. Beyond 1 MeV, the energy deposited remains constant over a large range of energies up to 1 GeV, which is typical of relativistic electron-atom cross-sections [94].

6.2.2 LANEX screens

While IP's provide a solid detector for relativistic electron bunches, the high rate of repetition in many laser facilities mean that time can be more effectively spent if diagnostics are online and in-situ. Provided that the numbers of electrons present are sufficient i.e., enough to cause signal to be more that the background, a scintillator screen can be deployed in place of an IP. This technique has been commonplace for over 30 years [95].

In Section **??**, the population of electrons in excited states was discussed. Using this rationale and again recalling equations 4.3 and 4.2, one can see that if relativistic electrons deposit energy in a material, the excitation of local electrons to higher energy

levels may lead to the fluorescence of that material. LANEX screens are phosphors such as Gd_2O_2S:Tb and work in this manner [96].

For multi MeV bunches such as those generated in LWFA, the LANEX provides an excellent alternative to the IP and extensive work has been carried out to calibrate the fluorescence of the phosphor to the number of electrons interacting with the screen [79]. While there is a largely linear response between the number of electrons and the signal level [97], because the viewing of the screen is carried out by imaging the screen onto a CCD, each setup will exhibit a unique set of properties which the experimenter must consider (such as lens collection efficiency, the quantum efficiency of the CCD chip, gain applied etc.). In many cases it is possible to cross calibrate the image seen on the CCD with that observed by the IP this will be elaborated upon in Chapter 9.

6.2.3 Specific Detector Choice

In considering which detector to choose, one must consider the advantages and practical limitations of each. Imaging plates are very sensitive over a wide range of values however, the fact that they cannot be scanned in-situ means that an experimenter using a high-rep laser should be cautious about their use. And as the LANEX screen is able to give instant feedback to experimenters through the use of on-line CCD's, they seem to be the obvious choice; however, as the collection of very low signal levels can be hampered by the collection angle imposed on the system by the lenses employed, the use of LANEX is limited to situations in which one is able to guarantee high levels of signal on a shot to shot basis.

7. THE LITHIUM DETECTOR

A novel approach to the detection of gamma rays has been developed with the main properties of this detector being confirmed by proof of principle experiments [98] and Monte Carlo simulations performed using the code FLUKA [99, 100].

The detector exploits Compton scattering of the gamma-ray photons in a low-Z solid (lithium in this case). It is shown that, for a suitable lithium thickness, the scattered electron population retains a similar spectral shape as the initial gamma-ray beam, as long as the latter has an energy not exceeding 20 MeV. By measuring flux and spectrum of this electron population by means of a magnetic spectrometer, it is thus possible to deconvolve the signal and retrieve the spectrum of the gamma-ray beam which produced it.

7.1 MeV Gamma-Ray Interaction with Lithium

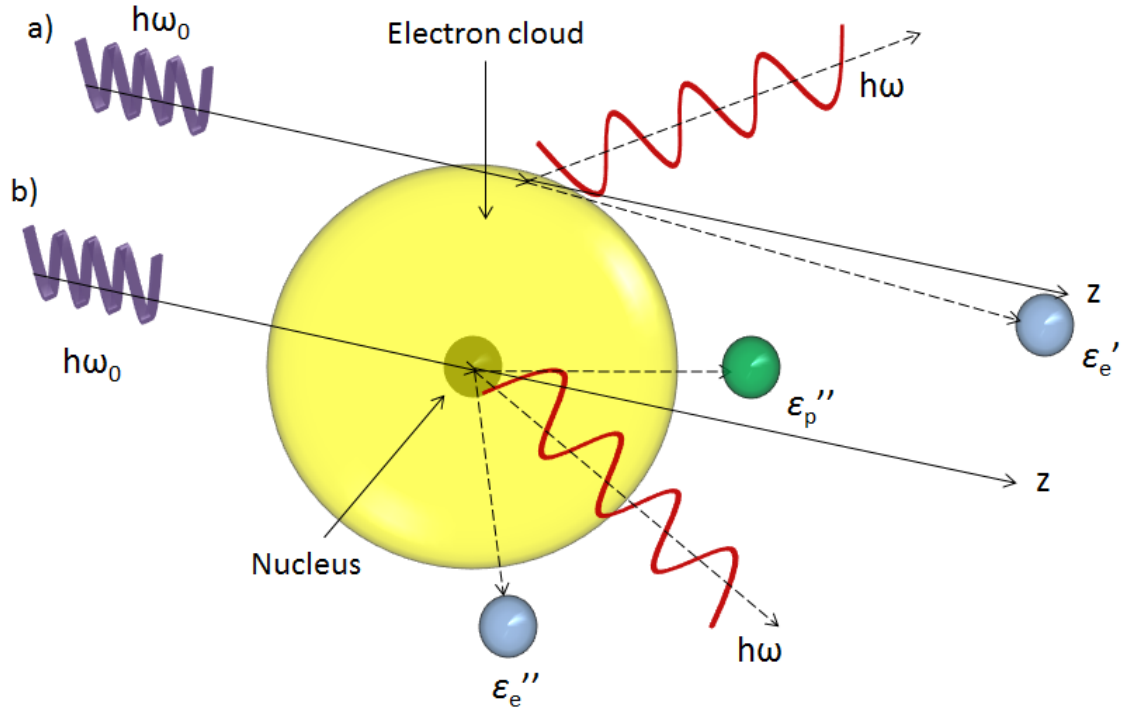

Fig. 7.1: Photon collisions with (a) an electron (b) or the nucleus of an atom.

Figure 7.1 shows some of the various was in which photons interact with atoms. The main interaction mechanisms are photo-ionisation, Compton scattering, and electron-positron pair production. In the multi-MeV regime, one can neglect the effect of photon-ionization since the energy loss associated with this mechanism is in the eV range.

As seen in figure 7.1(a), Compton scattering between an MeV photon and an electron at rest can essentially be considered as an elastic process. A photon collides with energy $h\omega_0$ is incident on the electron of an atom. Upon collision, the electron, absorbs the majority of the energy carrying it off in the form of kinetic energy ε_e'. A secondary photon of energy $h\omega$ may be present however, this is an elastic collision and ε_e' can be easily related to the incident photon. The forward scattered electron is expected to have an energy comparable to that of the incident photon.

In figure 7.1(b), a second photon also of energy $h\omega_0$ is incident on the nucleus of the atom. This time the >MeV photon, energy produces an electron-positron pair and a secondary photon of energy $h\omega$. As a 3 body collision, the electron energy ε_e'' and positron energy ε_p'' would not be trivia to calculate. As the energy given to the electrons in elastic collisions is much easier to relate back to the initial photon energy, it follows that in order to generate an electron population with a spectrum similar to the incident gamma-ray beam, the probability of Compton scattering needs to be much greater than that of pair production.

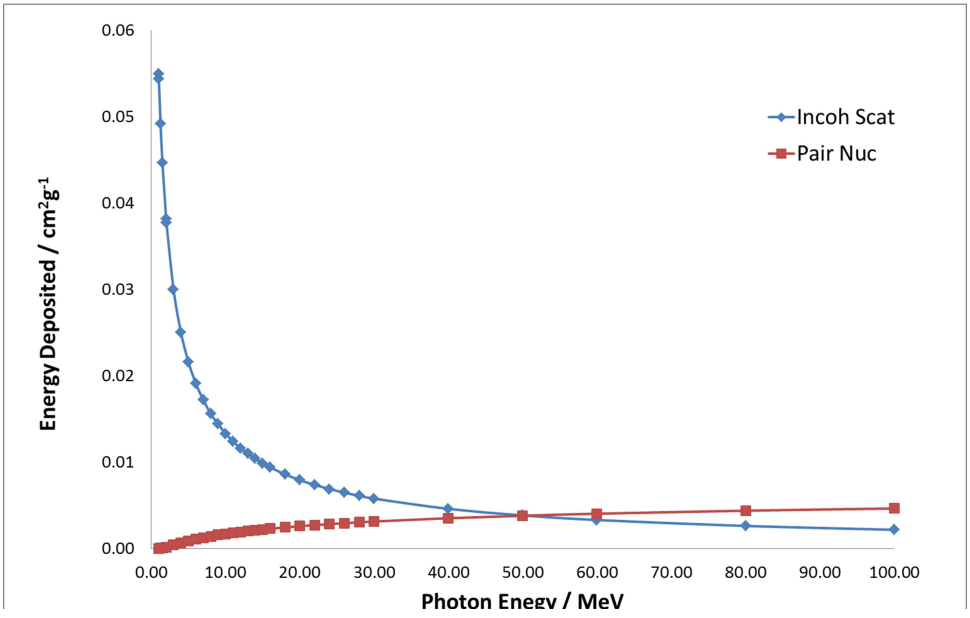

Fig. 7.2: Energy loss for a multi-MeV gamma ray beam as it interacts with lithium from the NIST database[94].

Since pair-production scales with the square of the atomic number Z [59, 101], it follows that an element with low Z would be required in order to reduce such production.

Initially one could think of hydrogen gas as the logical candidate however, as with any gas, the density at standard temperature and pressure (SPT) will be much lower than that of any solid. In order to increase the density, the pressure can be increased; but containment of high pressure gasses requires placing additional material in front of the gas which will inevitably cause scattering events unrelated to that which one intends to measure, as well as introducing a new set of safety concerns. Thus, the focus of attention will be on lithium, which is the material with lowest Z that is solid at STP.

Based on the NIST database [94], the amount of energy deposited per $\mathrm{cm}^2\mathrm{g}^{-1}$ is given for the two main types of interaction of photons with atomic lithium. It can be seen that Compton scattering is indeed the dominant interaction mechanism for a multi-MeV gamma-ray beam up to energies of 50 MeV. From figure 7.2, one can see that for energies < 20 MeV, the probability of Compton scattering is significantly higher than that of pair production. Beyond 20 MeV the likelihood of the interaction becomes similar (scattering of photons elastically becomes less than twice as likely than that of inelastic collisions). However, this is only part of the picture. In order to extract information about photons, one needs to understand their relationship to the direction and energy that electrons leave the lithium lattice with.

Equation 7.1 shows the Compton scattering formula.

$$\Delta\lambda = \frac{h}{cm_e}(1 - \cos\theta) \tag{7.1}$$

Where $\Delta\lambda$ is the change in photon wavelength, h is Planck's constant, c is the speed of light m_e is rest mass of the electron and θ is the angle of the scattered photon. From equation 7.1 it is trivial to calculate the energy transferred to the electron. Figure 7.3 shows that for high energy photons, the energy of the Compton-scattered electrons is insensitive to the scattering angle over a wide range and it is this which is exploited to form the basis for the spectrometer design.

While the primary Compton-scattered electrons are well correlated to the photon energy, the values shown in figure 7.2 demonstrate the need for thick lithium converters to ensure a usable level of conversion. In order to determine the effect of the lithium converter on the spectrum of the electrons escaping the lithium, a series of simulations have been performed using the Monte-Carlo code FLUKA [99, 100]. For these simulations we assume pencil-like monoenergetic photon beams of different energy E_γ (1.5, 2, 5, 7, 10, 15, and 20 MeV) incident upon 2 cm of lithium. Scattering of the electron in the lithium broadens the electron spectrum and results in a low energy tail. This effect can be mitigated by selecting a narrow acceptance angle. This was investigated by simulating 10 MeV photons incident on the 2 cm lithium and varying the acceptance angle of the

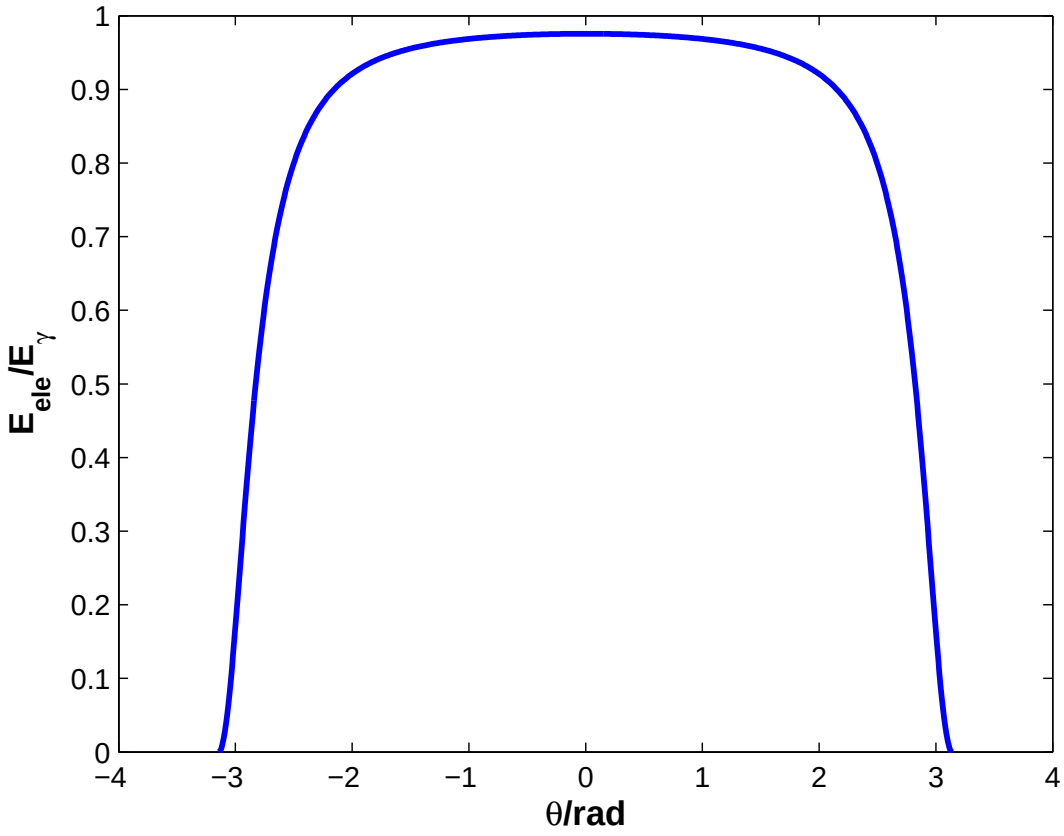

Fig. 7.3: Angular dependence of the energy of Compton scattered electrons for photon energy of 10 MeV [102].

electrons detected immediately after it.

From figure 7.4, it is clear that the shape of the peak is maintained for acceptance angles between 2π and 1 sr. With an acceptance angle of 0.2 steradians, the level of the low energy tail significantly reduces with only a minor reduction in the peak conversion factor; hence, the focus of attention will turn towards electrons which are forward scattered in narrow cones that give a reasonable compromise between spectral resolution and high signal yield (0.07 steradians).

Considering the dependence of the electron spectra on the incident photon energy; one finds a peaked distribution with a maximum at an energy approximately 1.6 MeV less than the incident photon energy E_γ. The full width half maximum increases with increasing photon energy and stabilises at a width of the order of 2 MeV at high energies plus a low energy linear tail for a 2 cm thick Li converter. The simulated spectra of this electron population for a range of initial gamma-ray energies are shown in figure 7.5. The spectral broadening and the emergence of the low energy tail is largely due to the straggling of electrons as they move through the converter and scatter. Thus, a trade-off

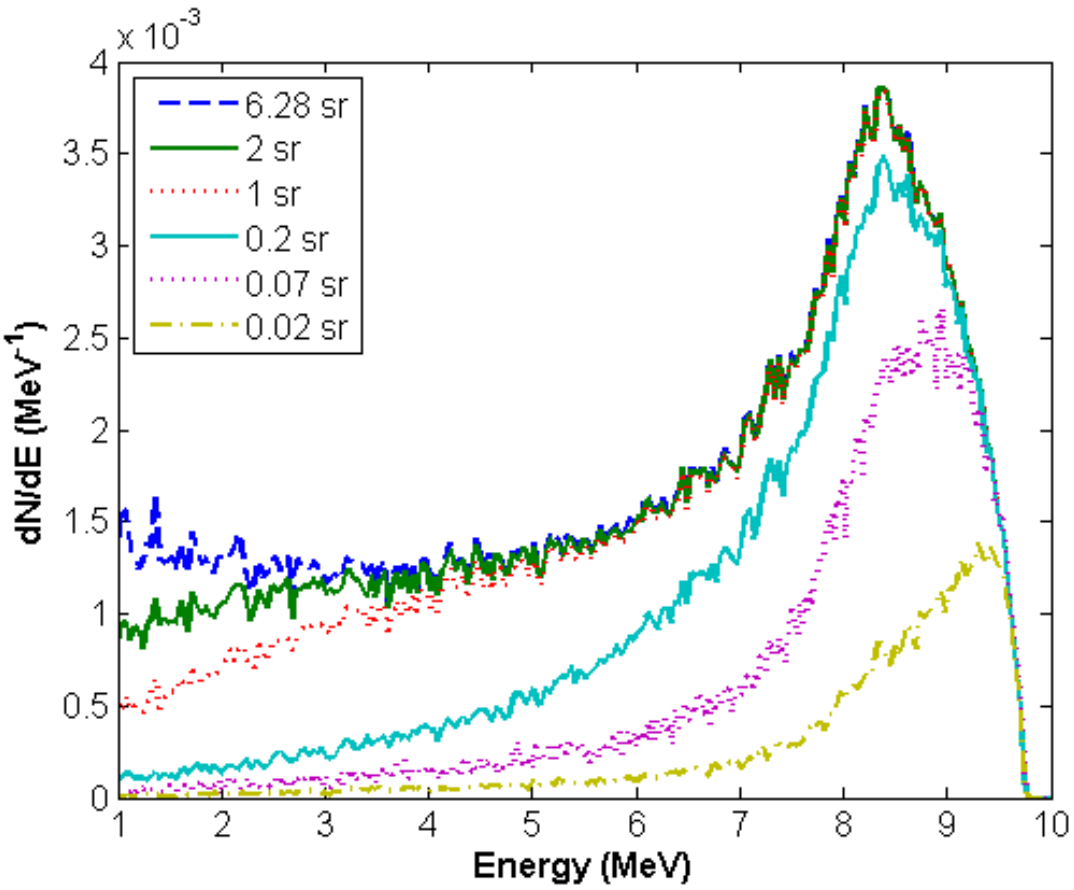

Fig. 7.4: Spectra of the electrons generated after the propagation of a pencil-like monoenergetic gamma-ray beam of 10 MeV through 2 cm of lithium for acceptance angles of 6.28, 2, 1, 0.2, 0.07 and 0.02 sr respectively. The y-axis corresponds to the number of electrons generated per incident gamma-ray photon per MeV.

exists between spectral resolution and yield.

Figure 7.6 shows the effect the various thickness of lithium for an interaction with 10 MeV photons. The thinner converters achieve a significantly narrower electron peak ($<$ 0.5 MeV) at the cost of a noticeable reduction in yield. Note that at lower photon energies the overlap of the response curves limits the achievable resolution and that alternative systems can be used in this energy range.

Using thin converters, deconvolution techniques allow for suitable energy resolution, while acceptable resolution at higher yields can be achieved with thicker converters. The thickness of lithium will largely depend on the flux of photons the user wishes to investigate. With high fluxes, a thinner target can be chosen; for our application a compromise of 2 cm was chosen. [103].

The simulations indicate a conversion efficiency into electrons of the order of 1.5 to 3% for a 2 cm target, depending on E_γ. Figure 7.7 shows the peak of the electron spectrum as a function of E_γ on a 2 cm thick target.

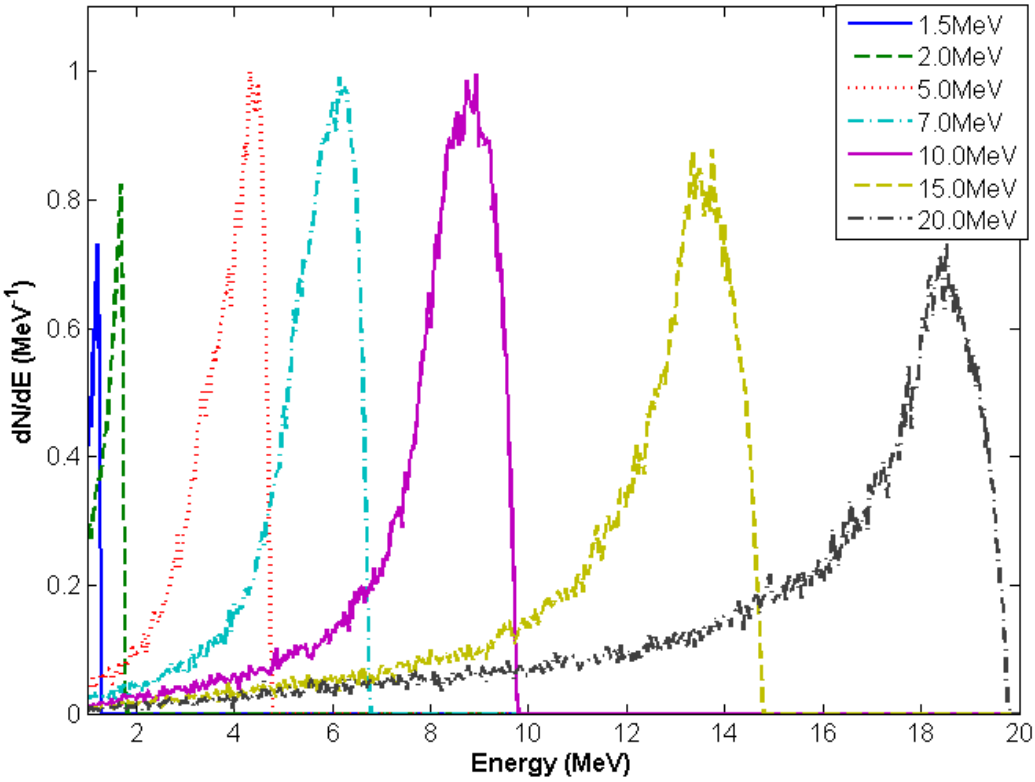

Fig. 7.5: Spectra of the electrons generated after the propagation of a pencil-like monoenergetic gamma-ray beam through 2 cm of lithium for energies of 1.5, 2.0, 5.0, 7.0, 10.0, 15.0 and 20.0 MeV respectively. The y-axis corresponds to the number of electrons generated per incident gamma-ray photon per MeV, normalized to the maximum peak. The angle of acceptance for electrons was 70 msr.

The peak position for the 2 cm thick target is well approximated in the region of interest by the function;

$$E_p = aE_\gamma + b \tag{7.2}$$

where E_p is the energy of an electron at the peak of the spectrum and the constant a and b are, respectively: $a = 0.93 \pm 0.01$, $b = (-0.25 \pm 0.01)$ MeV. The number of electrons produced per MeV per incident photon at peak energy is shown as a function of E_γ in figure 7.8.

The yield of electrons produced increases as the energy increases up to 5 MeV where it begins to plateau before once again decreasing. This is likely due to the electrons having absorbed higher energy and hence being scattered less before the conversion efficiency drops. Within the region of validity (between 3 and 20 MeV) a Gaussian gives a suitable approximation of the relationship between the peak value of the conversion factor to

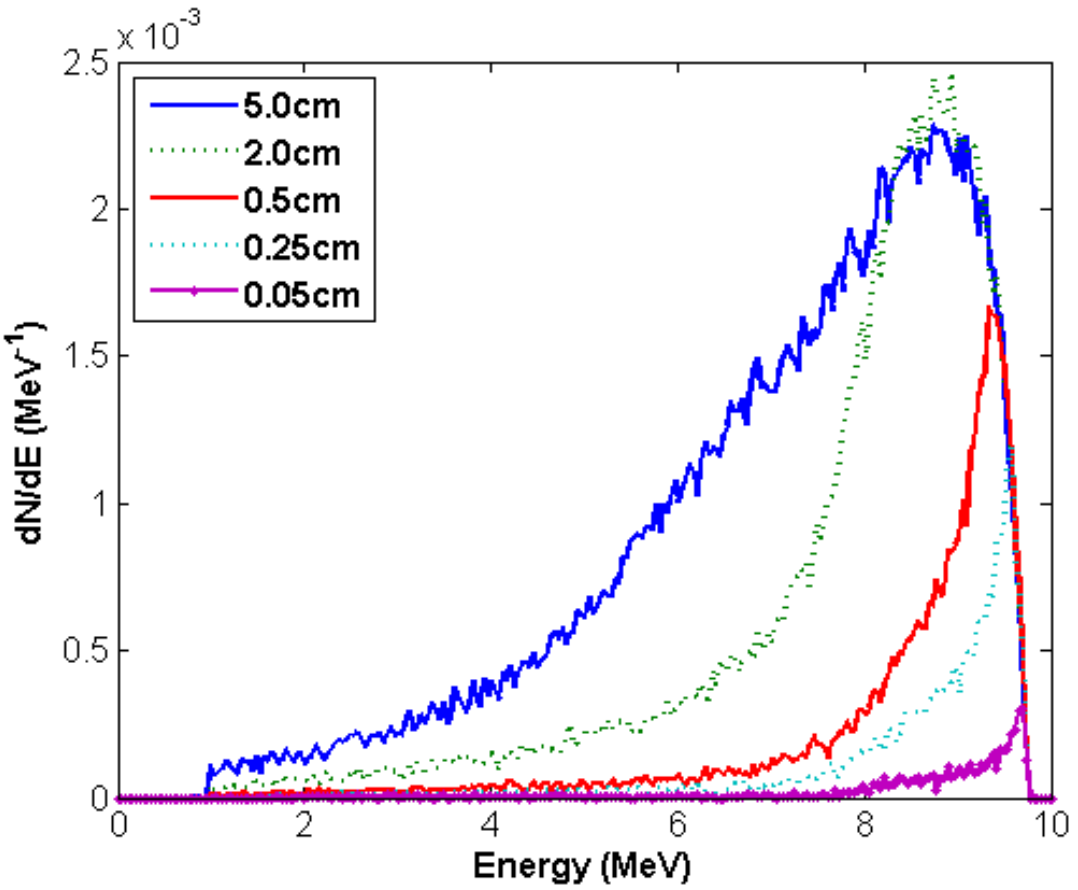

Fig. 7.6: Spectra of the electrons generated after the propagation of a pencil-like monoenergetic gamma-ray beam of 10MeV through a thickness of 5 cm, 2 cm, 0.5 cm, 0.25 cm and 0.05 cm of lithium (see legend for the target thickness simulated). The y-axis corresponds to the number of electrons generated per incident gamma-ray photon per MeV. The angle of acceptance for electrons was 70 msr.

within 5%:

$$\frac{dN_p}{dE} = C\exp[-\Big((E_\gamma - D)\Big)^2] \tag{7.3}$$

where N_p is the peak conversion factor value for electrons per incident photon in MeV^{-1}, $C = 0.0025 \pm 0.0001$ MeV^{-1} and $D = 9.3 \pm 0.5$ MeV. For poly-chromatic gamma-rays the expected spectrum will be a superposition of electron spectra, it is thus possible to parametrize the expected electron spectrum in terms of the flux and energy of the incident gamma-ray beam using the two equations provided. It thus follows that a deconvolution of the measured electron spectrum is possible to allow one to retrieve simultaneously, information regarding the flux and energy of the incident photons.

When performing a deconvolution, the low energy tail must be considered. In this specific case, a linear fitting may be used to describe this feature of the spectrum (before the Gaussian and after 1 MeV). This will allow the contributions from electrons in the

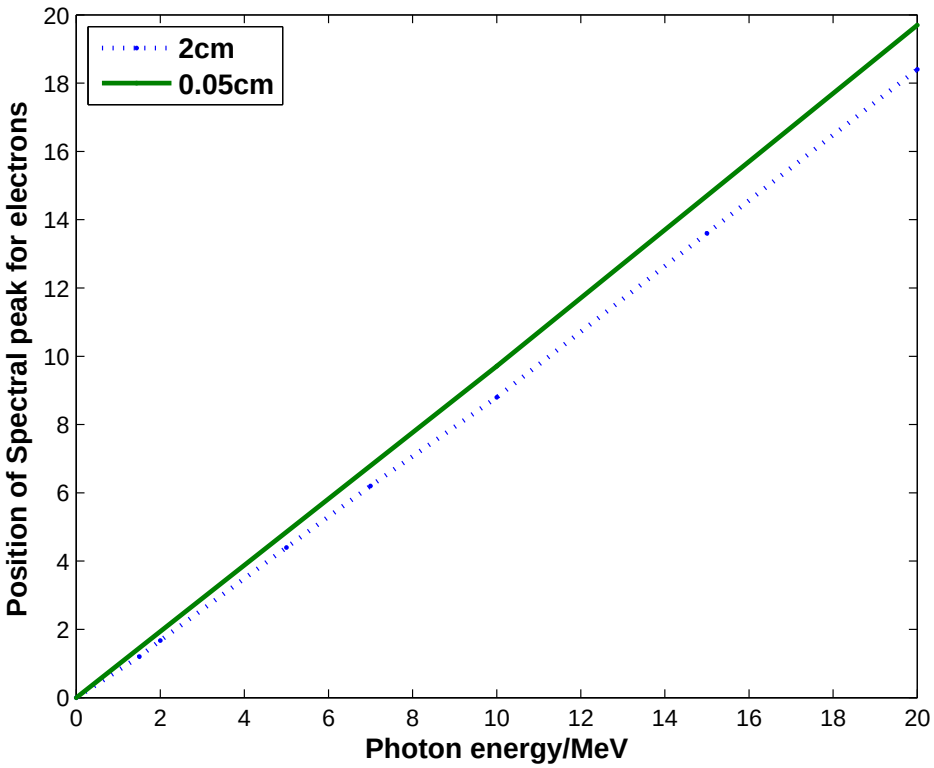

Fig. 7.7: Fluka simulations show a linear relation between the initial photon energy E_γ and the energy of the electrons escaping the lithium converter for thickness of 2 cm (blue dashed) and 0.05 cm (green solid).

low energy tail to be removed from the remaining electron spectrum and improve the accuracy of the gamma-ray spectrum obtained.

As a final remark, it is worth noting that, even if probability of pair production is significantly smaller than that of Compton scattering for $1 < E_\gamma[\text{MeV}] < 20$ (see figure 7.2), neglecting pair production effects introduces a small systematic error in extracting the photon spectrum once the spectrum of the scattered electrons is known. As an example, the plot in figure 7.9 shows the spectra of the electrons and positrons escaping from the rear surface of the lithium once a pencil-like monoenergetic gamma-ray beam with an energy of 10 MeV is incident upon it.

As we can see from figure 7.9, a small population of positrons is indeed generated. Integrating the positron and electron spectrum, we can see that the approximately 12 times more electrons than positrons escape the 2 cm thick lithium target. For thinner converter targets (0.5 cm and 0.05 cm), the low energy tail is almost entirely due to pair production and it is therefore possible to remove it entirely using this technique as long as the flux of incident gammas remains high.

FLUKA simulations indicate the spectra of electrons and positrons arising from pair

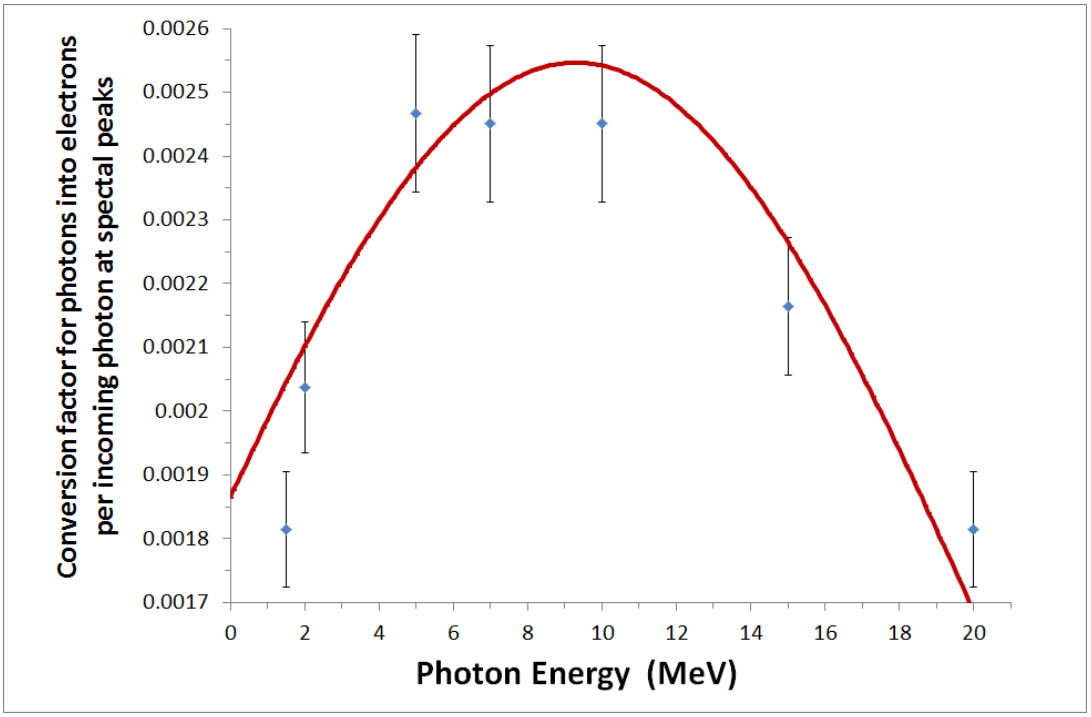

Fig. 7.8: The peak of the conversion factors in the electron spectra plotted as a function of the initial photon energy. A Gaussian fitting is applied to the trend.

production to be very similar, as theoretically expected [59]. The energy of the positrons is slightly higher than that of the electrons created via pair production (figure 7.9 shows a positron peak at 6 MeV). This is a result of the detector working in a photon range which is in the order of the energy required to initiate pair production and a break-down in the Born approximation leading to a loss of symmetry between the electrons and positrons created via pair production. To determine the exact energy contributions from the electrons would require and exact calculation of the Coulomb interaction of this 3-body system. The overall electron population will thus consist of the sum of the Compton-driven and pair-production-driven electron spectra. Neglecting pair production effects and assuming all the electrons to arise from Compton scattering will thus induce a systematic error in retrieving the gamma-ray spectrum in the order of 10% within the low energy tail. However, the contribution of electrons produced via pair production can still be approximated using the positron spectrum. A simultaneous measurement of the spectra of the electron and positron populations (see Section 7.3), allows for subtraction of the latter from the electron spectrum; thus, potentially eliminating this source of systematic error (details in section 7.2).

What has been demonstrated here is the principle of γ-ray interaction with a low Z material in order to produce an electron spectra. This is of course, not the full picture. Electrons scattered from this target need to be angularly selected and spectrally resolved.

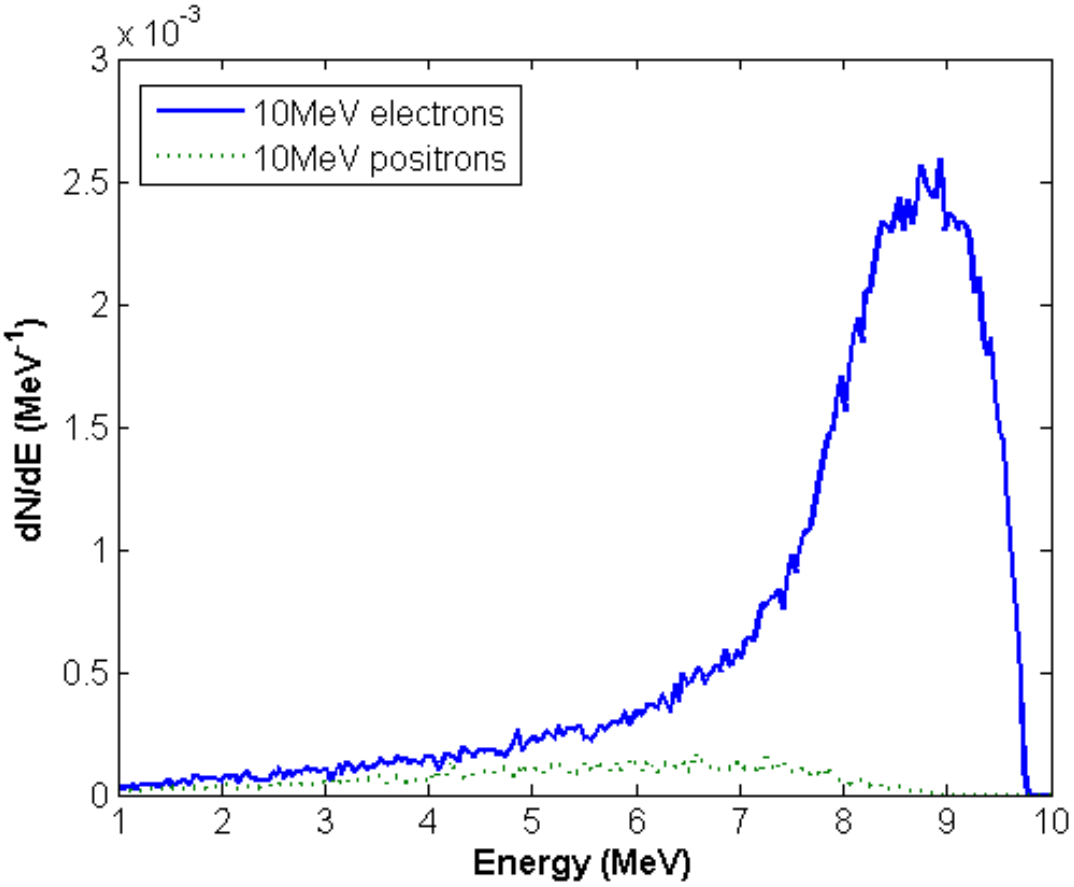

Fig. 7.9: Spectrum of the electrons (blue) and positrons (green-dashed) escaping from the rear surface of the lithium block of 2 cm thickness once a pencil-like monoenergetic gamma-ray beam with an energy of 10 MeV is incident on it. Results are expressed in number of particles generated per incident gamma-ray photon per MeV.

7.2 Behaviour of Particles After Interaction with Lithium

In the previous section, attention was focused exclusively on the electrons which are emitted on the same axis as the incident gamma-ray beam. This is in principle over-simplifying, since it is well known that Compton scattering present a broad angular distribution as is shown in figure 7.3. Electrons will thus be emitted also wider angles, with an energy that gradually decreases as we move far from the axis of the gamma-ray beam. Those electrons thus, represent a source of noise for the detector and should be suppressed. Compton scattering will also induce a broadly divergent population of scattered photons, which are again a detrimental source of noise when attempting to measure the spectrum of the scattered electrons. These qualitative arguments are quantitatively corroborated by figure 7.10, which show the spatial photon (7.10a) and electron (7.10b) distributions, as resulting from FLUKA simulations, once a pencil-like monoenergetic gamma-ray beam with an energy of 10 MeV interacts with a 2 cm thick lithium block.

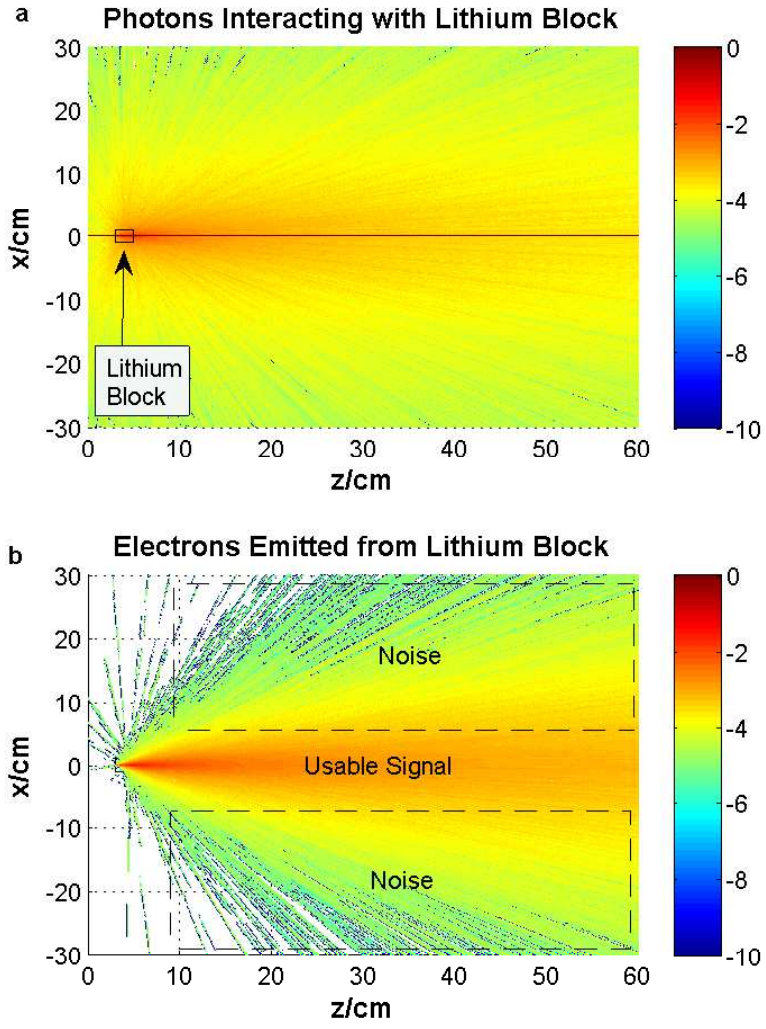

Fig. 7.10: Spatial distribution of photons (a) and electrons (b) after the interaction of a 10 MeV gamma-ray beam with a 2 cm thick lithium cube. In both cases, the colourbar represents the number of particles per incident photon per cm (x-axis) expressed as a base 10 logarithm.

As we can see the vast majority of photons pass through the lithium block without interacting (less than 98% of the initial photons). Also, a population of scattered photons will be isotropically emitted by the lithium (approximately 10^{-3} or 10^{-4} photons per incoming gamma-ray photon). The situation is analogous for the scattered electrons. As can be seen from figure 7.10(b), the electron spatial distribution consists of two main parts: a relatively strong population of forward scattered electrons (labelled as usable signal in figure 7.10(b)) and a wider distribution of electrons scattered widely at both sides of the lithium (labelled as noise in figure 7.10(b)). This latter population must be suppressed if a good signal-to-noise ratio is to be achieved with the detector. The easiest way to deal with this noise is to introduce a thick lead shielding immediately adjacent to

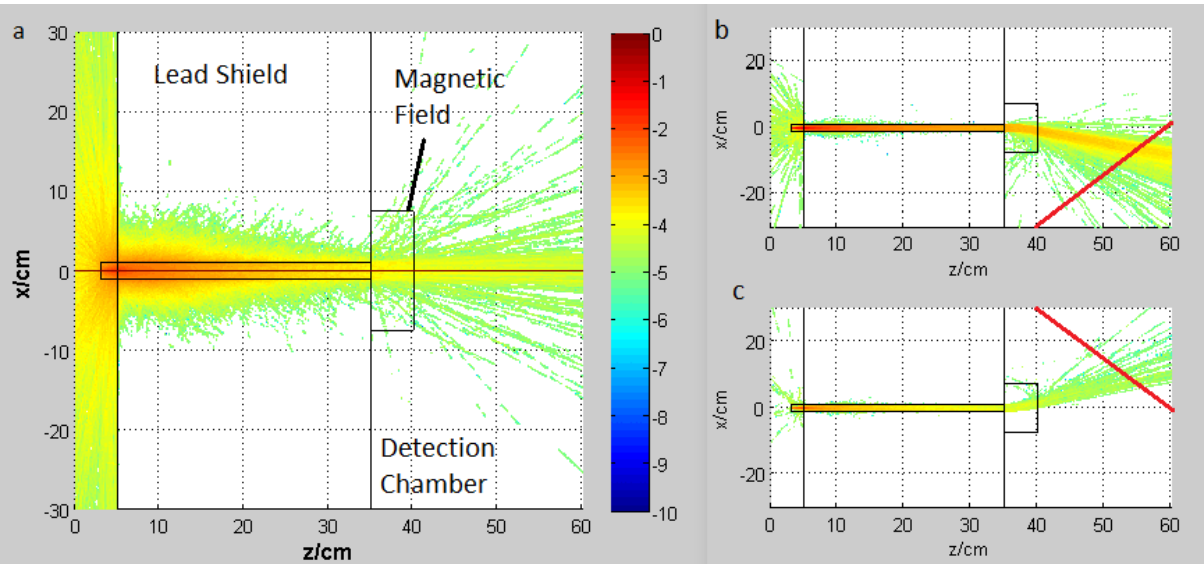

Fig. 7.11: Spatial distribution of photons (a), electrons (b) and positrons (c) after the interaction of a 10 MeV gamma-ray beam with a 2 cm thick lithium cube once the lead shielding and a 5 cm-long 0.3 T magnetic field is inserted. The colourbar represents the number of particles per incident photon per cm (x-axis) expressed as a base 10 logarithm. The red lines in b and c indicate the possible locations of an imaging plate or LANEX screen.

and at either side of the lithium. If we assume a 30 cm thick lead wall with an aperture in the middle of the same size as the lithium block, almost all the off-axis scattered electrons and photons are effectively absorbed in the lead. This is shown in figure 7.11 which depicts the simulated photon, electron, and positron spatial distribution for the same initial conditions as the ones used for figure 7.10, with the only difference that a 30 cm lead wall has been now inserted at each side of the lithium block.

Whilst, the photon signal on axis has obviously not been affected by this shielding, the off-axis noise has dropped by several orders of magnitude (see figure 7.11). If we now insert a magnetic field at the rear of the lead shielding, we can effectively separate, and spectrally resolve, the electrons and the positrons (see figure 7.11). The spectrally separated electrons and positrons can then be recorded on a suitable, spatially resolved detector, such as an Image Plate or a LANEX screen placed at locations indicated by the dashed lines in figure 7.11 (b) and (c) [84, 85, 79].

Recalling the work presented in Section 6.1 regarding the use of magnets as a means of spectrally resolving relativistic electrons and specifically equation 6.7, one is reminded that ideally a small aperture, a strong magnetic field, and a long distance between the source and the detector are ideal in order to improve the spectral resolution. However, it is clear that all these parameters significantly decrease the yield of particles on the detector. A trade-off must then be found between a good spectral resolution and a good signal on the detector. Calculations show that a reasonable compromise is found for

$B = 0.3$ T, $L_m = 5$ cm, $\theta_s \approx 30$ mrad, $D_s = 1$ cm, $D_d = 25$ cm (see figure 7.10).

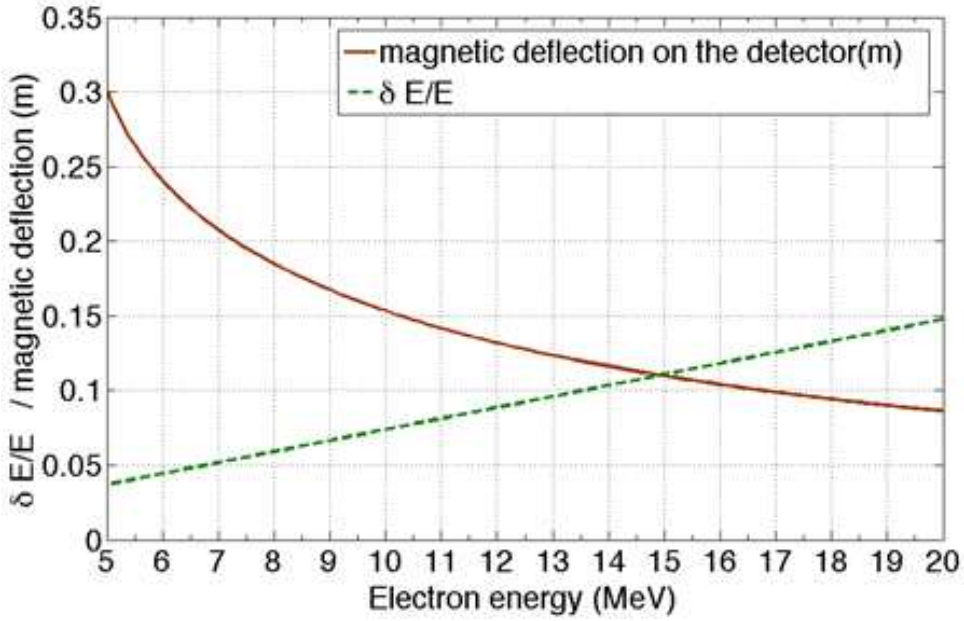

Fig. 7.12: Relative energy resolution (dashed green line) and spatial deflection on the detector (solid brown line) of the scattered electron population after propagation through a 5 cm long, 0.3 T magnet. Details in the text.

As expected, the energy resolution decreases as the electron energy is increased. However, a relative energy resolution of 4% and 12% are found for 5 MeV and 15 MeV, respectively (energy resolution of 0.2 MeV and 1.8 MeV, respectively). This energy resolution is less than or comparable to the intrinsic energy resolution during the conversion of gamma-ray photons to electrons in the lithium target (see figure 7.12). The resolution of the magnetic spectrometer can also be improved by positioning the detector further away, but at a cost of reduced compactness. As a final remark, it is interesting to note that the vast majority of the gamma-ray photons are able to escape unperturbed from the detector (more than 97%). This allows for simultaneous detection of the spatial profile of the gamma-ray beam, if a suitable detector is placed on axis.

7.3 Final Design and Conclusions on the Lithium Detector

A proposed setup for the detector is depicted in figure 7.13. The gamma-ray photon to be measured is incident upon a 2 cm thick lithium block surrounded by 30 cm of lead shielding with a 1×1 cm^2 aperture. The entire device shown in figure 7.13, including the shielding is 60 cm long and hence, able to fit conveniently into most laboratories.

A population of electrons and positrons is generated, the latter arising from pair production in the nuclear field whereas the first generated partially by pair production

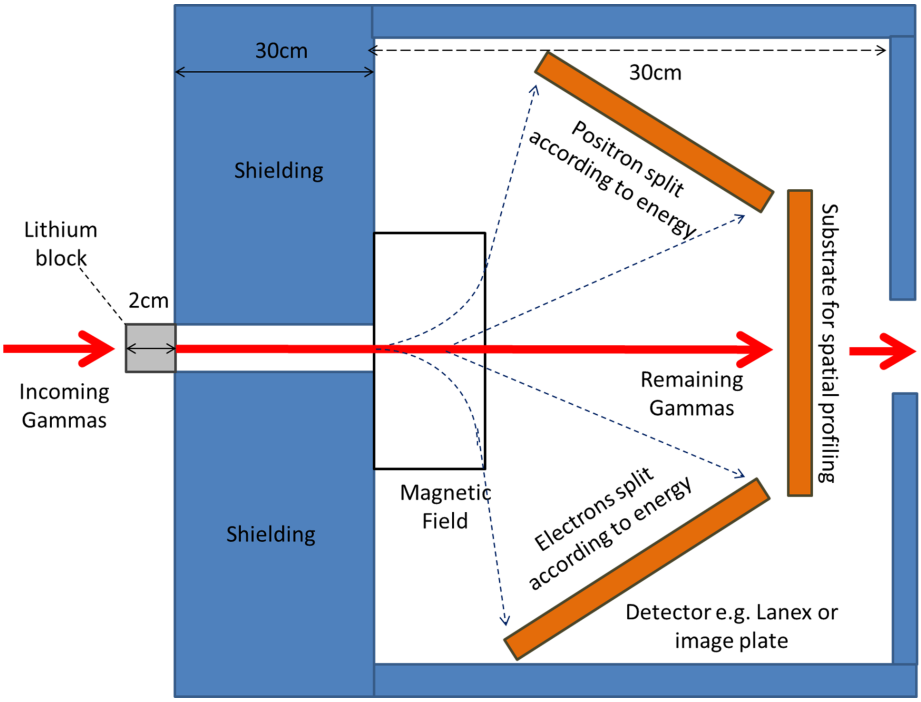

Fig. 7.13: The proposed setup for the gamma-ray spectrometer (not to scale). Image plates can sit off axis in order to detect the charges deflected. On axis, a substrate can be placed for spatial profiling.

and mostly by Compton scattering. For a gamma-ray energy window of $1 < E[\text{MeV}] < 20$, Compton scattering is dominant (see figures 7.2 and 7.9) allowing for effects due to pair production to be neglected (less than 10% of the overall electron yield).

The scattered electrons will have an energy distribution that resembles that of the incident gamma-ray beam (bell-shaped distribution plus a linear low-energy tail, see figure 7.6). The electron distribution can be parametrized as a function of the flux and energy distribution of the incident gamma-ray beam (see figure 7.6 and 7.7), allowing for deconvolution of the electron signal. Once the electron spectrum is measured by a magnetic spectrometer, the spectrum of the incident gamma-ray beam can thus be retrieved with a resolution of the order of the MeV (see figure 7.12). The lead shielding allows for fine selection of the scattered electrons and reduces the off-axis noise induced by photons and particles scattered at a wide angle (see figure 7.10 and 7.11).

In conclusion, the design for a compact gamma-ray spectrometer suited for high-flux gamma-ray beams is presented. The system has an energy resolution of the order of one MeV in an energy window of $3-20$ MeV. The performance of the detector is analysed by Monte-Carlo simulations. The system has been tested in recent experimental campaigns confirming the numerical predictions presented in Chapter 9.

8. TEMPORALLY OVERLAPPING MULTIPLE BEAMS

It has been shown that by using the relatively broad frequency envelope of a femtosecond laser pulse, detailed information about the phase front and relative time delay between two collimated laser pulses could be revealed by employing an interferometric technique provided prior knowledge of a reference beam parameters was obtained [104, 105]. Exploiting similar physical principles, a compact and versatile experimental technique has been designed which allows for the precise measurement of the temporal delay between two short laser pulses at their focal planes. This technique can simultaneously allow for micron scale overlapping in the plane perpendicular to the axis of propagation of the pulses. The proposed technique can be implemented in virtually any focusing geometry and relative intensity of the two pulses.

Not only is the technique highly beneficial for experiments into NLTS but should also prove extremely useful any multi-beam experiment to be routinely performed on the next class of multi-petawatt laser systems such as the 20 PW Vulcan at RAL [106] and ELI [60].

8.1 Theoretical Rationale

The electric field of an electromagnetic wave can be expressed generally as $E = E_0 e^{-i(k\cdot r-\omega\tau-\phi_0)}$ where E_0 is the peak electric field strength, k is wavevector ($2\pi/\lambda$ where λ is the wavelength of the pulse), r is the displacement vector from the source to the point of observation, ω is the frequency of the wave, τ is the time of observation of the pulse and ϕ_0 is a constant. The general equation describing the intensity of electromagnetic radiation is given by $I = c\epsilon_0 |EE^*| /2$ where c is the speed of light and ϵ_0 is the permittivity of free space. From figure 8.1, it can be seen that the superposition of two electromagnetic waves with a similar peak field strength E_0, gives an intensity

$$I = c\epsilon_0 E_0^2 \left| 1 + \cos\left[(k_1 \cdot r_1 - k_2 \cdot r_2 - \omega_1\tau_1 + \omega_2\tau_2 + \phi_1 - \phi_2)\right] \right| \tag{8.1}$$

If we consider the first wave to be propagating along r_1 and the second wave to be propagating at an angle θ separated by y with respect to this so that $r_2 = r_1 + y\sin\theta$ (where y is the distance separating the two sources of the waves), and the waves to have

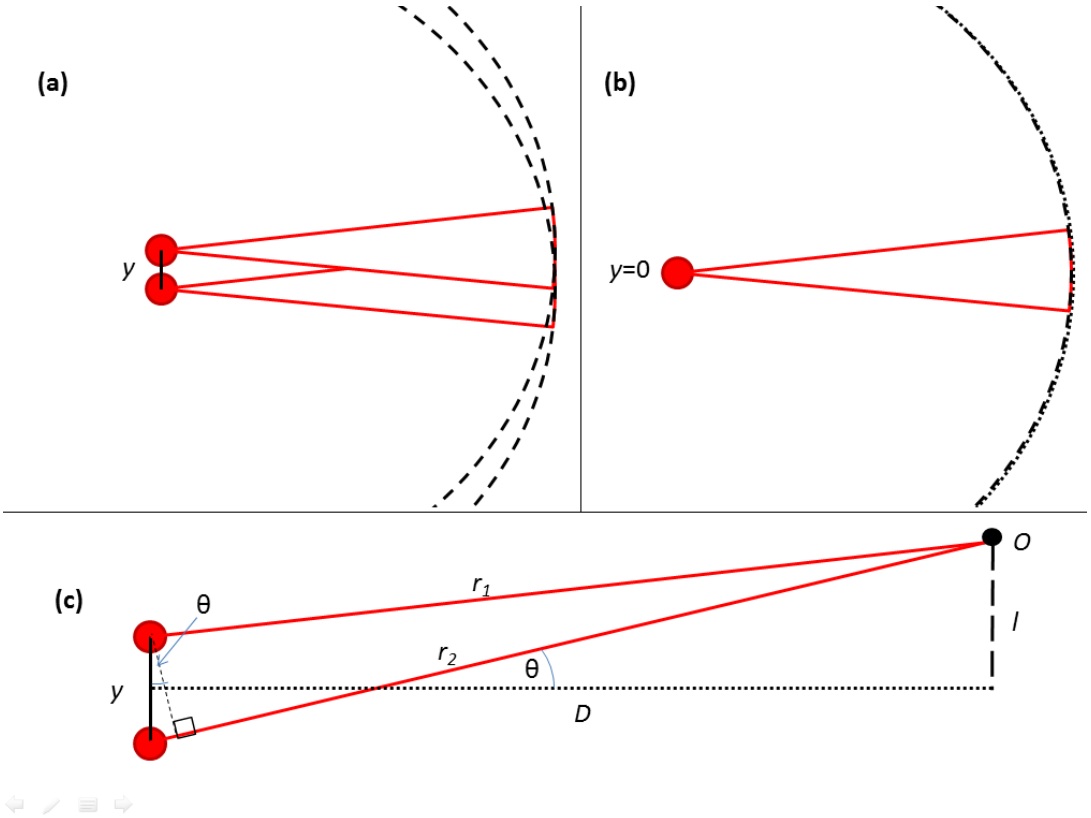

Fig. 8.1: The sources of two spherical wavefronts are separated in space by a transverse distance (a) y or (b) $y = 0$, (c) an angular difference can be seen by an observer at O.

identical frequencies, with a temporal delay related by $\tau_2 = \tau_1 + \Delta\tau$, then the Eq. (8.1) becomes

$$I \propto \left|1 + \cos[ky \sin\theta - \omega\Delta\tau + \phi]\right| \tag{8.2}$$

In equation 8.2 the notation 1 has been dropped for convenience, in addition the constants have been replaced by $\phi = \phi_1 - \phi_2$. This equation can be thought of as consisting of two distinct parts, a spatial component which varies periodically with θ and a temporal component which varies periodically with $\Delta\tau$ demonstrating that equation 8.2 varies periodically.

If we consider two realistic laser pulses of identical bandwidth $\Delta\lambda$ and central wavelength λ_0, the use of a diffraction grating allows two pulses to interfere spectrally many pulse durations apart. If the diffraction grating disperses the various spectral components in one axis only, then this behaviour will only manifest in the dispersion axis [104]; let this phase term be $\vartheta = \omega\Delta\tau$.

In order to improve the resolution of the system, a lens can be used after the grating. The focussing power of the lens will smooth modulations induced by the spatial interfer-

ence along the axis of dispersion. A cylindrical lens allows one to remove this information in one axis while allowing it to persist in the other. Hence, the phase term representing spectral information ϑ, appears exclusively along the dispersion axis.

In the undispersed, unfocused (with respect to the cylindrical lens) axis, perpendicular to the axis in which spectral components manifest, the spatial contributions are present while spectral components are not. Considering the simple 2-point source diffraction equation from Young's Double slit experiments (see figure 8.1) the spatial terms can be written as $\varphi = ky \sin\theta$.

In order to determine the intensity for an observer at any point, the solution will be proportional to the cosine of the sum of the temporal domain ϑ and spatial domain φ as shown below.

$$I(\vartheta, \varphi) \propto \left|1 + \cos(\vartheta + \varphi)\right| \tag{8.3}$$

Equation 8.3 allows one to make a prediction of the interference pattern that would be observed if a CCD were placed in the arrangement.

8.2 TARANIS Femtolab Setup for Relative Timing Measurements

The TARANIS femtolab at Queen's University Belfast (QUB) [107], employs a MIRA 900f ultrafast laser from Coherent's Verdi range [108]. The gain medium is a titanium:sapphire crystal that can be tuned from 700 to 900 nm. The optical cavity utilizes changes in the self focusing in the Kerr medium to attain higher gain when mode locked in this way. Group velocity dispersion is compensated for by the use of intracavity prisms, this allows the laser to operate with a pulse duration of $T_0 = 140$ fs [109]. The system is setup to produce energy of 6.6 nJ and within this time and has a repetition rate of the system is 76 MHz. The central wavelength is selected to be 800 with 32 nm FWHM. The beam diameter exiting the system is 0.8 ± 0.1 mm with a divergence of 1.7 ± 0.2 mrad.

The pulse is expanded to a size of 20 ± 1 mm so as to fill the majority of the parabolic mirrors used for focusing the beam. One of these parabolic mirrors is on a stage to allow the relative position of the foci of the mirrors to be altered. Once the desired separation is set, this stage is locked in place. The pulse is incident on a $50:50$ beam splitter and two subsequent paths are followed. The paths followed are given in figure 8.3. As shown in figure 8.3, one of the paths includes a micrometer stage which controls the spatial separation of the focal spots, while the other contains a micrometer stage with two of the mirrors that allows the relative timing to be changed by a path length increase/decrease to be imposed. Parabolic mirror 1 has additional x and y micrometer stages in order to make adjustments to the relative position of the focus at the pellicle.

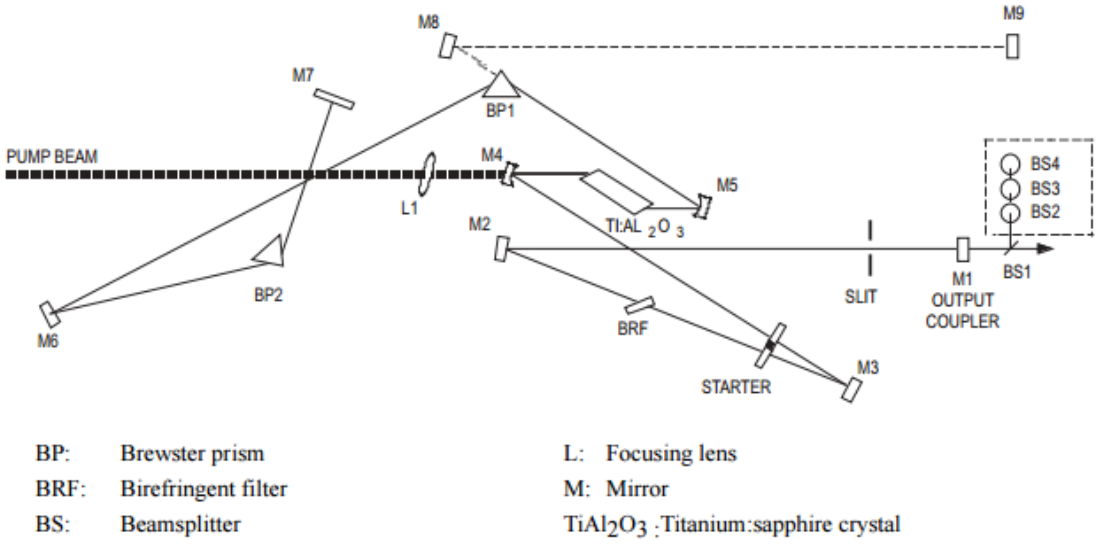

Fig. 8.2: The internal workings of the MIRA 900f [109, 108].

8.3 Temporal Overlap of two Spatially Overlapped Foci

8.3.1 Experimental Setup for Spatially Overlapped Pulses

In most modern laser facilities, the intensity of laser pulses is greatly increased by focusing via parabolic mirrors. The rise of dual-pulse, counter-propagating geometries such as that

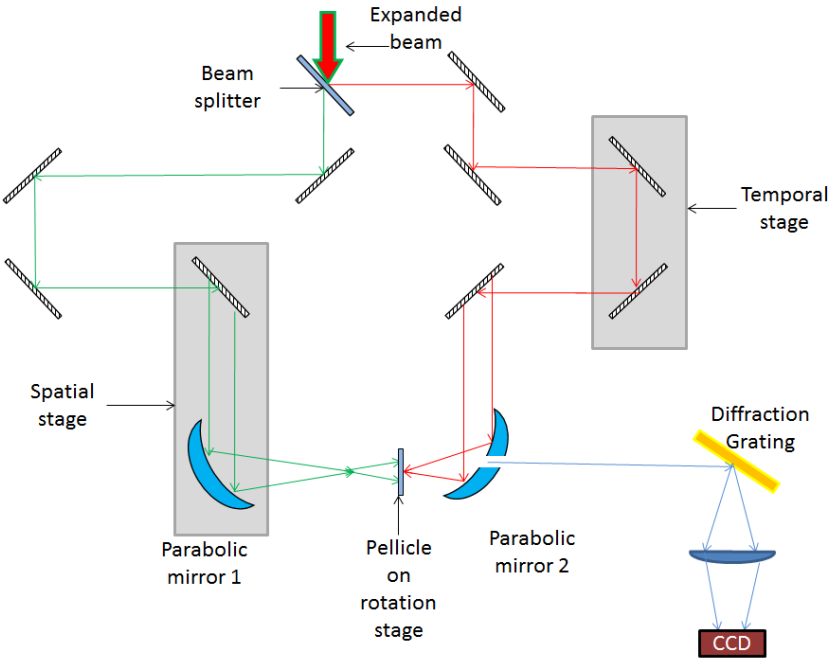

Fig. 8.3: The beam paths followed for the spectral interferometry setup.

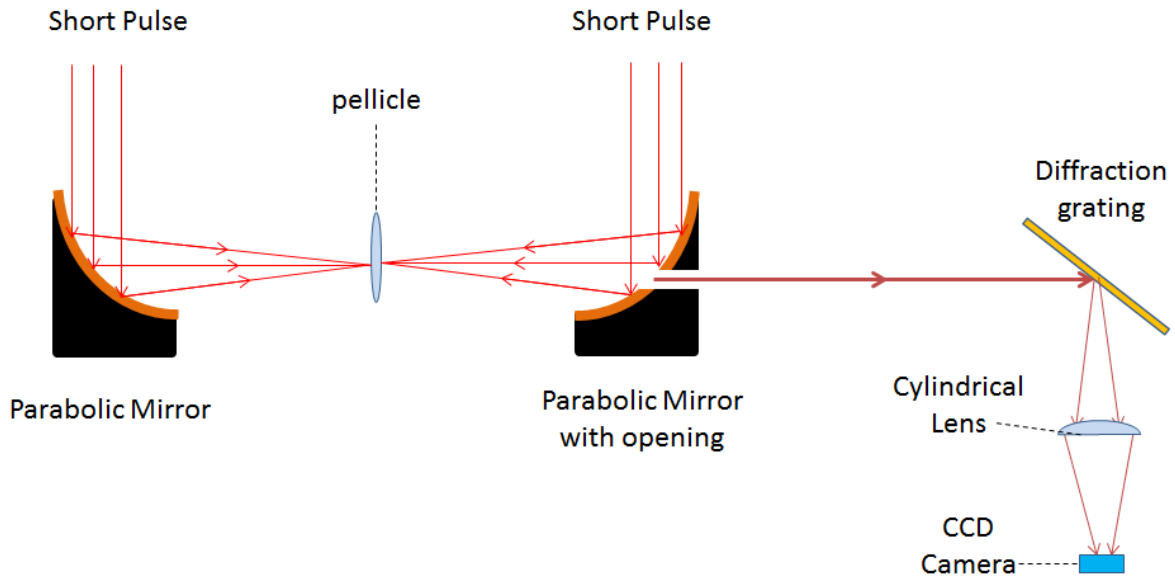

Fig. 8.4: Two counter-propagating laser pulses are incident on the pellicle whose surface closest to the parabolic mirror with the hole represents the point at which temporal delay is measured. The pulses propagate towards a diffraction grating.

shown in reference [43], may require the employment of such mirrors which have been modified with features such as a hole in their centre in order to allow electrons generated by laser wakefield acceleration to propagate unhindered by the physical presence of the mirror. Therefore, the technique outlined in Section 8.1 was investigated specifically for a counter-propagating arrangement where two pulses are required to arrive simultaneously at a point; this is marked by the placement of a thin pellicle (see figure 8.4).

In this arrangement, a 50.8 mm parabolic mirror of focal length 101.1 mm with a 3 mm hole in the substrate, and 8 mm at the point of exit at the back of the mounting, is focused onto surface of the pellicle. The pellicle is angled very slightly to allow the reflection off the surface to propagate through the opening in the parabola. The second pulse is focussed by a second parabola of the same parameters (without the hole at it's centre) and is transmitted on axis through the pellicle. The transmitted and reflected components of the pulses which propagate through the hole in the parabola and are incident on a diffraction grating of 800 lines per mm which is placed 530 mm from the back of the holed parabola and angled such that the first order reflection of diffraction from it is 50 mm from a cylindrical lens of focal length 50 mm. A CCD is placed 60 mm after the lens.

To improve the fringe contrast seen by the CCD, one may require a method to control the relative intensities without inducing any path difference in one pulse with respect to the other, for this identical polarisers can be placed into the arrangement, one before each

parabolic mirror if the beams are polarised in the same plane (where one can be screened out with respect to the other), or one directly after the hole for the case of cross polarised pulses (to allow simultaneous control of relative intensities and allow the two pulses to gain common axial components). The sampled components of the pulses are incident on a diffraction grating then propagate through a cylindrical lens. This destroys any spatial information gained in the arrangement while simultaneously allowing the resolution of the components to be improved. The CCD reads out the intensity pattern arising from the pulses. This is shown in figure 8.4.

Using the specifications of the TARANIS oscillator outlined in the first section expectations of an intensity pattern of two overlapping pulses can be determined. Initially the focal spots of the two pulses are overlapped using a thin wire and CCD camera as is standard in most laser facilities. If the pulses are overlapped perfectly, y and θ both drop to 0. This means that there are no spatial terms in equation 8.3; a prediction is shown in figure 8.5.

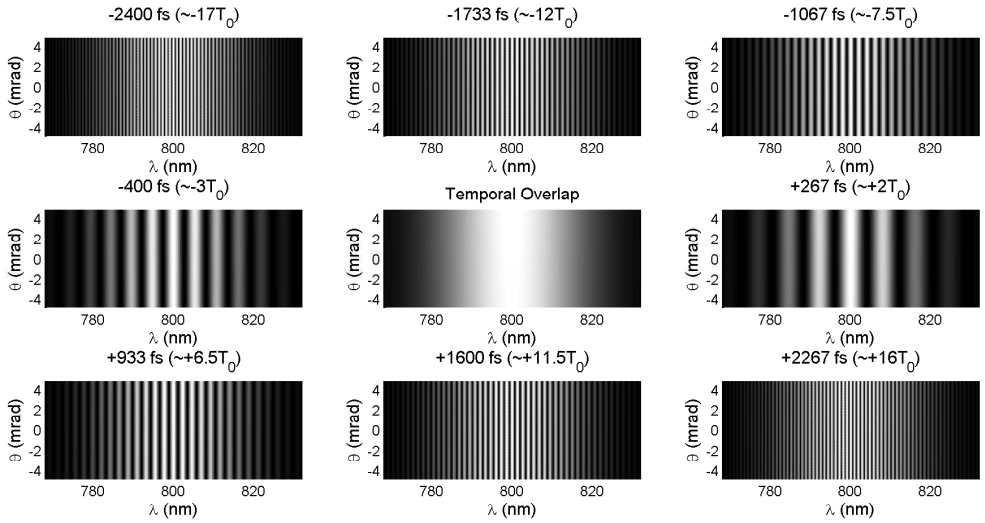

Fig. 8.5: Prediction of fringe patterns at perfect spatial overlap.

As can be seen in figure 8.5, when the time delay is increased, the fringe separation decreases also. The vertical axis representing the relative angle the observer is at from the common centre of the origin of the two pulses θ and the and the horizontal axis representing the wavelengths λ present, the relative intensity is plotted. The 9 images begin from the top left at a time delay of $-2400(\sim -17T_0)$, $-1733(\sim -12T_0)$, $-1067(\sim -7.5T_0)$, $-400(\sim -3T_0)$ fs before best temporal overlap is reached. The process then proceeds to times of $+267(\sim 2T_0)$, $+933(\sim 6.5T_0)$, $+1600(\sim 11.5T_0)$ and $+2267(\sim 16T_0)$ fs. It can be seen that the fringes are vertical in orientation and begin compressed. The reduction of the temporal delay leads to the broadening of the fringes until temporal

overlap where the the broadening tends to a single fringe which stretches over the full bandwidth. After this point, increasing the temporal delay leads to a compression of the fringes, mirroring the behaviour of the fringes prior to temporal overlap. Far from temporal overlap, the fringes tend towards being infinity close and are unable to be resolved, in this setup, this occurred at $\sim 20T_0$.

Figure 8.5 represents the case where the foci of the pulses are perfectly overlapped; in the case where the offset is set to 250 μm, one can see the change that occurs to the pattern governed by equation 8.3 is entirely due to $\vartheta \neq 0$. This results in a fixed firing pattern being present in the θ axis. As the φ remains unaffected, the pattern becomes modified such that the fringes are now angled (this angle will be specific to the distance of the CCD from the pellicle). Assuming a CCD at a distance of 1.0 m from the pellicle, a fringe pattern is given in figure 8.6.

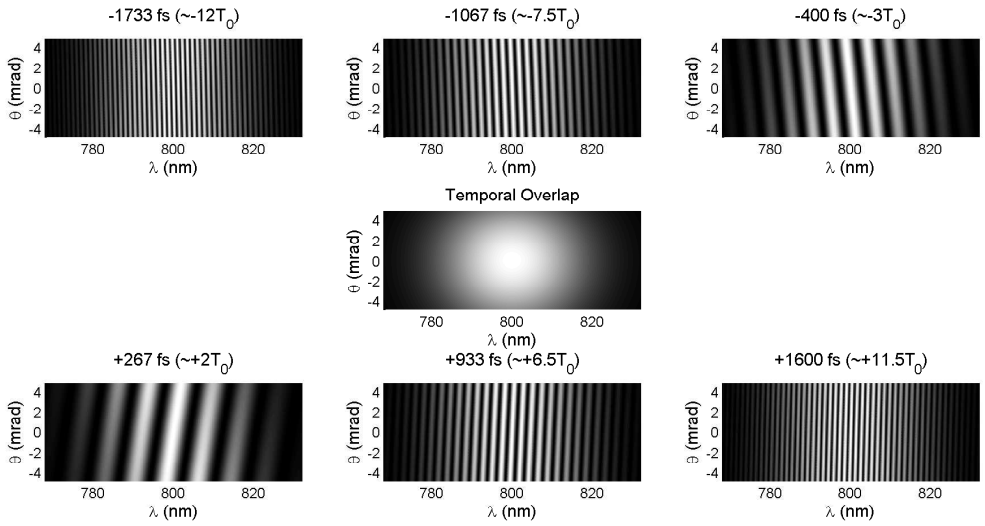

Fig. 8.6: Prediction of fringe patterns with spatial mis-match of 250 μm.

As demonstrated in figures 8.5 & 8.6), for each time delay given, a unique number of fringes is present along the λ axis. The number of these temporal fringes which are present is of course related to the bandwidth of the system being used; however, as a consequence of this, simply counting the number of temporal fringes present the user is able to obtain information regarding the relative temporal mis-match of the pulses.

8.3.2 Results for Spatially Overlapped Pulses

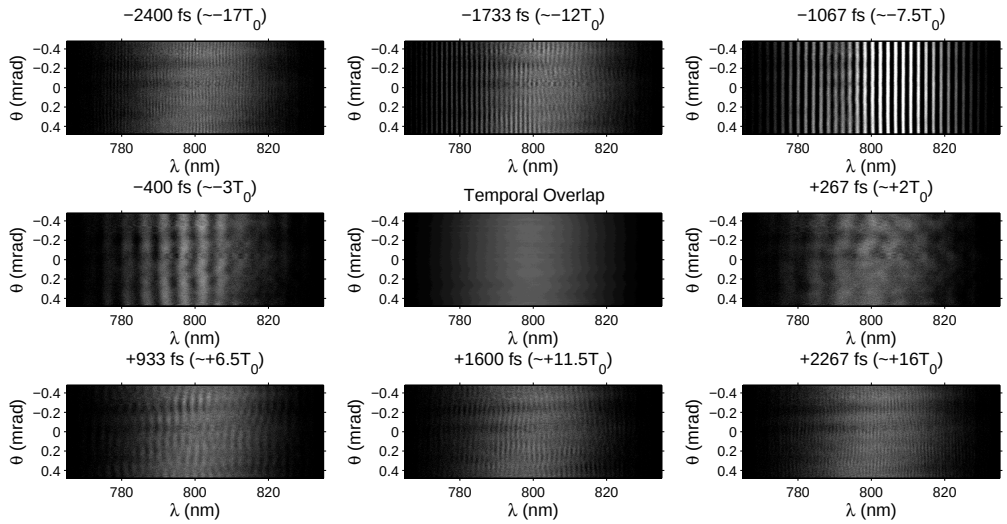

Fig. 8.7: Results of the temporal matching process as seen on the CCD camera.

Using the setup presented in the previous section, results were obtained in order to make a comparison with the theoretical expectations. Looking at figure 8.7, one can see the changes that occur on the CCD camera close to temporal overlap. The 9 images begin from the top left at a time delay of $-2400(\sim -17T_0)$, $-1733(\sim -12T_0)$, $-1067(\sim -7.5T_0)$, $-400(\sim -3T_0)$ fs before temporal matching occurs. The process then proceeds to times of $+267(\sim 2T_0)$, $+933(\sim 6.5T_0)$, $+1600(\sim 11.5T_0)$ and $+2267(\sim 16T_0)$ fs. The central image shows the pattern obtained at temporal overlap.

Progressing from the upper left to the central image in figure 8.7, one can see the fringes begin to expand until temporal overlap; at this point, no fringes can be seen. This is within the expectations discussed previously in Section 8.1. Continuing through the images from the central image to lower right of the figure, the behaviour of the fringes is mirrored and the fringes begin to once again, compress.

Using figures 8.5 & 8.7, a comparison between the number of temporal fringes expected theoretically and those obtained experimentally along the λ axis was made. Figure 8.8 shows that a similar number of fringes are present in the experimental findings to the number predicted in the theoretical model presented in figure 8.5. The number of fringes determined experimentally are generally lower than those predicted; however, this is most likely due to the poor contrast of the fringes in the peripheral regions of the images. The gradient of the graph presented in figure 8.8 is shown to be $|\Delta\omega|$ i.e., the modulus of the range of frequencies contained within the pulse packet. In terms of the bandwidth of the

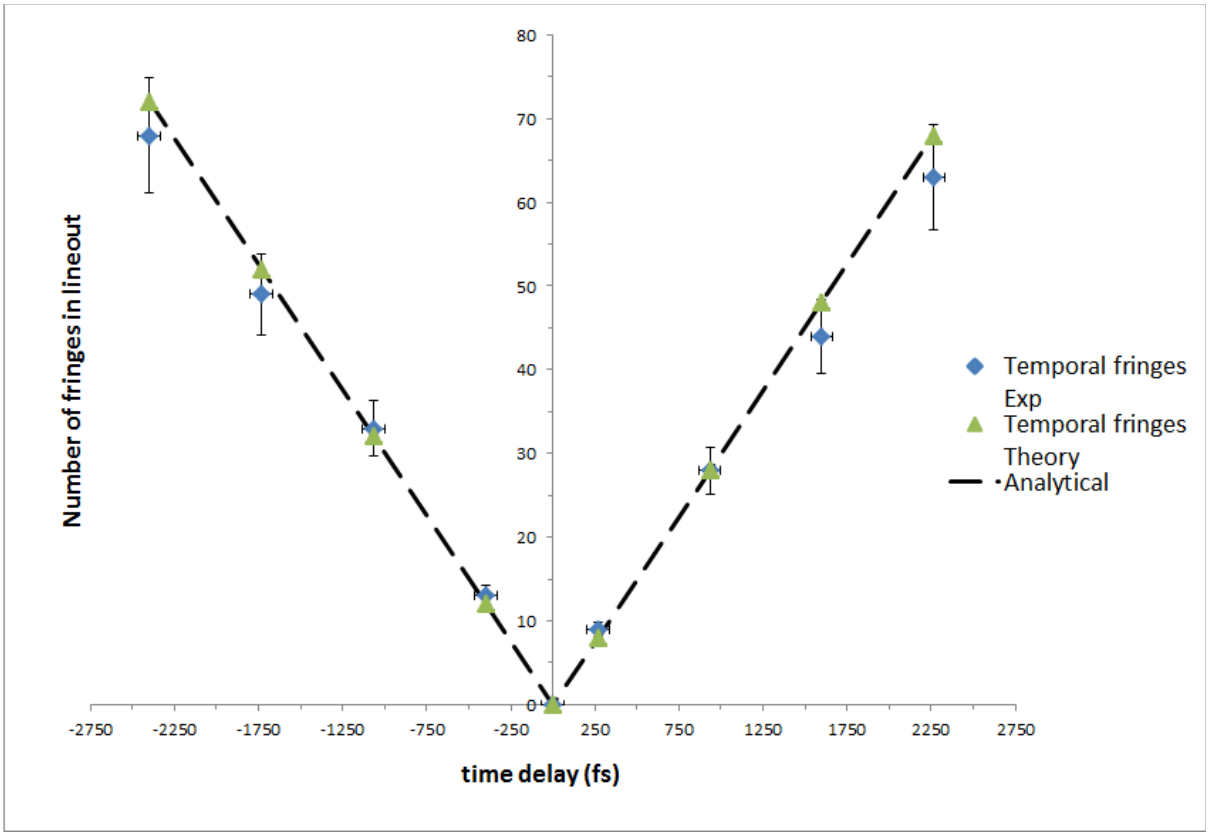

Fig. 8.8: A comparison between the theoretical expectations of the number of temporal fringes predicted (green) in the model presented in Fig. (8.5) and the number of fringes detected in the experimental setup (blue). The line represents the gradient of $c|\Delta\lambda/\lambda_L^2|$.

laser, this is approximately

$$\frac{N}{\Delta\tau} \approx \left|\frac{c\Delta\lambda}{\lambda_L^2}\right| \tag{8.4}$$

Where N is the number of fringes that are observed on the CCD. This result demonstrates that a user is able to establish with the most basic information about a laser system, the time delay between two pulses. By varying the number of fringes on the CCD, one can determine the delay between two intense laser pulses. In figure 8.8 the uncertainty in the number of fringes detected can be attributed to the poor contrast seen at the edges of the intensity pattern on the CCD and estimated at $\sim 10\%$. By carrying out a Fourier analysis on the fringe pattern, in order to extract the separation, the results are extremely similar; however, this technique improves the accuracy to $< 1\%$ (results presented by C. Hyland MSci Project 2016). It is important point to note that one of the strengths of the technique lies in requiring no prior calibration which can save valuable time in an experimental environment. Clearly, the degree of temporal matching is limited by the accuracy of the delay stage, in this instance be achieved within ±66 fs. This is easily

improved by the use of more precise equipment. And while improving the arrangement by use of different lenses and/or gratings, equation 8.4 can be used to determine an absolute limit to the precision of the technique by rearranging the equation to give

$$\Delta\tau = \frac{N\lambda_L^2}{c\Delta\lambda} \tag{8.5}$$

In this particular system, this was found to be ±33 fs i.e., the time difference between the two pulses that will add another fringe to the pattern. For a broader bandwidth, this of course will improve.

In the case where the temporal matching process is carried out with a misalignment of the focal spots of 250 μm, the 7 images begin from the top left at a time delay of $-1733(\sim -12T_0)$, $-1067(\sim -7.5T_0)$, $-400(\sim -3T_0)$ fs before temporal matching is reached. The process then proceeds to times of $+267(\sim 2T_0)$, $+933(\sim 6.5T_0)$ and $+1600(\sim 11.5T_0)$ fs. It can be seen that the fringes no longer simply vertical in orientation. This is due to a spatial difference being present on the vertical axis. The fringes do begin compressed and expand as the temporal overlap is approached, this time however, they also rotate. As shown in figure 8.9, the fringes rotate as they move beyond temporal overlap. This

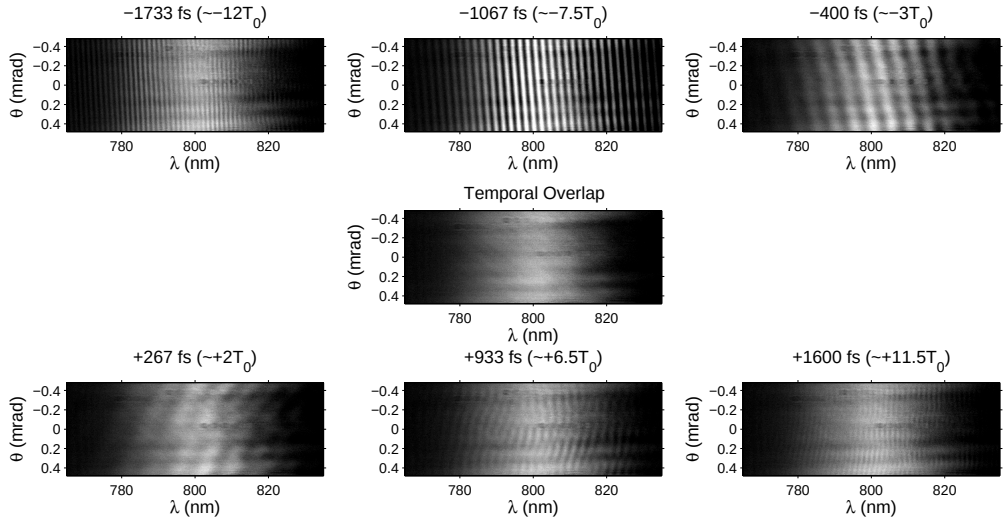

Fig. 8.9: Results of the temporal matching process as seen on the CCD camera when a misalignment of the focal spots at 250 μm is introduced.

rotation can be attributed to the spatial mis-match and is therefore, dependant on the arrangement of the setup, particularly the distances to and size of CCD chip as well as power and distance of the lens.

8.4 Temporal Overlap of Spatially Separated Foci

8.4.1 Experimental Setup for Spatially Separated Pulses

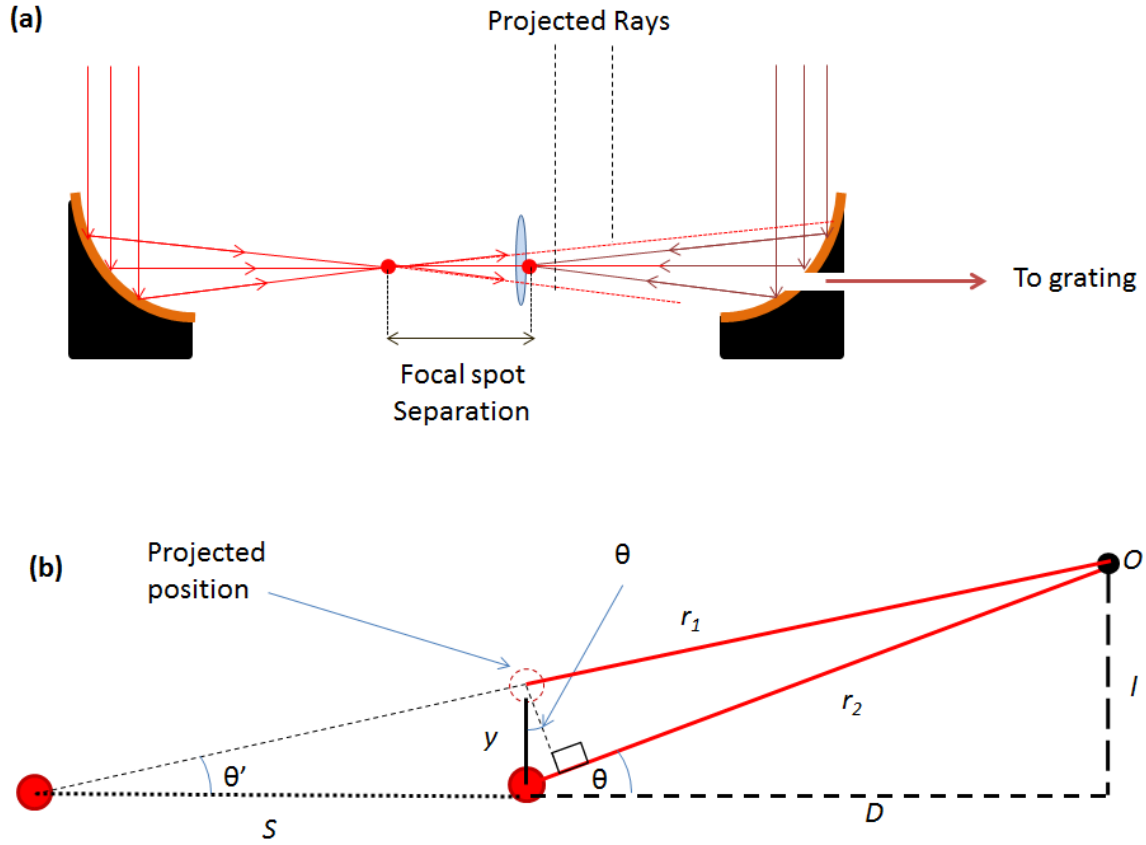

Fig. 8.10: The modifications made to the arrangement presented in figure 8.4. (a) Here the focal spots are separated in space by a distance S, (b) this new arrangement means that at the pellicle the displaced spot projects onto the pellicle causing a relative variation of the displacement.

As many experiments would require the foci of multiple pulses to be at different locations, the setup was modified to investigate the behaviour of the fringe pattern when the pulses are focused to a distance of 2.5 cm. The arrangement is given in figure 8.10.

The theoretical grounding is of course, unchanged from that presented in Section 8.1; however, as the focal spots are separated in space by a distance S the values for y and *theta* are co-dependant. With the pellicle marking the point at which temporal overlap is to occur, the focal spot of the pulse behind the pellicle is projected onto the pellicle and on towards the observer at O as shown in figure 8.10b. As can be seen, y now varies as $S\tan\theta'$, and because $D \ll S$, one can state that $\theta' \to \theta$. With $\theta \ll 1$ $\tan\theta \approx \sin\theta \approx \theta$ and hence, $\varphi = kS\theta^2$. As the setup remains unaltered after the parabola, the temporal fringes remain unaffected.

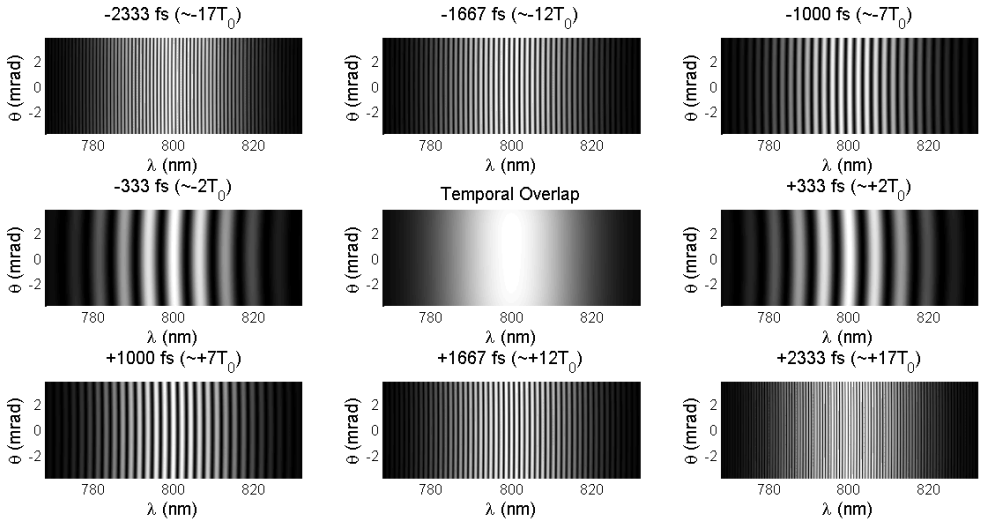

Fig. 8.11: Prediction of fringe patterns for spatially separated foci.

Figure 8.11 shows the expectations for 2.5 pulses that have been separated in space by a distance of 2.5 cm. As can be seen, the behaviour of the temporal fringes remains the same as those previously obtained. As the spatial relationship exhibits a θ^2 dependence, the fringes away from temporal overlap are slightly curved in appearance.

From the data presented here, one can see that the technique will work for determining the relative timing for any beam separation provided one can steer enough light to the CCD. The setups presented in this Chapter are for counter propagating pulses however, there is no reason that it would not be applicable to any geometry. In fact, what has been demonstrated here, is that the use of the cylindrical lens essentially removes the interference effects that are gained from the setup leaving the experimenter with the temporal fringes which are the sole requirement for measuring the degree of synchronisation.

8.4.2 Results for Spatially Overlapped Pulses

Figure 8.12 once again bears a remarkable resemblance to the predictions made in figure 8.11. As the pulses are separated by 2.5 cm along a common axis, the spatial variation is dependant on θ^2 and hence the fringes appear curved. The 9 images begin from the top left at a time delay of $-2333(\sim -17T_0)$, $-1667(\sim -12T_0)$, $-1000(\sim -7T_0)$, $-333(\sim -2T_0)$ fs before temporal overlap is reached. The process then proceeds to times of $+233(\sim 2T_0)$, $+1000(\sim 7T_0)$, $-1667(\sim -12T_0)$ and $+2333(\sim 17T_0)$ fs. It can be seen that the fringes do exhibit a curved nature. The behaviour of the temporal fringes is unaltered. A comparison of the number of temporal fringes was made.

As can be seen in figure 8.13, there is a strong correlation between what has been

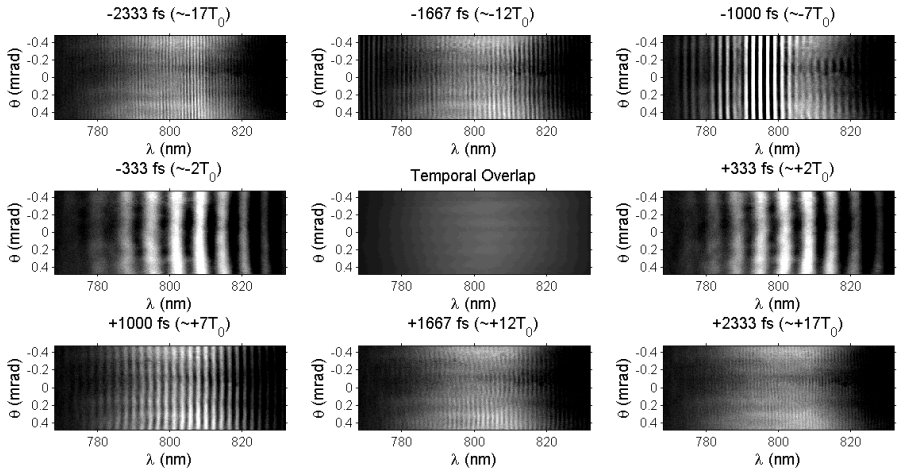

Fig. 8.12: Results of the temporal matching process as seen on the CCD camera for pulses spatially separated by 2.5 cm.

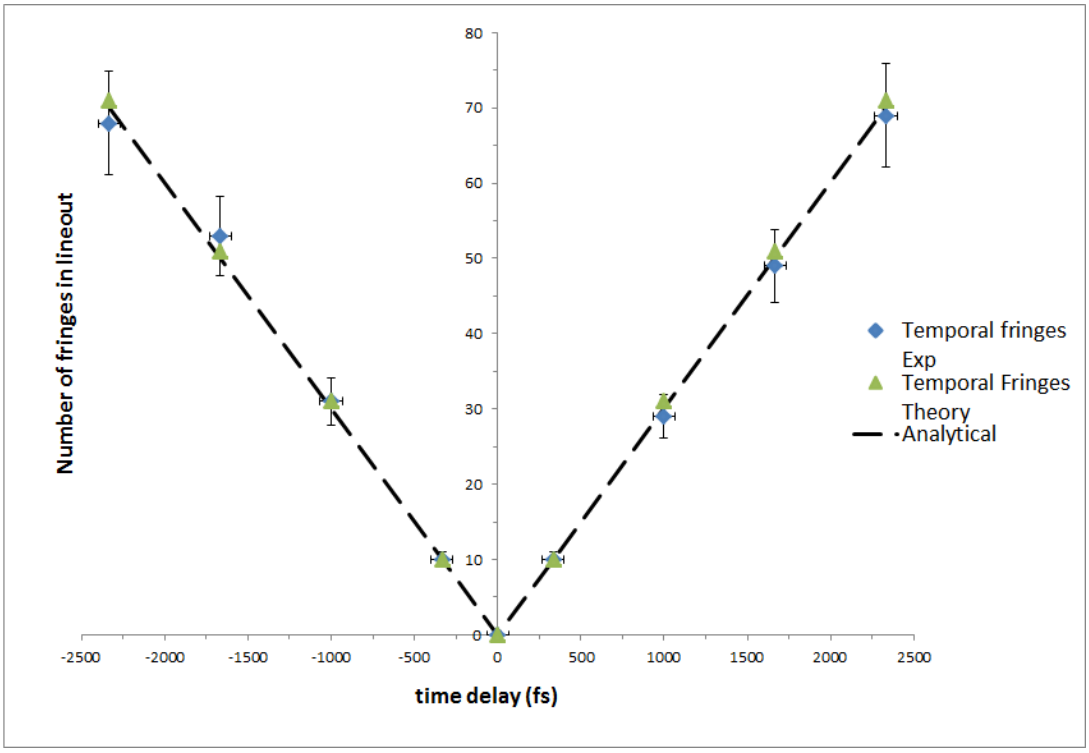

Fig. 8.13: A comparison between the theoretical expectations of the number of temporal fringes predicted (green) in the model presented in Fig. (8.5) and the number of fringes detected in the experimental setup (blue) for spatially separated foci.

predicted and obtained experimentally. This demonstrates the techniques versatility as a means of determining the degree of temporal overlap between two pulses.

8.5 Conclusions on the Spectral Interferometer

A method for real-time optical measurement of the temporal delay between two focussed and ultra-short laser pulses has been developed and presented. By varying the number of fringes on the CCD, one is able to determine with the delay between two intense laser pulses. In this case, this has been achieved with an uncertainty of ±66 fs i.e., the precision of the delay stage used. It has been shown that the degree of temporal overlap achievable, limited by a number of factors such as the step size available on the delay stage used, the resolution of fringes on the CCD and the number of lines per mm on the diffraction grating. However, assuming the impact of these factors can be minimised, a theoretical limit to the accuracy of the technique has been presented in equation 8.5.

Due to the compact and versatile nature of the technique, it should prove highly beneficial in reducing the technical difficulties that may arise specifically in the next class of multi-petawatt laser systems such as the 20 PW Vulcan at the RAL and the ELI, in which experiments with multiple ultra-high intensity lasers will be routinely performed. The technique has already been employed in a recent experimental campaign [43] carried out using the Astra Gemini laser at RAL [75] were the precision achievable was increased to ±15 fs demonstrating its viability as a beneficial technique in the modern laser laboratory. The results of this will be presented in Chapter 9.

Part III

EXPERIMENTAL FINDINGS

9. NON-LINEAR THOMSON SCATTERING EXPERIMENT IN A COUNTER-PROPAGATING BEAM GEOMETRY

In this chapter, the results from the experimental campaign in which NLTS was investigated using intense laser pulses in a counter propagating geometry is presented.

In this arrangement, an ultra-intense laser pulse was used to generate a beam of ultra-relativistic electrons through LWFA (see Section 2.2). This electron beam was collided with a second ultra-intense laser pulse. The resultant synchrotron emission (see Chapter 3) was detected using a lithium based detector (see Chapter 7).

9.1 Introduction and Motivation for Non-Linear Thomson Scattering Experiment in a Counter-Propagating Beam Geometry

In Chapter 2, the acceleration of electrons using an intense laser was discussed in detail. Using this accelerating mechanism, it will be demonstrated that high energy electron beams can be produced and forced to oscillate by a second intense laser pulse, leading to the emission of ultra-bright high energy gamma ray beams. This will be a demonstration of the first all optical wiggler system.

Previous investigations of laser-driven Thomson scattering have mostly focused on the linear or single-photon or undulator regime i.e., whenever the relativistically invariant dimensionless amplitude of the laser pulse ($a_0 < 1$) [27, 49] and report on γ-ray energies ranging from a few hundreds of keV [27] up to $3-4$ MeV [49].

In Section 3.2, the spectra emitted from an oscillating electron was determined. From this the radiated energy within a spectral bandwidth $d\omega$, centred on a frequency ω within a solid angle $d\Omega$ is given as

$$\frac{d^2I}{d\omega d\Omega} = \frac{e^2}{16\pi^3\epsilon_0 c} \times \left| \int_{-\infty}^{+\infty} e^{i\omega[t-\mathbf{n}\cdot\mathbf{r}(t)/c]} \frac{\mathbf{n}\times[(\mathbf{n}-\boldsymbol{\beta})\times\dot{\boldsymbol{\beta}}]}{(1-\boldsymbol{\beta}\cdot\mathbf{n})^2} dt \right|^2 \tag{9.1}$$

For a ideal bunch of electrons, this simply summation of each contributing electron. Three main factors can in principle be modified in order to increase the energy of the generated photons: the electron velocity β, the driving frequency of the laser ω_L and the intensity of the laser driving the interaction i.e., the a_0.

The energy of the generated photons can in fact be estimated as: $E_\gamma \approx 4\gamma_e^2 \hbar\omega_L f(a_0)$, whereby $4\gamma_e^2$ accounts for the relativistic Doppler shift and $f(a_0) \approx 1$ for $a_0 \ll 1$ or $f(a_0) \approx a_0$ for $a_0 \geq 1$ [35]. a_0 here relates to the number of photons with which the electron is interacting simultaneously, implying non-linear scattering for $a_0 > 1$. Perturbative non-linear corrections ($a_0 < 1$) were first reported in reference [110].

Liu and collaborators recently reported on an increase in photon energy (up to 8-9 MeV) by frequency converting the scattering laser up to its second harmonic (thus increasing $\hbar\omega_L$) [28]. However, using a higher laser frequency for scattering significantly reduces the laser energy available (crystal conversion efficiency into second harmonic of the order of 30-50 %), and the laser a_0 implying a modest number of generated photons ($\approx 3 \times 10^5$ photons per shot are theoretically inferred in Ref. [28]). This relatively low number can be easily understood if we consider that it would scale as $N_\gamma \propto a_0^2$ for $a_0 \ll 1$ [35]. The brilliance of this source is thus not higher than laser-driven bremsstrahlung source [5, 23, 24] (see figure 9.27 for a comparison of reported brilliance for different γ-ray sources). Only one work has reported on non-linear laser-driven scattering ($a_0 \approx 1.5$) using a single laser to both drive and scatter the electrons [29]. γ-ray energies of the order of few hundreds of keV were generated but the intrinsic difficulty in scaling this system to higher energies prevents it to be used for the generation of multi-MeV γ-ray beams.

In this Chapter, the generation of multi-MeV (maximum energy of the order of $16-18$ MeV) and ultra-high brightness ($> 10^7$ photons per shot with energy exceeding 6 MeV, implying a brightness exceeding $\sim 10^{20}$ photons s^{-1} mm^{-2} mrad $^{-2}$ 0.1% BW at 15 MeV) γ-ray beams following NLTS of an ultra-relativistic LWFA electron beam ($\gamma_{e^-} \approx 1100$) in the field of an ultra-intense laser pulse ($a_0 \approx 2$, $\hbar\omega_L \approx 1.5$ eV). The γ-ray spectrometry technique presented in Chapter 7 allowed for the first absolutely calibrated detection of the full spectrum of the γ-rays, clearly indicating onset of non-linear effects. This is the γ-ray source with the highest peak brilliance in the multi-MeV energy range ever generated in a laboratory.

9.2 Experimental Setup for Investigating Non-Linear Thomson Scattering Experiment in a Counter-Propagating Beam Geometry

In order to achieve the generation and subsequent detection of high-energy, high-flux γ-ray beams, a dual pulse, ultra-intense laser system is required. The Asta-Gemini laser, hosted by the Rutherford Appleton laboratory [75], provides a unique platform with which to conduct such an experiment. This laser delivers two laser beams each with central wavelength $\lambda_L \approx 800$ nm, pulse duration $\tau_L \approx (42 \pm 4)$ fs, and energy after compression of 18 J. Both lasers are generated from the same oscillator, avoiding problems of jitter in

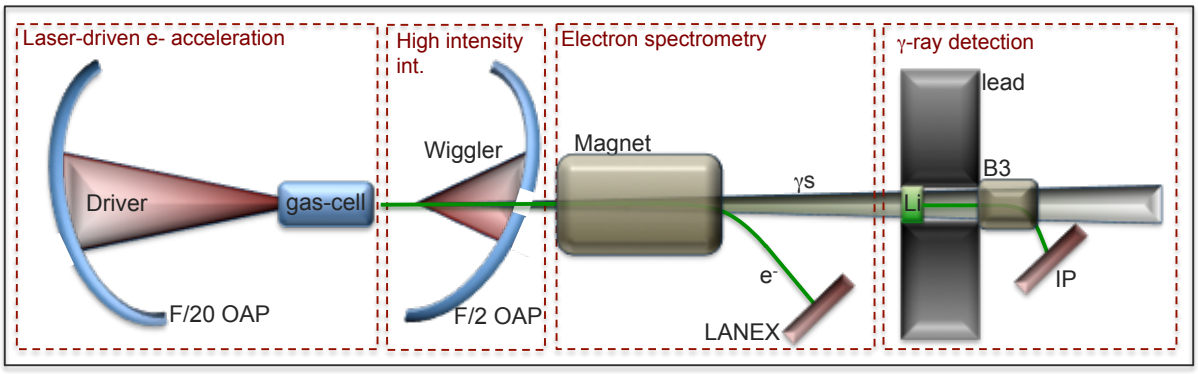

Fig. 9.1: Sketch of the experimental setup for all optical NLTS (picture Courtesy of G. Sarri).

their synchronisation.

The experiment consists of a laser pulse to generate a beam of high-energy electrons via LWFA hereby called the 'driver' and a second pulse to collide with the electrons and create the high energy γ-ray beam hereby known as the 'wiggler'. With Gemini able to produce up to 18 J on target in a duration of 42 fs, the intensity is increased by the use of parabolic focusing mirrors. The requirements for LWFA (outlined in Section 2.2) lead to the use of a long focus to ensure a stable wakefield is generated. Hence, an $F/20$ parabolic mirror assumes the role of the driver. For the wiggler the requirement is much more straightforward, to generate a large as intensity as possible. To strike the balance between generating a high intensity and practical considerations, an $F/2$ parabolic mirror is used.

As the interaction is maximised for a counter-propagating geometry (see Section 3.4), the experiment is setup in this manner; however, this will lead to a problem with the electron beam colliding and interacting with the wiggler mirror. The problems caused by this are twofold, firstly the electrons would generate high energy radiation via Bremsstrahlung that would potentially mask the signal generated by the NLTS interaction. Secondly, the energy of the electron beam would be distorted by this interaction and a meaningful electron energy spectrum would be unobtainable. The wiggler mirror thus, has a hole bored in the centre of it to allow the electrons propagate through the hole unobstructed. This hole accounts for an $F/15$ value and will reduce the intensity of the wiggler pulse but is necessary if a meaningful information is to be extracted. The hole also reduces the risk of back reflections into the laser amplifier chain which may lead to damage of critical components of the laser.

After the electrons exit the arrangement, they are spectrally resolved by a magnetic spectrometer (see Chapter 6) which consists of a 15 cm long 1 T magnet and a LANEX [79, 97] screen as the detection mechanism.

Finally, in order to determine the spectrm of the γ-rays produced, the lithium detector

is used (see Chapter 7). A brief overview of the experiment is given in figure 9.1. A more detail description of each of these sections will follow.

9.2.1 The Driver

In order to extract high-yield, high-energy electrons via LWFA, the driver consisted of an $F/20$ parabolic mirror, which takes the 15 cm diameter beam down to a focal spot of 27 ± 3 μm. As seen in Section **??**, the long focal length of the mirror is of course not optimal for achieving the highest intensities; however, as seen in Section 2.2 the long focus ensures that a long and stable cavity is created in which the electrons are accelerated. As the spot contains approximately 50% of the laser energy, the resulting intensity is determined to be $I_{\text{Driver}} \approx 3 \times 10^{19}$ W/cm^2.

The gas cell was a design by the collaborating group at Michigan and is presented in detail in references [81] and [111]. The cell is a single stage gas cell of 10 mm length and was filled with 97% helium which would create a stable wake and 3% nitrogen in order to increase the number of electrons injected into the wake.

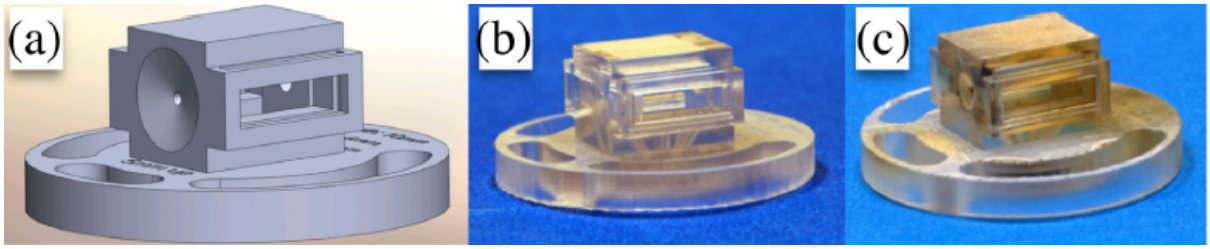

Fig. 9.2: The gas cell type used during the NLTS experiment [81]. (a) the CAD drawing of the cell. One can see the gap at the side through which optical interferometry can be carried out. (b) the 3-D printed cell before the experiment (c) the cell after use.

A small portion of the laser pulse was picked off using a small mirror before being expanded and used to probe the gas cell. Using this technique, one could optimise the backing pressure going into the gas cell and use that to determine the electron density of the plasma created and allowing one to infer the behaviour of the wake and the electrons produced [112]. Figure 9.3 shows the relationship between the backing pressure and the electron density.

As can be seen from figure 9.3, the relationship is linear as one would expect for below critical density and the intensities sufficiently large as to not deplete the pulse significantly. After this calibration, an optimisation process must be run in order to determine what pressure reliably produces high energy, high charge electron bunches.

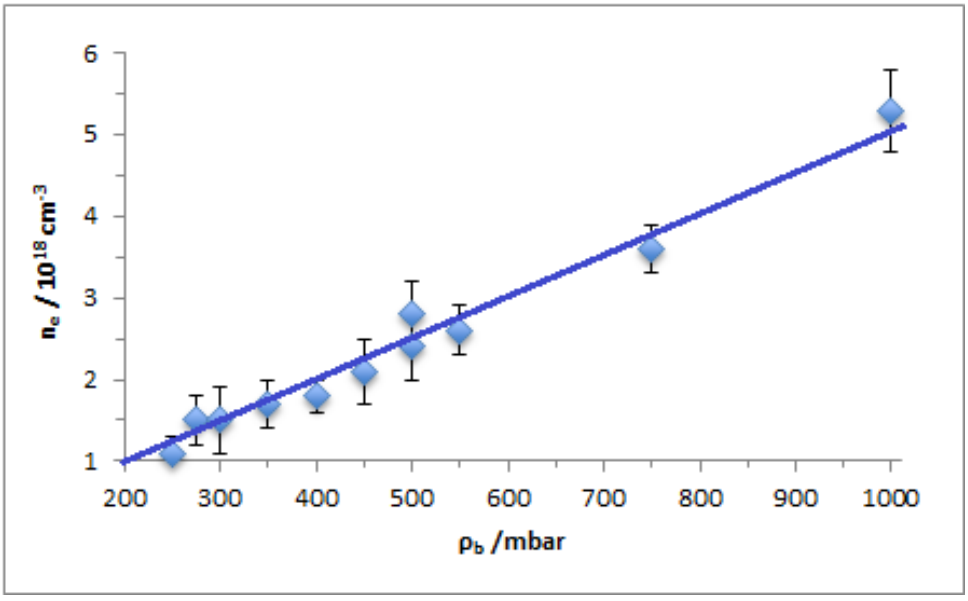

Fig. 9.3: The variation of electron density with the gas density. The blue line represents a guide for the eye.

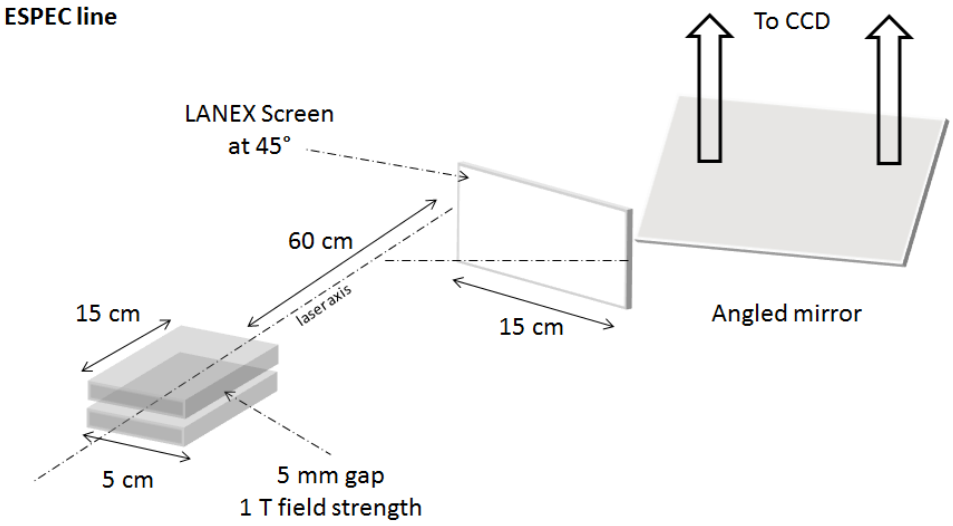

Fig. 9.4: The Electron spectrometer arrangement for the NLTS experiment consists of a strong (1 T and 5 mm gap) magnet of dimensions 15 cm long and 5 cm wide. A LANEX is placed touching the beam axis at one end and 15 cm long at a 45^o angle. A mirror allows the back of the LANEX to be imaged safely by a CCD camera.

9.2.2 Calibration of the electron spectrometer

Figure 9.4 shows the design of the electron spectrometer (ESPEC) used in the experiment. As the energies generated are expected to be in the order of 100's of MeV, a 15 cm long, 5 cm wide magnet of 1 T field strength is employed. A gap size of 5 mm ensures uniformity of the fields. A 15 cm long LANEX screen [79] is placed 60 cm from the screen at a 45^o

angle. A mirror allows the back of the LANEX to be imaged by a Andor iXon CCD camera [113]. This arrangement can be calibrated by using an imaging plate which is placed across the LANEX. As the number of electrons can be extracted easily from the imaging plate, a comparison between the signal levels on the CCD and the relative number of electrons on the imaging plate can be made and necessary adjustments applied to the values obtained on the CCD to allow them to accurately reflect the number of electrons which interacted with the screen. A comparison of the two calibration images is shown in figure 9.5.

Fig. 9.5: A comparison of the images obtained of the number of electrons on the imaging plate (top) and the Andor iXon CCD (bottom).

It has been shown in Section 6.2 that the number of electrons which interacted with an imaging plate can be given by equation 6.8: PSL = $\left(\frac{R}{100}\right)^2\left(\frac{4000}{S}\right)10^{L[G/(2^B-1)-1/2]}$. The numbers observed on the CCD were adjusted as to match the number of electrons extracted at the corresponding locations on the imaging plate. Using 'ImageJ' [93], the Gray value was obtained for the imaging plate. This allowed for the extraction of number of electrons at each position along the plate. Plotting this against the count values that were extracted for each location along the plate from the CCD, the necessary adjustments were made to allow the counts-electron value be determined. The match for the IP and the LANEX are shown in figure 9.6.

As can be seen from figure 9.6, the fitting applied to the ESPEC from the LANEX and the IP are closely matched. Hence, necessary adjustments can be made so that electron spectra can be obtained directly from the CCD images.

From Section 6.2, one can see that the calibration of a magnetic spectrometer is dependent on several factors primarily the magnets length L_m, its field strength B and the distance from the magnet to (in this case) the LANEX. First of all, a zero point must be established by generating electrons in gas cell and allowing them to travel through the

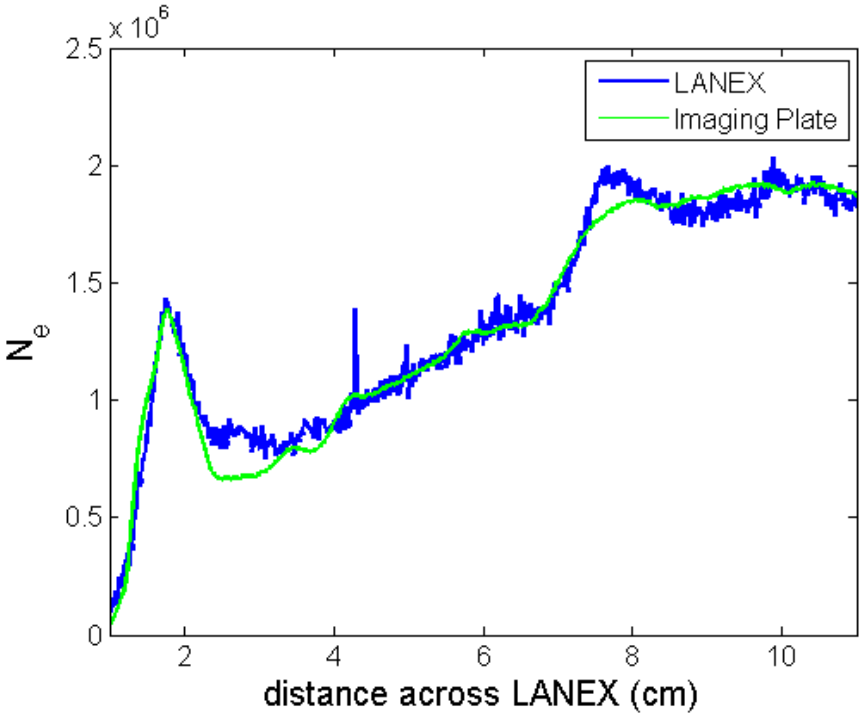

Fig. 9.6: A comparison of the images obtained of the number of electrons on the imaging plate (top) and the Andor iXon CCD (bottom).

setup without the magnetic field present. From taking lineouts from the CCD images one will be able to determine the direction electron beam travel if undeviated, this in turn, allows one to mark on the CCD the zero point. In addition using this arrangement, the pointing instability can be determined by looking at the degree of variation in the position of individual shots. Some select shots are shown in figure 9.7.

Looking at figure 9.7, it can be seen that the shapes are loosely Gaussian in shape. The FWHM is determined to be ~ 0.4 cm in size. With the source at a distance of 95 cm away, this corresponds to a half angle divergence of ~ 4 mrad. Shots also vary in their central position from around 0.2-0.3 cm corresponding to a pointing fluctuation of 0.1 cm. This factor must be considered when looking at the beam divergence and determining the resolution of the detector giving $\theta_S \simeq 5$ mrad. In order to determine the zero point, an average of the shot series was used (presented in figure 9.8).

Figure 9.8 shows the average pointing of the electron beam. Here the shape is loosely Gaussian and the centre of the beam is taken as 0.25 cm with FWHM of 0.5 cm. From this point, the energy of the spectrometer's axis can be calibrated.

Figure 9.9 shows the calibration of the ESPEC energy axis. As can be seen, the resolution of the detector is ideal for energies between 200-1400 MeV where the uncertiantity remains below 10%. It must be noted that the response is not linear. This means that the energy 'bins' as observed on the CCD are not linear each pixel of 25 μm in length will

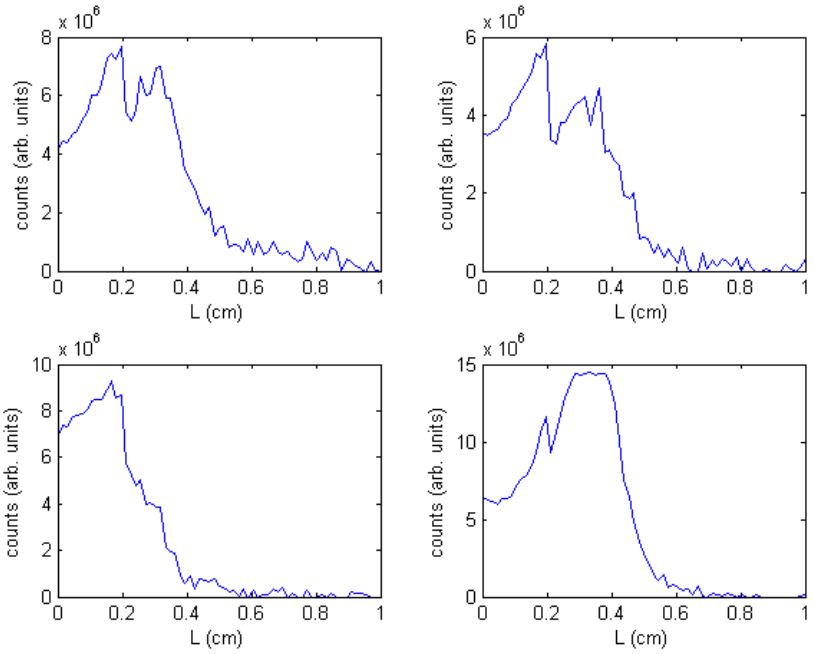

Fig. 9.7: A series of lineouts taken in the setup with the magnet driven out of the arrangement. The x axis represents the distance across the LANEX and the y axis represents the counts obtained on the CCD in arbitrary units.

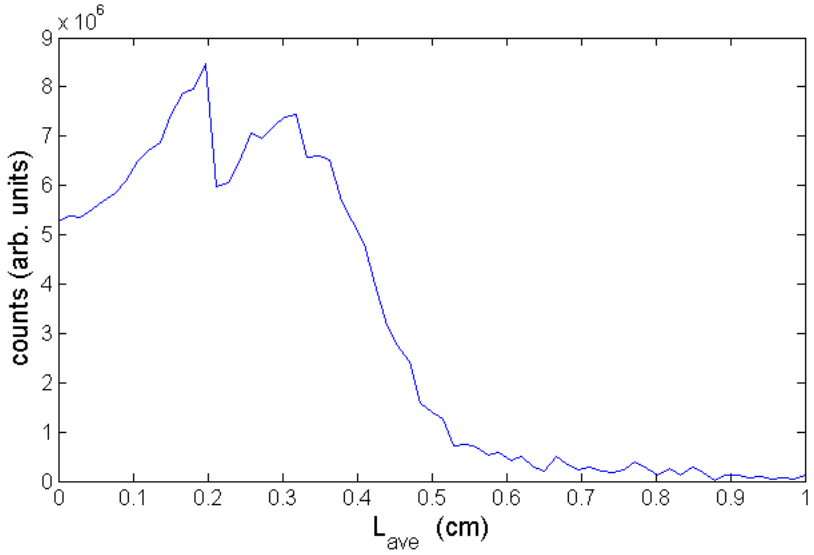

Fig. 9.8: The average lineouts taken in the setup with the magnet driven out of the arrangement. The peak centres on 0.25 cm from the edge of the Lanex screen and will represent the zero point of the spectrometer.

observe a different energy width and this must be considered when extracting a spectra.

With a calibrated ESPEC, the backing pressure was optomised to give the best balance of charge, energy and reliability. In a scan which will be presented elsewhere (see reference [111]), a backing pressure of 400 mbar was found to be ideal. From figure 9.3 this pressure

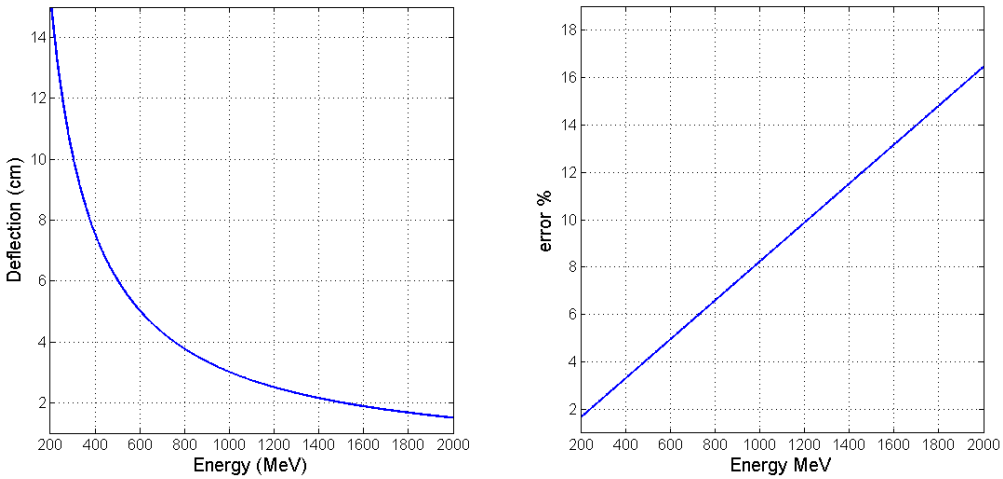

Fig. 9.9: The calibration of the electron spectrometers energy from the zero point and the subsequent error that arises from it.

corresponds to an electron background density of $(3.2\pm0.2)\times10^{18}$ cm^{-3}. This is analogous to a plasma period in the order of $\tau_{\mathrm{pl}} \approx (60 \pm 2)$ fs.

9.2.3 The wiggler and Temporal Overlap of the Pulses

The wiggler consists of an $F/2$ parabolic mirror with a hole of 2 cm diameter (Corresponding to an $F/15$ hole) to allow electrons generated to travel along the beam axis and be resolved by the ESPEC without distorting the spectra. The fast focus of this mirror allows a good compromise to be maintained between a small spot size and usability for the experimenters.

In order to increase the probability of an interaction occurring, a random phase diffuser was introduced into the beam which would lower the energy contained in the main peak and diffuse it into a larger secondary halo. This would increase the chances of an interaction in the case where the pointing fluctuations of the beams becomes large.

Spatial overlap between the two laser pulses was achieved with 5 μm precision using an alignment wire. This technique involves focusing one pulse to a small wire and focusing the laser onto it. The wire is then moved along the beam axis and the second laser pulse is also aligned to it. Initially the driver was aligned and the position marked so to indicate the location of the gas cell, then at the $F/2$ wiggler pulse.

As the electrons will travel with a velocity of $\beta \sim 1$, the relative timing could be measured by assuming the laser pulse from the driver and the electrons would arrive at or close the same time. Thus, temporal overlap was obtained using a spectral interferometry technique outlined in Section 8 and in reference [114]. The a thin pellicle was moved the position of the $F = 2$ focus to mark the position of the temporal overlap and the technique

was implemented.

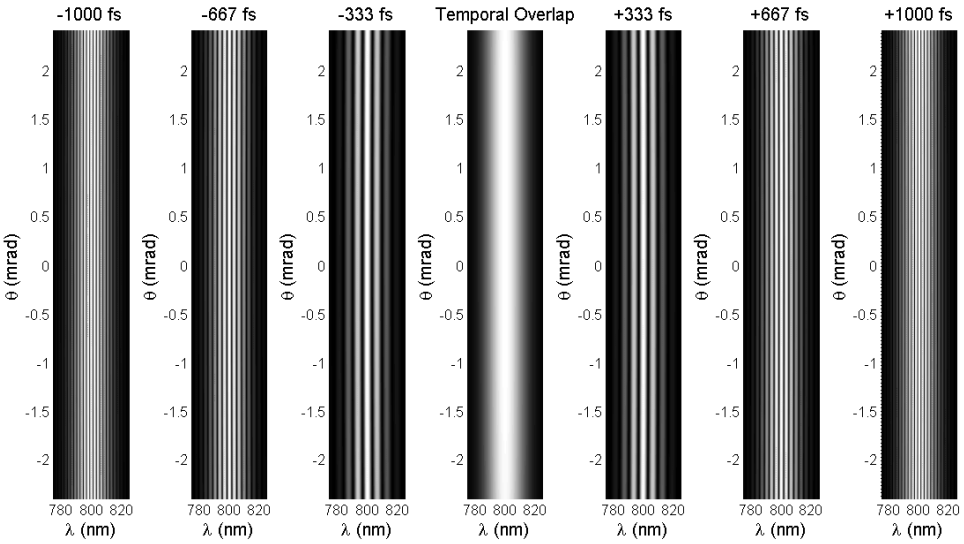

Fig. 9.10: The fringes that are predicted to arise using the same methods that were outlined in Section 8.

As can be seen in figure 9.10, the behaviour linked with the fringes is largely similar to that presented in Chapter 8 in that the temporal fringes increase in number when one moves away from temporal overlap. Due to the relatively large paths of the lasers at the Astra-Gemini facility (in the order of several meters), rough timing was carried out by using a fast photo-diode and a cathode ray oscilloscope in order to temporally match the pulses to within 9 ns. This ensured a quicker overlapping process. When this was achieved the spectral interferometer was implemented. The results of the process are given in figure 9.11.

As seen in figure 9.11 the number of fringes decrease when their temporal overlap approaches 0. When the numbers are compared to those predicted by the analytical model as in figure 9.12, one can see there is excellent agreement between the fringes generated and those predicted by the spectral interferometry technique. As the delay stage can go down to 10 nm, the delay stage is no longer the major limiting factor in determining the degree of synchronisation achievable. Looking back at equation 8.5, one can determine suitable values of $\Delta\lambda$ (50 nm) and λ_L (800 nm) to show the precision achievable is $\approx$ 21 fs.

With the pulses spatially overlapped to within 5 μm and temporally overlapped to 21 fs, the setup is able to be used to generate high energy gamma-ray beams through all optical non-linear Thomson Scattering.

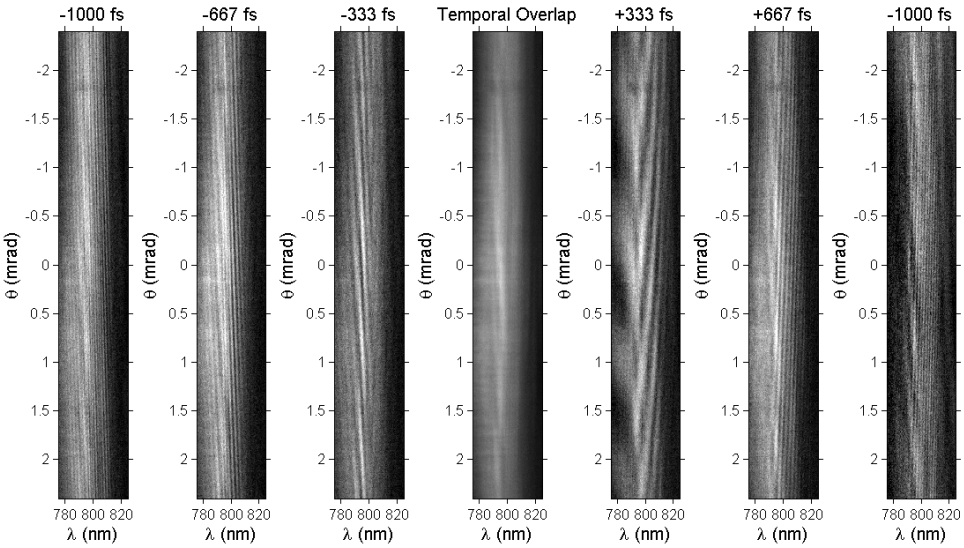

Fig. 9.11: The fringes which arise from the implementation of the spectral interferometer.

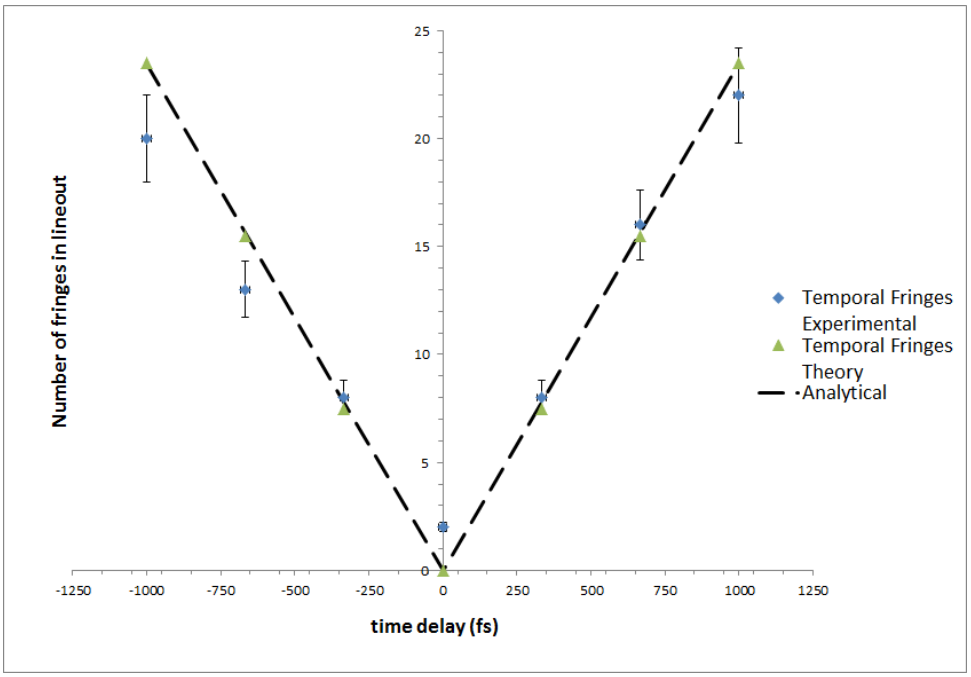

Fig. 9.12: Comparison of the number of fringes predicted (green) and the number obtained (blue) on the Astra-Gemini laser. The results are very similar demonstrate that timing can be overlapped to ~ 21 fs.

9.2.4 The Gamma Detector

Based largely on the designs presented in Chapter 7, the γ-ray detection was carried out by a lithium based detector. With the expectation that electron beams would be produced whose energies could be up to 1 GeV, adequate shielding was developed that could not only stop such electrons, but would reduce the level of noise created via Bremsstrahlung

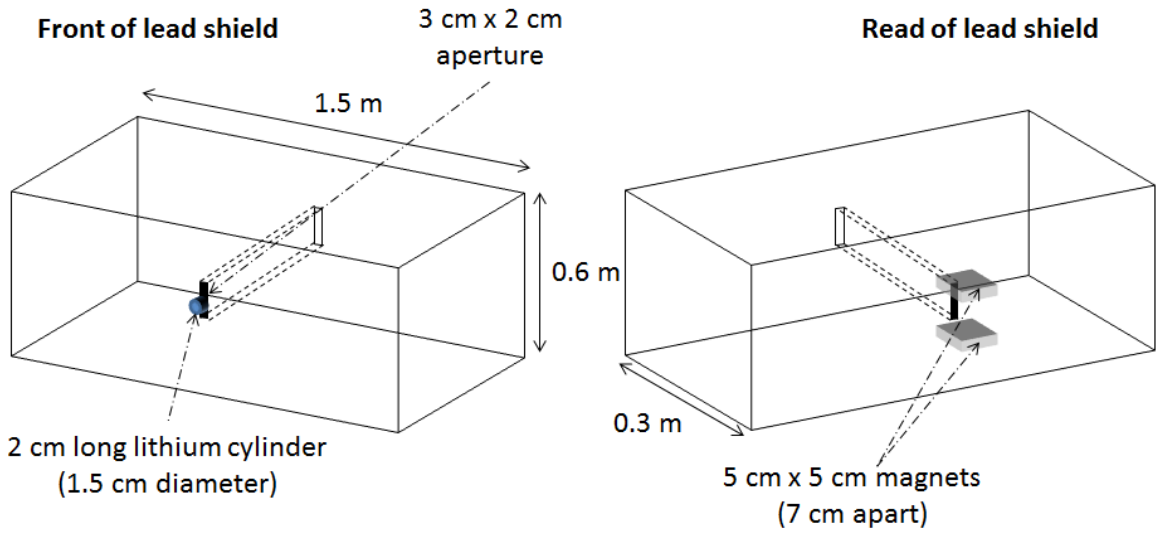

Fig. 9.13: The shielding used for the lithium detector based on the design presented in Chapter 7.

to negligible. From simulations carried out using FLUKA [99, 100], a shield of thickness 30 cm was found to match these requirements (presented in MSc dissertation by D.J. Corvan, 2013). In order to cover the electrons swept away by the ESPEC as well as any other potential sources of noise generated in the chamber, the face of the shielding was designed to be 1.5 m wide and 0.6 m high.

As shown in Chapter 7, lithium of 2 cm thickness provides one with a yield that is large enough to detect with relative ease, while not compromising on the spectral response; hence, a cylindrical block of 1.5 cm diameter and thickness 2 cm was set along the beam axis. A aperture 3.0 cm height and 2 cm with was used to angularly select a large number of the electrons generated by the interaction. At the opposite end of the aperture, a yoked magnet 5 cm × 5 cm, with a gap of 7 cm and field strength 0.3 T was placed to spectrally resolve the electrons generated by the lithium. The basic design is presented in figure 9.13.

To detect the electrons, the detector would use imaging plates 15 cm long and 4 cm high. In order to facilitate the relatively high rep rate of the Gemini laser (one shot every 20 second) and accommodate the radiation procedures of the facility, it was decided that these would be placed on an array and the plates would be exposed to 10 shots and averaged to determine the spectrum of a particular set of parameters. The array consists of four imaging plates on a motorised stage [115]. In order to ensure the plates remained blank, this array would sit behind a second lead shield 4 mm thick that had a hole cut in it also of 15 cm long and 4 cm to ensure that only a single imaging plate be exposed at a time. The design of this is given in figure 9.14.

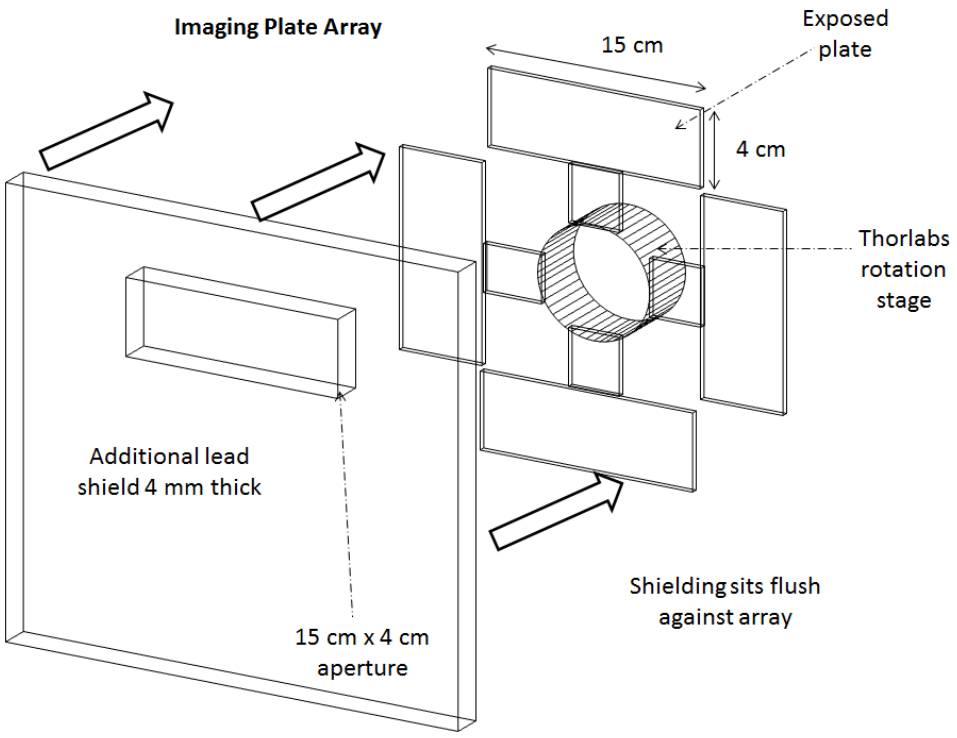

Fig. 9.14: The imaging plate array used to detect the electrons generated from the interaction of γ-rays with the lithium block.

As the development of the lithium detector is still in the early stages, it is useful to carry out simulations specific to the setup in order to determine the exact nature of the electron signal obtained on the image plates. Once again, FLUKA [99, 100] was employed to carry out this task. Using 10^8 iterations, a number of simulations were carried out allowing one to determine the spectral response of the setup for beam energies of 6, 8, 10, 12, 15, 17 and 20 MeV. Unlike the pencil beams employed in the initial design, the input beams chosen were given a diameter of 2.5 cm and a divergence of 2.5 mrad to match the possible beams predicted to be emitted from a combination of the electrons produced by LWFA and the wiggler driving those electrons with an intensity parameter $a_0 = 2$.

As can be seen from figure 9.15, the numbers and spectral profiles obtained are a slightly different from those shown in Chapter 7 in both shape and number; however, the spectra can be considered as consisting of two distinct parts, a Compton peak and a tail of low energy electrons. This time the tail is due not only to scattering within the lithium itself but as a result of gamma and secondary electron interaction with the lead shielding and the air in the chamber. A fitting equation was applied to the spectra to allow one to generate a deconvolution script that would be easily implemented.

The first step in developing a fitting equation was to match the Compton peak spectra obtained. The peak number of electrons generated A_C falls as the energy of the incoming

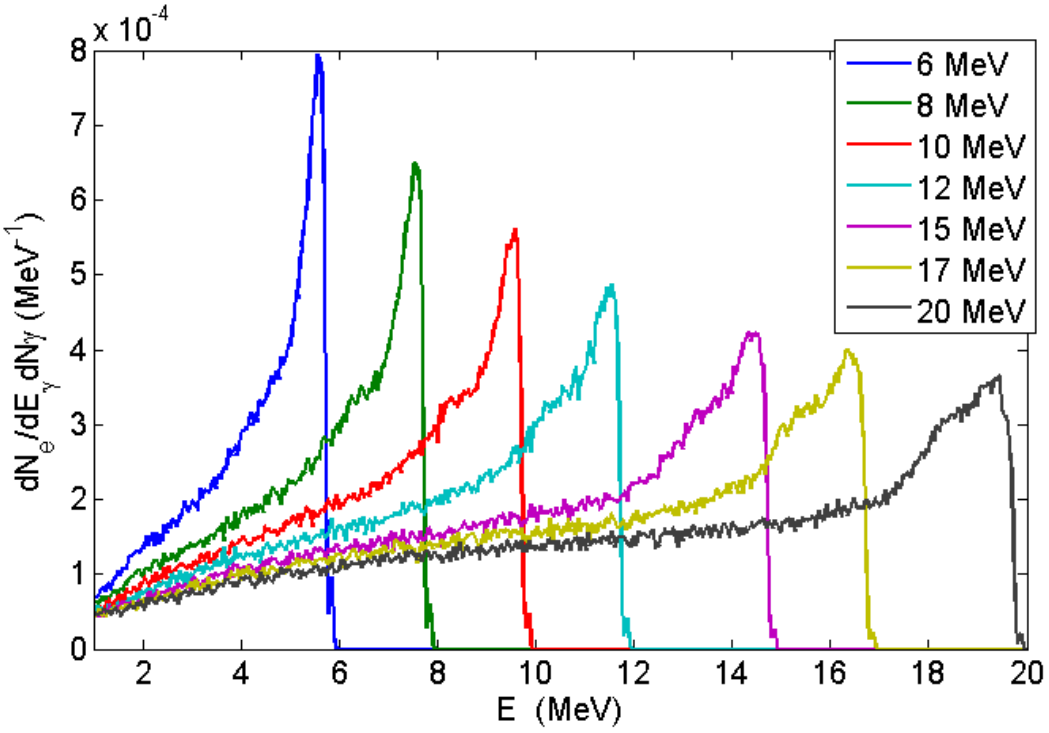

Fig. 9.15: The results of simulations carried out with FLUKA [99, 100]. Using 10^8 iterations, beam energies of 6, 8, 10, 12, 15, 17 and 20 MeV with diameter of 2.5 cm and a divergence of 2.5 mrad were used. The spectra produced are per number of input gamma per MeV.

γ photon E_γ increases. This decrease was determined to be exponential in nature and is given by

$$A_C = \frac{A_0}{(E_\gamma/40)^{0.75}} \exp -[0.001(E-5)]^2 \tag{9.2}$$

Where $A_0 = 0.165 \times 10^{-3}$ MeV$^-$1, and E is the energy of the electrons produced. The Compton aspect of the spectra is mainly described by the equation

$$C_M = A_C \exp -\left[13\left(\frac{E}{E_\gamma} - 0.98\right)\right]^2 \tag{9.3}$$

The equation 9.3 is not complete as the highest possible energies are unlikely to arrive at the detector as they propagate through both the lithium and the air. In order to compensate for this, the equation is corrected to give

$$C_e = C_M\left(1 - \exp -\left[0.8\left(E - E_\gamma - 0.9\right)\right]^{20}\right) \tag{9.4}$$

The super Gaussian (exp to the power of 20) in equation 9.4 essentially shuts off the high energy end of equation 9.3 which more accurately portrays the behaviour of the Compton electrons. This is not however, a full description of the spectra. In order to

describe the electrons that will be detected having been scattered or generated through other interactions such as pair production in the lithium or interaction with the shield i.e., the dark current, a second part the equation is added. This is a quadratic equation that is applicable only over the range R_1, where $R_1 = \exp -(E/(0.98E_\gamma))^{20}$.

$$D_e = A_D\left(\left(\frac{E}{E_\gamma^{1.5}}\right)^2 + \frac{E}{E_\gamma} + c\right)R_1 \tag{9.5}$$

Where $A_D = 5.5 \times 10^{-3}$ MeV$^-$1, $a = 0.7$ MeV$^-$1, $b = 8 \times 10^{-3}$ MeV$^-$1 and $c = 12.5 \times 10^{-3}$ MeV$^-$1. Equations 9.4 and 9.5 can be added together to form the fitting equation used to perform the deconvolution of the lithium spectra as shown in equation 9.6.

$$G_e = C_e + D_e \tag{9.6}$$

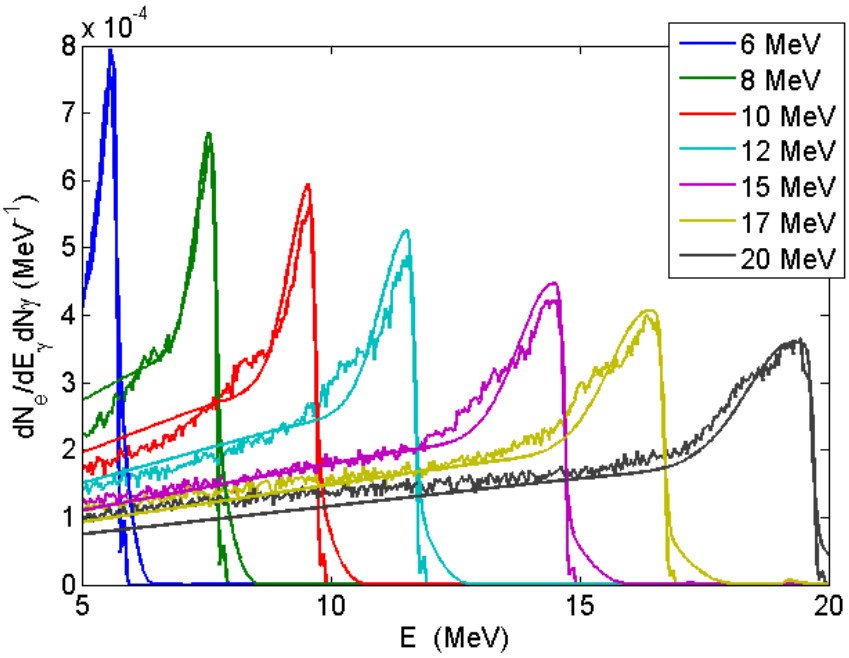

Fig. 9.16: The fitting equations applied to the data obtained from 9.15. The input values are given as 6, 8, 10, 12, 15, 17 and 20.

Figure 9.2.4 shows the fitting equations applied to the various input energies in the simulation for the energy range that should be detected $5-20$ MeV. As can be seen there is good agreement between the electron spectra obtained using FLUKA and the fitting equation 9.6. There are some visible problems with the fitting; firstly, there is a region of electron production beyond the initial input energy, secondly the values of D_e appear a little too high at lower energies and lower at higher energies. However, as the aperture of the detector is large (3×2), this will only make a small contribution to the overall

uncertainty. If the aperture were to be smaller, then further corrections may need to be applied.

9.3 Results of Non-Linear Thomson Scattering Experiment in a Counter-Propagating Beam Geometry

9.3.1 The Effects of Temporal Overlap

During the course of the experiment, several parameters were scanned in order to determine the effects on the spectra of γ-rays that would be obtained.

Initially, the relative timing of the two beams was varied. 10 shots were taken for temporally overlapped pulses before the timing was altered to +133 and −133 fs from perfect overlap. The results of this shot series are presented in figure 9.17.

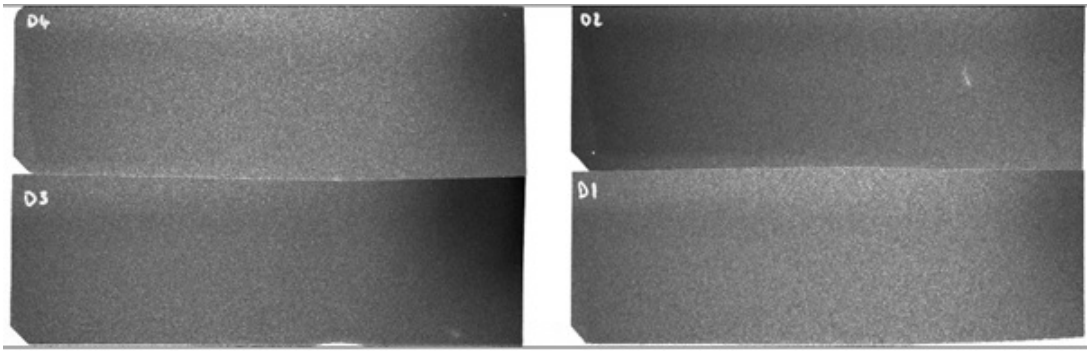

Fig. 9.17: The raw data scanned from the imaging plates used in shot series 64-113. Going anti-clockwise from the bottom right of the figure, the plate numbers are $D1$, $D2$, $D4$,an $D3$.

From the temporal scan results in figure 9.17, it can be seen that the imaging plates show various levels of exposure to high energy particles (represented by a darkening of the plate). The left side of the plate is closest to the beam axis and thus, represents the high energy end and energy decreases to as one moves right across the plate. $D1$ (bottom right) was the plate used when the beams were temporally separated by ~ 333 fs. Hence, this plate was used to take a background level for the run.

Plate $D3$ (bottom left) showed high activity at the low energy end of the plate and also represents the plate which has been exposed to the highest levels of high energy particles. This is within expectations as this plate used for a temporal overlap of 0 fs. Plate $D2$ (top right) was used for +133 fs, showed some activity at the high energy end of the plate but upon subtraction this seemed to be a spurious effect likely due to x-rays created by the electrons generated during the run of $D3$ and may indicate a design flaw that can be rectified in future iterations of this experiment. There is however, signal on the low energy end albeit, low levels compared with $D2$. Moving to $D4$ (top left), one

can see that there is activity low energy end of the plate which is comparable to that of plate $D2$. This again is within expectations as the timing was altered to -133 fs for this shot series.

As this is only raw data and a qualitative analysis can give little insight, equation 6.8 needs to be applied (as in previously shown in figure 9.5). The electron spectra that is extracted from this including subtraction of noise is given in figure 9.18

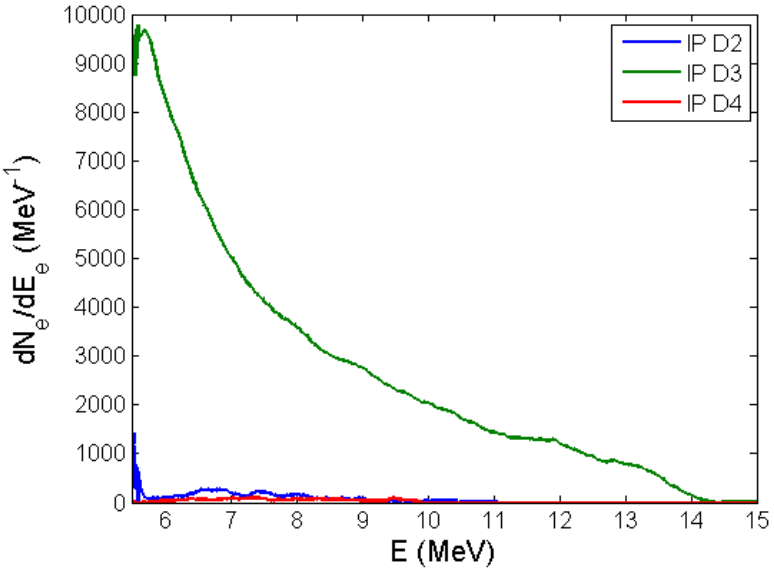

Fig. 9.18: The electron spectra from the run 64-113 after noise subtractions. The electrons are normalised to the number of shots.

Figure 9.18 shows the electron spectra that were obtained from the imaging plates presented in figure 9.17 including the subtractions of sources of noise. As can be seen, the imaging plates with a temporal mis-match, $D2$ and $D4$ show the presence of much fewer electrons above the background levels than that of $D3$ where temporal overlap was minimised. The energy of these electrons extends up to 10 MeV and down to 5.5 MeV i.e., the limit of the detector. Imaging plate $D3$, as expected, has the number of electrons. These electron decay from ~ 6 MeV to just above 14 MeV. There does seem to be a decay in the signal level below 6 MeV but due to limitations in the detector, more information could not be extracted from this setup.

With the electron spectra obtained, it is now possible to apply the deconvolution routine in order to extract the γ-ray spectrum that is implied from each imaging plate. The temporal shot variation run yielded interesting results presented in figure 9.19

Figure 9.19 shows the results from the deconvolution of the signal by the lithium detector for a variety of relative timing delays. The uncertainty of the results in energy is ≈ 1 MeV and this data-set represents an oversampling which requires averaging. The

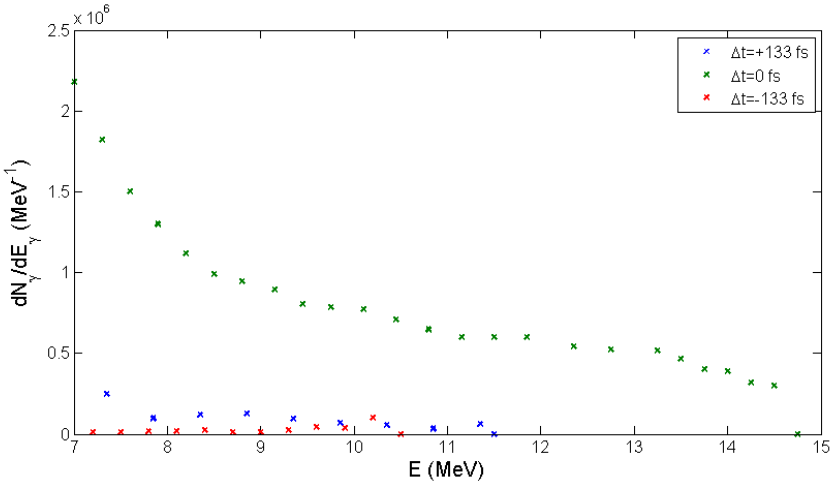

Fig. 9.19: The results from the deconvolution of the signal obtained by the lithium detector for a variety of relative timing delays. The green points represent the γ-ray spectrum for two temporally overlapped pulses.

green points represent the γ-ray spectrum for two temporally overlapped pulses. The γ-ray spectrum in this case shows energies exceeding 14.5 MeV and numbers up to 2.25×10^6 MeV^{-1}. The blue points represent a timing change of -133 fs and the red -133 fs. These spectra extend up to 11.5 MeV and 10.5 MeV respectively with numbers much lower than those shown in the temporal overlapped case with numbers below 0.5×10^6.

Clearly, it can be seen that NLTS is dependent on the relative timing between the two pulses. This is a clear demonstration that this arrangement can yield high energy γ-ray beams.

9.3.2 The effects of Spatial Overlap

In the second scan series, the spatial overlap of the two beams was varied. 10 shots were taken for temporally overlapped pulses before the timing was altered to +20 and -20 μm from perfect overlap. The results of this shot series are presented in figure 9.20.

From the spatial scan results in figure 9.20, it can be seen that the imaging plates show various levels of exposure to high energy particles. As with the previous run, the left side of the plate is closest to the beam axis and thus, represents the high energy end which decreases to as one moves right across the plate. $B4$ (top left) was unused as to take a background level for the run. However, this again showed some spurious signal level, likely due to cross talk between the plates (* this was also considered in the previous run).

Plate $B2$ (top right) showed the highest activity at the low energy end of the plate and additionally, there appears to be darkening of the plate at higher energies than in

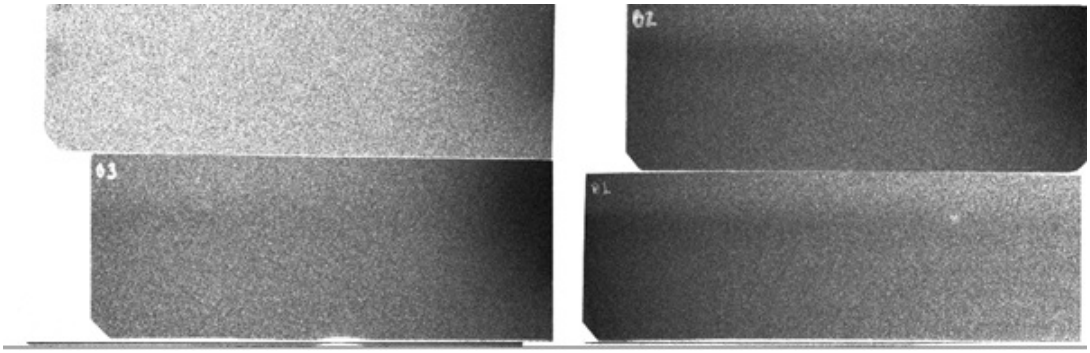

Fig. 9.20: The raw data scanned from the imaging plates used in shot series 173-212. Going anti-clockwise from the bottom right of the figure, the plate numbers are $B1$, $B2$, $B4$,an $B3$.

the previous run. This plate used for a spatial mis-alignment of 0 μm. Plate $B1$ (bottom right) was used for +20 μm, a similar level of activity at the high energy end which tails off. Plate $B3$ (bottom left) was used for -20 μm and shows some activity at the high energy end but higher levels of activity at the low energy end. Qualitatively, this run appears to be consistent with the expectation of spatial effects on NLTS but of course, quantitative values are required to be extracted using the calibration of the detector and the PSL equation. The electron spectra is shown in figure 9.21.

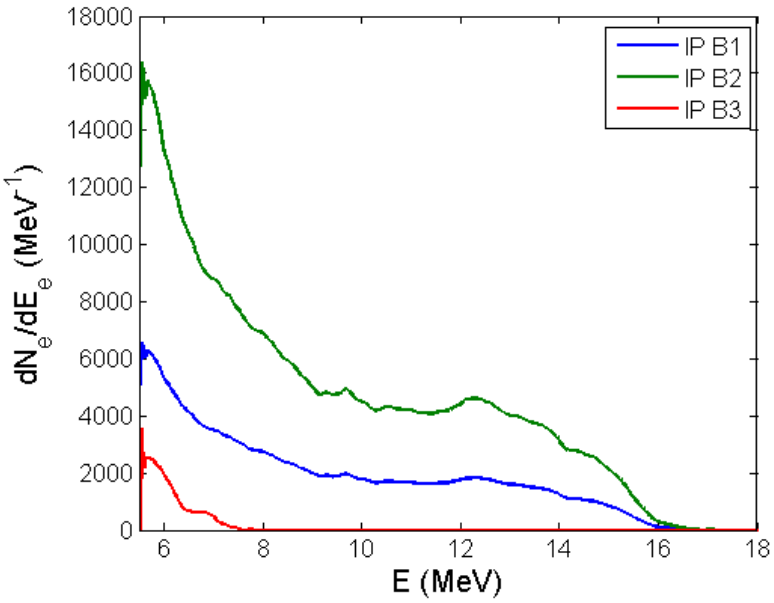

Fig. 9.21: The electron spectra from the run 173-212 after noise subtractions. The electrons are normalised to the number of shots.

From figure 9.21, one can see that the highest number of electrons are produced when the beams are perfectly overlapped. For plate $B2$ which represents a spatial overlap of 0 μm, the energies extend up to 16 MeV. Electron numbers and energy appear to be higher

than those presented in figure 9.18. For $B1$ whenever the beams are misaligned by +20 μm the peak energy seems to match that of the perfectly aligned pulses. However, the numbers are largely 3 times lower. For $B3$ whenever the beams are misaligned by +20 μm, the energy only extends to 8 MeV and numbers are again much lower than presented in the other two plates. This may indicate that the electrons are pointing in a slightly different direction to the beam axis.

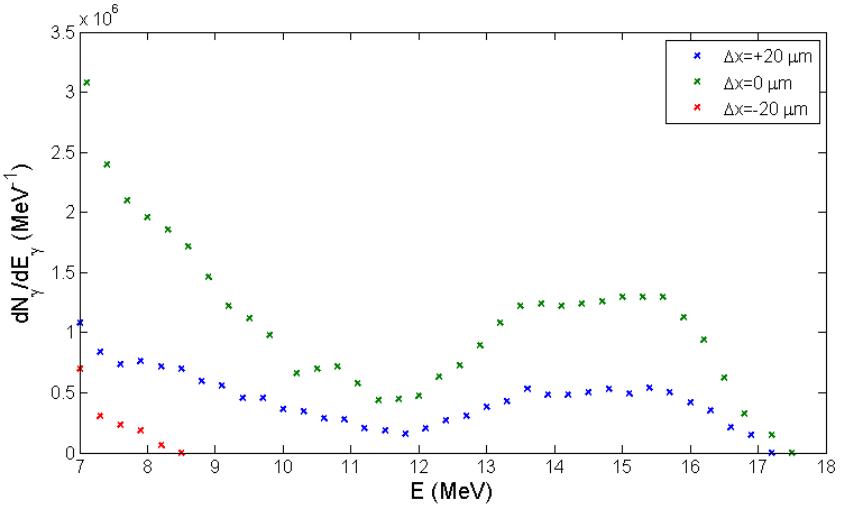

Fig. 9.22: The results from the deconvolution of the signal obtained by the lithium detector for a variety of relative timing delays. The γ-rays are normalised to the number of shots.

Clearly, it can be seen that NLTS is dependent on the relative overlap between the two pulses. However, one must take care to ensure that pulses are aligned in a manner that accommodates for the electron pointing.

9.3.3 Comparison with Theory

In order to make sense of the spectra obtained, one must look at the electrons which were used to generate the radiation. During the course of the runs, a number of additional detectors were placed in the chamber of the lithium detector, taking advantage of the low number of γ-rays absorbed by the lithium. These detectors (whose exact operation is beyond the scope of this thesis but can be found in reference [111]) included a scintillator and coincidence detector which would be used to determine if numbers of γ present had increased significantly in an individual shot. This allowed one to identify particular shots which yielded potentially interesting results.

Figure 9.23 shows the average electron spectra obtained from the two runs. Significant shots were identified using the scintillator and coincidence detectors, and the calibrated ESPEC used to determine the numbers present. The results from the temporal scan are presented in the graph on the left in blue and the spatial run is averaged from 4 important

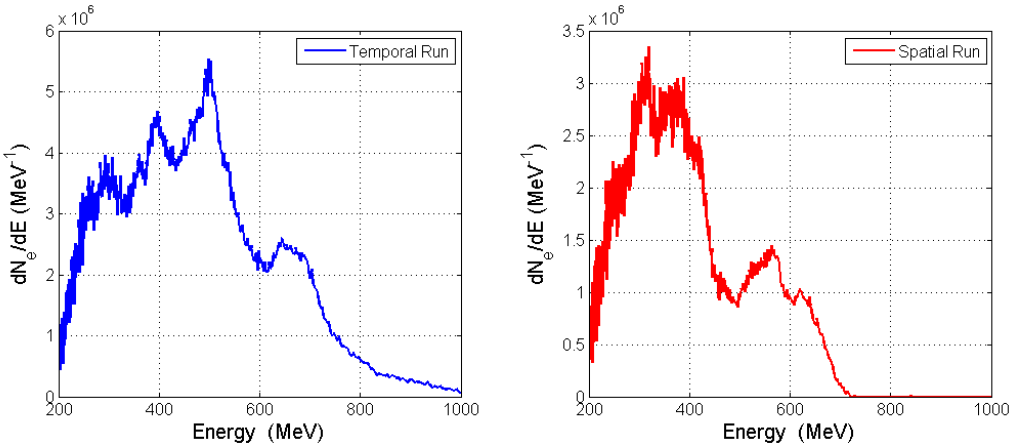

Fig. 9.23: The average electron spectra obtained from the two runs. Significant shots were identified and the calibrated ESPEC used to determine the numbers present. The peak numbers of electrons are 5.6×10^6 MeV^{-1} in the temporal scan and 3.2×10^6 MeV^{-1} in the spatial scan.

shots with a high energy peak of ≈ 650 MeV peaking at 2.5×10^6 MeV^{-1}. The spectrum has a low energy tail with peak numbers of 5.6×10^6 MeV^{-1} at ≈ 500 MeV which decays to 200 MeV.

The results from the spatial scan are presented in the graph on the right in red and the spatial run is averaged from 5 important shots with a high energy peak of $\approx$ 575 MeV peaking just below 1.5×10^6 MeV^{-1}. The spectrum has a low energy tail with peak numbers of 3.3×10^6 MeV^{-1} at ≈ 375 MeV which decays to 200 MeV. There is no significant reason as to the differences in numbers between the graphs presented.

In order to determine the validity of the spectrum after interaction i.e., whether or not quantum effects need to be considered, an estimate of the quantum non-linearity parameter χ_0 must be considered. This is given by the equation $\chi_0 = 5.9{\times}10^{-2} E_{e^-}[\text{GeV}]\sqrt{I_L[10^{20}\ \text{W/cm}^2]}$ and will be elaborated on in Chapter 10 (see equation 3.59) [26]. From the spectra presented in figure 9.23, a reasonable value for the energy would be $E_{e^-} \sim 550$ MeV and the laser intensity is given as $I_L \sim 8 \times 10^{18}$ Wcm^{-2}. Inputting these values for χ_0, one finds that $\chi_0 \simeq 0.01$ hence, quantum effects can be neglected.

Additionally, as shown in figures 9.19 and 9.22, the maximum energy emitted by these electrons is in the order of 17 MeV. This means that radiation-reaction effects (to be expanded on in Chapter 10) will also be negligibly small. As one can consider this as a recoil-less interaction, the electron spectrum after scattering by the intense laser is substantially unchanged and thus, the spectra found after the interaction remains a valid approximation for the initial electron spectrum.

To generate the theoretical emission spectra, the integration of the classical Lorentz equation in the presence of a laser field with a Gaussian temporal profile and initial electron spectrum based on those presented in figure 9.23. This gives the trajectories of

the electron upon interaction with the pulse, after which the Liénard-Wiechert equation can be applied and the subsequent gamma yields generated (simulations courtesy of Chris Harvey QUB).

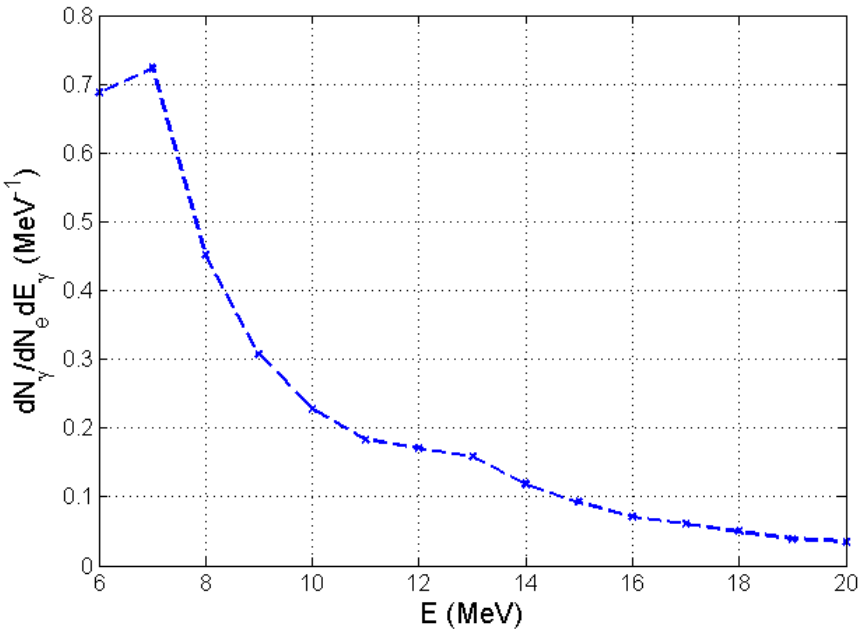

Fig. 9.24: The results of the numerical integration of the classical Lorentz equation for an electron spectra based on the results presented in figure 9.23, in the presence of a Gaussian pulse of intensity matching that of the wiggler. The y-axis shows the number of photons emitted per MeV and are presented normalised to the number of electrons interacting with the pulse (Courtesy of C. Harvey).

Figure 9.24 shows the results of the numerical integration. The y-axis shows the number of photons emitted per MeV and are presented normalised to the number of electrons interacting with the pulse. One can see that the peak number of photons are produced at 7 MeV with a number of 0.7 MeV^{-1} per electron. The spectra decays at higher energies.

With the number of γ-rays predicted, one can begin the process of matching the numbers predicted. One can predict an electron beam which has a size of the order of the driving pulse i.e, 27 ± 3 μm and a divergence of 4 mrad with pointing fluctuations for the electron beam to be in the order of 1 mrad, if the wiggler is positioned at the exit of the gas cell, then the electrons propagate a distance of 1 cm, the spot size at the wiggler is estimated to be ≈ 80 μm at the point of interaction with a wiggler spot size of 50 μm; however, with the wiggler fluctuations being in the order of 60% of the total spot size [75], this value can be thought of as having an effective spot size of 30 μm. This means that the effective ratio of sizes of the electron beam to the wiggler pulse are 0.14.

Now considering and the actual proportion of electrons with which the pulse interacts is decreased. Given that the wiggler pulse is of a duration of 42 fs but that the electron beam has duration estimated to be 60 fs, only ~ 3/4 of the electrons can expect to interact with the pulse. This gives an effective interaction factor of 0.09375.

Given also, that the active part of the detector, the lithium block has a diameter of 1.5 cm and that the cone angle is given by a_0/γ, where $\gamma \approx 1000$, one can imply a collection efficiency from the detector of 0.09. Hence, as there are electrons in the order of 4×10^8, the numbers of gammas detected can be determined and a comparison with theory made.

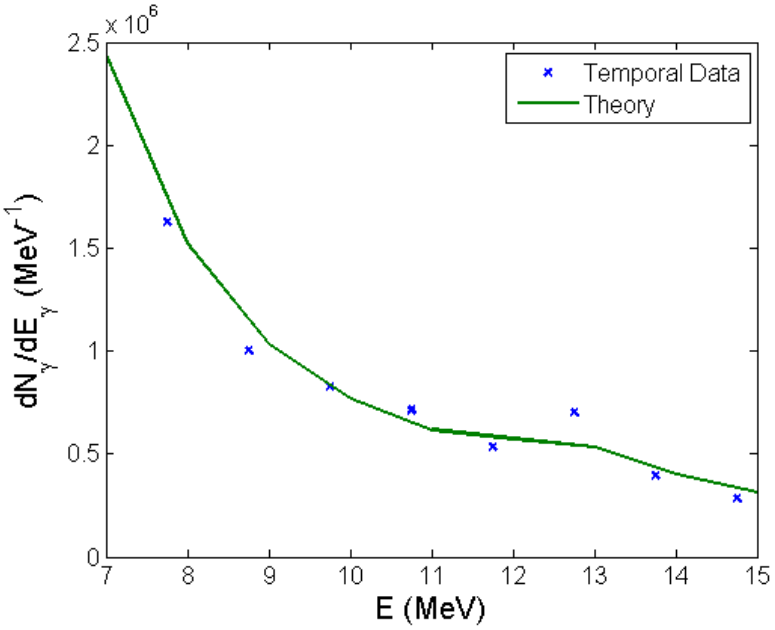

Fig. 9.25: Graph showing the comparison of the numbers of γ-rays detected at best temporal overlap (blue crosses) and the number predicted (green line). As can be seen, there is excellent agreement between the results obtained and the results predicted in the range 7-15 MeV.

Figure 9.25 shows the comparison of the numbers of γ-rays detected at best temporal overlap (blue crosses) and the number predicted (green line). As can be seen, there is excellent agreement between the results obtained and the results predicted in the range 7-15 MeV where the numbers of γ-rays detected fall within the acceptable tolerances of the lithium detector.

Figure 9.26 shows the comparison of the numbers of γ-rays detected at best temporal overlap (blue crosses) and the number predicted (green line). As can be seen, there is good agreement between the results obtained and the results predicted in the range 7-12 MeV; however, the increase in numbers detected between 12 -18 does not fit the numbers predicted so well. There are a number of possible explanations for this behaviour, one is that the angular distribution of the γ-rays has not been extracted thus, perhaps the

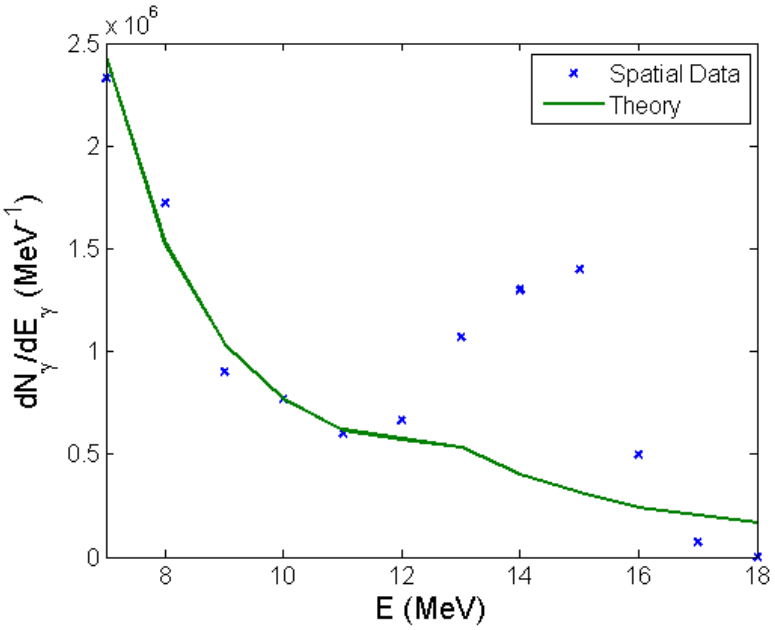

Fig. 9.26: Graph showing the comparison of the numbers of γ-rays detected at best spatial overlap (blue crosses) and the number predicted (green line). As can be seen, there is good agreement between the results obtained and the results predicted in the range 7-12 MeV; however, the increase in number between 12 -18 does not fit the numbers predicted.

arrangement lead to the detection of more high energy γ-rays, which should have a higher number on axis [116]; however, as this cannot be conclusively shown, one must write this aspect of the data off as un-physical and resign ones self to repeating the experiment at a later stage and actively looking at variations in the angular distribution.

From the results presented in figures 9.25 and 9.26, one can see that overall there is excellent agreement between the theoretical prediction and the results obtained. This is strong evidence of an all-optical source of high energy γ-ray beams.

For the final part of the analysis, attention shall move to the Brilliance of the source. Let the source size be comparable to the electron beam diameter at interaction $D_\gamma \approx (30 \pm 3)\mu$m). For the divergence, one imposes the acceptance angle of the γ-ray spectrometer i.e., 3 mrad). Finally, the temporal duration would be comparable to the duration of the wiggler inducing the radiation $\approx$ 45 fs. In a 0.1% bandwidth around 10 MeV, it can be seen that approximately (75 ± 0.2) photons are produced, implying a lower limit for the peak brilliance of $(2.0 \pm 0.4) \times 10^{19}$ γ s^{-1} mm^{-2} mrad^{-2} 0.1% BW.

9.4 Conclusion of Non-Linear Thomson Scattering Experiment in a Counter-Propagating Beam Geometry

When one looks at the results presented in Section 9.3 in the context of current sources available such as synchrotrons, LINAC's and Bremsstrahlung sources, the NLTS source demonstrates unprecedented brilliance for the energy range. In figure 1.3 many sources were compared, the current work is added to this in order to contextualise the results.

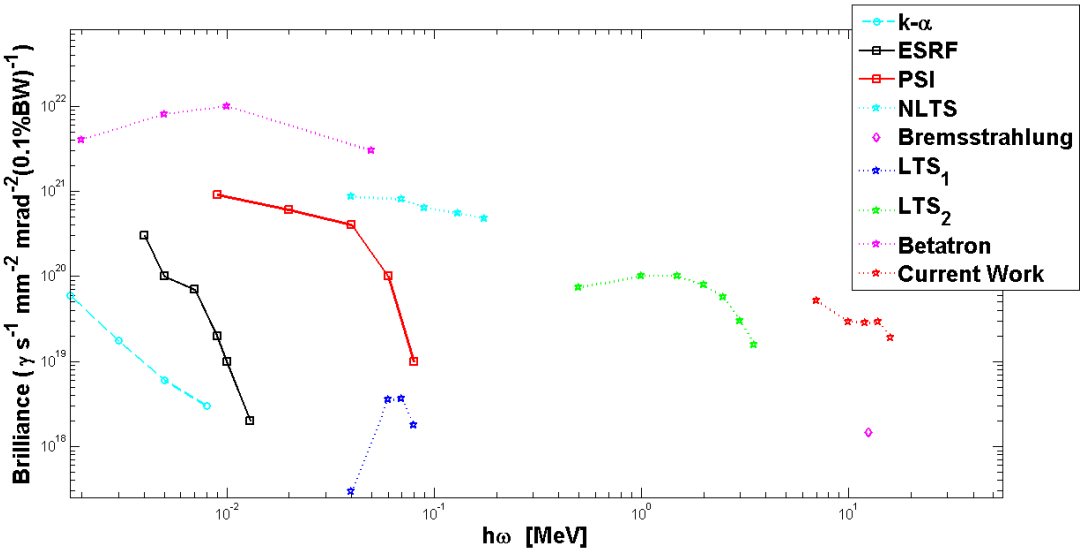

Fig. 9.27: Comparison of the present γ-ray source with other generation mechanisms reported in the literature.

As can be seen from figure 9.27, many current sources are able to achieve higher brightnesses than those presented here. However, the energies that are achievable by these devices are limited to th keV regime. Beyond MeV, sources such as Bremsstrahlung source in reference [23] can extend up to multi and even 100's MeV regime (the maximum energy achievable from a Bremsstrahlung source is limited by the energy of the electrons colliding with the high Z target), the large source size and divergence limits the brilliance that can be attained by such sources. The brilliance of the NLTS source is the highest ever achieved in a laboratory for multi-MeV γ-ray sources exceeding by orders of magnitude that achieved using Bremsstrahlung. This is due to the unique combination of high photon energy (maximum of 10-15 MeV compared to a sub-MeV for betatron and a maximum of a few MeV for linear relativistic Thomson scattering sources), high photon number (approximately 10^7 photons with energy exceeding 6 MeV per laser shot), small divergence and source size (3 mrad and 30 μm compared to tens of mrad and hundreds of microns for typical bremsstrahlung sources, respectively), and short duration (tens of fs, compared to picoseconds or nanoseconds for solid-state systems).

Regarding the results of the spatial scan presented in figure 9.26, it has been suggested that the number of high energy photons detected on axis should be higher [116] but without further work, the result must remain for now, anomalous.

In conclusion, experimental evidence of non-linear relativistic Thomson scattering in a two-laser counter-propagating geometry has been demonstrated. The calibrated spectrum of the generated γ-ray beam has been seamlessly measured, with MeV resolution, from 7 to 16 MeV and provides clear experimental evidence of non-linear relativistic Thomson scattering. Thanks to the high photon number generated, short duration, narrow divergence, and small source size, this photon source presents the highest peak brilliance ever obtained in the laboratory in a multi-MeV energy window.

Part IV

OUTLOOK

10. OUTLOOK

In Chapter 2, the possibility of using an intense laser to couple energy into a plasma was shown. LWFA has been shown as an effective way of generating high energy electron beams and in Chapter 3, the action of an intense laser on such a beam was shown to be an effective way of generating high energy photons. Getting such beams to interact posed a significant technical challenge; however, in Chapter 8 this problem was overcome by using a modified version of spectral interferometry. Using the lithium detector presented in Chapter 7, the setup presented in Chapter 9 was shown to yield significant results in the field of high energy photon sources. These successful results pave the way for exciting new pathways which the work can proceed.

10.1 Applications and Improvements of the Non-Linear Thomson Scattering Source

In terms of the practical implications of the work, as stated in the opening Chapter, high energy photon sources are required for not only in fundamental research [1], but have important practical applications which include cancer radiotherapy [2, 3], active interrogation of materials [4], and radiography of dense objects [5]. The advantages of such an all-optical source of such γ-ray beams come in the form of it's compact nature, relatively low cost and ultra-high brilliance. The work presented here can be used as a launch-pad for such undertakings to begin.

Looking back specifically at Section 9.3, one can see there are many improvements which can easily be made. Firstly, improvements in the LWFA process are continually being made and increasing the energy and number of electrons created by the driver, can increase the number of photons generated and decrease the divergence of source (which is linked intrinsically to the Lorentz factor: γ^{-1}). In addition, as laser technology continues to improve, the duration of the source can be reduced and the intensity increased. All of these factors make a contribution to the increasing brightnesses available.

The demonstration of an optical and compact source of bright and multi-MeV γ-rays, provides a unique opportunity for studies in nuclear physics to be carried out in laser laboratories. As work is in its infancy, there is much scope for development which will

lead to the compact-scale production of high quality γ-ray beams for use in the medical industry and the non-invasive scanning of shipping containers.

However, the spectra produced when moving into the non-linear intensity regime remains an issue that needs to be tackled. Equation 10.1 gives the expected bandwidth:

$$\frac{\Delta\omega_B}{\omega_B} \approx \sqrt{\left(\frac{2\Delta\gamma}{\gamma}\right)^2 + \left(\frac{\Delta\omega_L^2}{\omega_L}\right)^2 + \left(\frac{a_0^2}{2}\right)^2} \tag{10.1}$$

The first term shows the importance of obtaining high energy mono-energetic sources of electrons through LWFA while the second term relates to the bandwidth of the laser itself. This latter term is generally small and does not make a significant contribution to the broadening when compared to the other terms. The final term demonstrates that at high intensities, as the electron emits continuously during its interaction with the laser field, the stronger the field, the wider the bandwidth. While it may seem like this is a problem that cannot be resolved, it has been recently proposed that a suitable chirp of the scattering laser might minimise this issue. An example of these theoretical predictions can be found in reference [117] (see figure 10.1 for an example of these calculations). Research needs to be continued and work has been shown to already underway to develop further

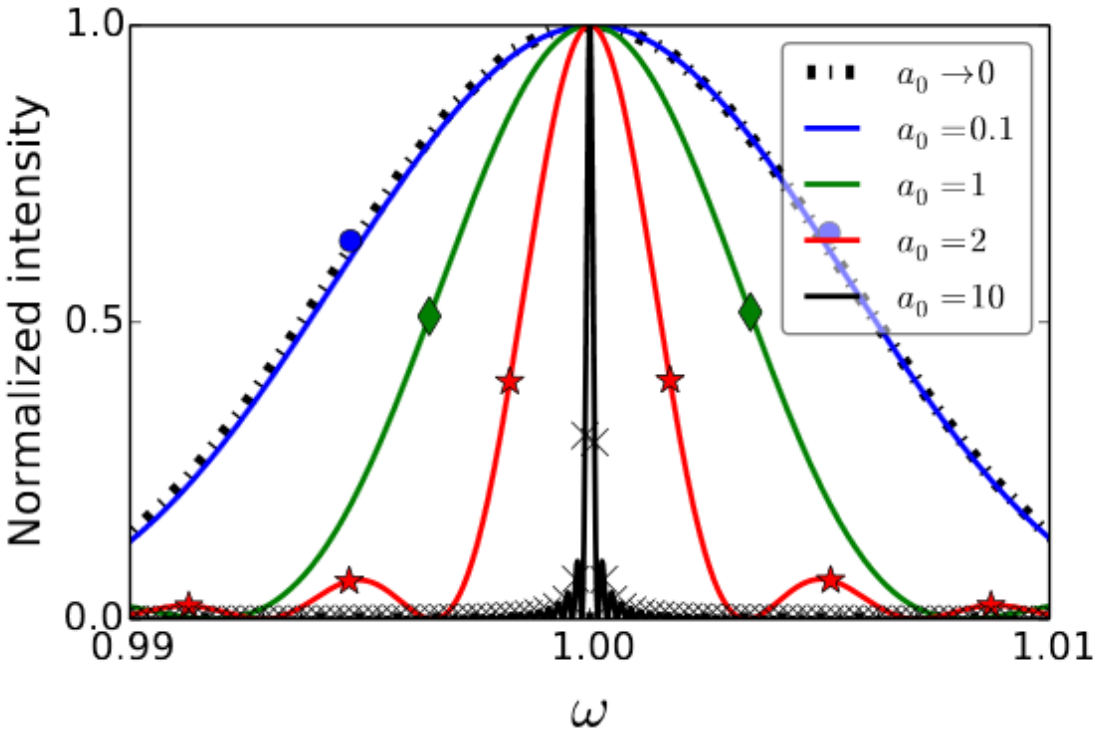

Fig. 10.1: The graph shows the normalised intensity against the normalised frequency of the emitted photons [117].

the LWFA technique. As well as better quality electron beams, more intense lasers will of course, be a welcome addition to the field allowing higher intensities larger focal spots with which to interact. As well as trying some of the methods outlined in reference [117].

10.2 From Non-Linear Thomson Scattering to Quantum Electrodynamics

The NLTS results presented in this thesis have been completely classical in nature i.e., The interaction of the laser and the electron has not required any significant changes from the classical picture. However, with an ultra-relativistic electron beam of $\gamma \gg 10000$ would give a γ-ray spectrum with lower energies than that predicted classically. If the intensity of the laser is sufficient to interact with the virtual photons in the field of the electron, then the quantum radiation reaction effect [26, 59] becomes significant and the electron spectrum will be significantly altered. In these circumstances, merely looking at the γ-ray spectrum will be insufficient in describing accurately what has happened during the interaction. For a truer picture, one may be required to look at the electron beams energy before and after the interaction, or produce an extremely stable mono-energetic electron beam via LWFA.

Work has already been carried out using improved LWFA techniques developed by collaborates in Imperial College London, where energies are generated between 1-2 GeV and charges in the nC scale [118]. Coupled with the improvements that have been made on Astra Gemini (pulse in the order of 30 fs), the stage is set to bring these quantum effects fully to bear.

One such effect which will be accessible is that of radiation reaction (RR). In RR, the effect of the electromagnetic field scattered by an electron on itself (self-interaction). This can modify the energy and trajectory of the electron. The rate of energy loss of the electron is given by $\gamma(t) = \gamma_0/(1+\nu_\gamma t)$ where γ_0 is the initial Lorentz factor of the electron and

$$\nu_\gamma = \frac{\tau_0}{2}\gamma_0 a_0^2\Big(\frac{2\pi c}{\lambda_u}\Big)^2 \tag{10.2}$$

Here, $\tau_0 = 2r_e/3c = 6.26 \times 10^{-24}$ s. RR can only be neglected if the critical frequency $\omega_c \ll \nu_\gamma$ i.e., energy losses are faster than the emission of radiation. By comparing the energy of an electron spectra before and after laser interaction, it is possible to perform simulations in order to form a prediction based on electron interactions with intense laser pulse with this effect turned off (a Compton only picture) and make comparison to those with the effect included [119, 116]. By making a direct comparison with results obtained, one is presented with the opportunity of observing this effect.

Getting such a comparison is non-trivial but work is underway in this respect and QUB is developing double magnetic spectrometer which spectrally resolves electrons before laser interaction, then again after interaction in the transverse plane in order to allow one to make direct comparisons. This has been trailed and will continue to be improved upon in order to allow the group access to this thus far, illusive regime.

A second point of interest of QED is the photon-photon scattering for pair production. The high number density of photons present in intense lasers can yield the creation of virtual eigenstates which can lead to the production of an electron-positron pair provided momentum was conserved e.g. created by lasers in a counter propagating geometry. Previously the electric field strength was given as the Schwinger limit ($E_L = 1.3 \times 10^{18}$ Vm^{-1}[59]). While increasing the intensity of lasers to this limit is technologically far from grasp, other avenues can be explored. As the cross section of such photon-photon interactions increases as the energy of the photons increases to 1 MeV, using a coherent x-ray source which is coupled to an intense laser such as that available in Stanford LINAC or SLAC, one may be able to use LWFA to produce Bremsstrahlung radiation and enhance significantly, the cross-sections for interaction. However, a major issue which needs to be addressed is that of the signal to noise ratio. As detecting a single relativistic electron-positron pair, in an environment containing many orders of magnitude of high energy photos is beyond the limitations of any detector which has been presented here, unique detectors will need to be developed to enable this.

10.3 Detection of Relativistic Charges in High-Noise Environments

The speed of light in a vacuum is an invariant quantity [59]. However, the phase velocity of light in a material may vary due to the presence of charges within the material which light propagates. If light propagates through a material of refractive index $\eta > 1$, then the velocity of light in that material is given by $v_\phi = c/\eta$. However, as charged particles may not exceed the speed of light in a vacuum, they may travel through a medium with $v_e \approx c$; Thus, in that material, they may be observed to be travelling at a velocity which exceeds the speed of light $v_e > v_g$. This leads to an important non-linear effects in the medium known as Čerenkov radiation. This process gives rise to optical photons due to the charge propagating through a medium at velocities exceeding that of light in that medium. The result is that at a particular angle θ_c, radiation is observed. Then the ratio of $v_g/\beta c$ is found to be the cosine of the angle between the two vectors.

$$\cos\theta_c = \frac{1}{\beta\eta} \tag{10.3}$$

The emission is many times faster than processes such as scintillation and the yield obtained from such an effect can be described by the fundamental equation for the output of radiation

$$\frac{dW}{dl} = \frac{e^2}{c^2} \int_{\beta\eta>1} \left(1 - \frac{1}{\beta^2\eta^2}\right) \tag{10.4}$$

Imposing cut-off limits in the frequencies that may be emitted, equation 10.4 becomes

$$N = 2\pi\alpha l\left(\frac{1}{\lambda_2} - \frac{1}{\lambda_1}\right)\left(1 - \frac{1}{\beta^2\eta^2}\right) \tag{10.5}$$

Where $\alpha = e^2/\hbar c = 1/137$ [120]. It is therefore, conceivable that one could exploit the short timescale by using a fast gated camera so as not to see any scintillation or other effects which may give spurious reults, as well as filter out any stray laser light, and bevel the light to select only the unique angle of emission, in order to detect a potentially large number of photons from the effect. This has the potential to become an alternative form of detection for relativistic electrons, from the traditional forms of detection from Image Plates or LANEX screens [84, 85, 79], or exploit the large yields generated by single charged particles moving with relativistic velocities. In addition to this practical benefit, in environments were noise is intrinsically high, the unique mechanism generating the radiation gives a practical way of discerning between high energy photons (which emit no radiation) and relativistic charges (which will). This means that a potential solution is available for those wishing to pursue photon-photon scattering effects using lasers.

ROLE OF AUTHOR

During the course of the doctoral thesis presented in this herein, the author has endeavoured to make a large and positive contribution to this project and take a lead role whenever possible. The work was carried out under the close supervision of G. Sarri and M. Zepf. The work presented is entirely the authors, otherwise referenced appropriately within the text.

The author used the Monte Carlo scattering code FLUKA to design the lithium detector. The work presented in Chapter 7 was therefore, that of the authos with the exception of figure 7.12, which was supplied by G. Sarri.

During the course of this particular campaign, the author was able to develop both the analytical equations and the subsequent predictions of fringe behaviour using the program Matlab. With the assistance of T. Dzelzines and M. Yeung, the experiment in TARANIS which would be used to verify those predictions was designed and lead by the author.

In Chapter 9, the author played a key role in the experiments design and imlemntation. This included designing and implementing the lithium detector, working to ensure smooth implementation of the spectral interferometer as well as desining and implementing the probe-line used to perform interferometry and shadowgraphy of the gas-cell.

In terms of analysis during the NLTS campaign, the author was responsible for determining the shots which showed NLTS signal and extracting the relevant electron spectra from the LWFA data. Beam profiles were extracted by J. Cole and these pertinent pieces of information were given to C. Harvey for simulation purposes. It was C. Harvey who provided the normalised spectra presented here. The author developed and implemented the fitting equations for deconvolution that would yield the final results. The electron spectra from the lithium detector were extracted by G. Sarri.

PUBLICATIONS PERTINENT TO THIS THESIS

In order of publication:

Design of a compact spectrometer for high-flux MeV γ-ray beams.
Authored by; D. J. Corvan, M. Zepf & G. Sarri
Published in; Review of Scientific Instruments **85**, 065119 (2014).

Ultrahigh Brilliance Multi-MeV γ-Ray Beams from Nonlinear Relativistic Thomson Scattering
Authored by; G. Sarri, D.J. Corvan, W. Schumaker, J.M. Cole, A. Di Piazza, H. Ahmed, C. Harvey, C.H. Keitel, K. Krushelnick, S.P.D. Mangles, Z. Najmudin, D. Symes, A.G.R. Thomas, M. Yeung, Z. Zhao, & M. Zepf
Published in; Physical Review Letters **113** 224801 (2014).

Optical measurement of the temporal delay between two ultra-short and focussed laser pluses.
Authored by; D. J. Corvan, T. Dzelzainis, C. Hyland, G. Nersisyan, M. Yeung, M. Zepf, & G. Sarri
Published in; Optics Express **24**, 3127 (2016).

A high-energy, high-flux source of gamma-rays from all-optical non-linear Thomson scattering
Authored by; D. J. Corvan, M. Zepf & G. Sarri
Published in; Nuclear Instruments and Methods in Physics Research Section A: Accelerators, Spectrometers, Detectors and Associated Equipment
in press (2016).

BIBLIOGRAPHY

[1] Y.K. Wu. International Workshop on Polarized Sources, Targets and Polarimetry (University of Virginia 2013) (2013).

[2] A. Laugier. Annuaire de la Cancrologie/Radiothrapie et des Imageries Mdicales en France, Hopital Tenon, Paris 20 (1995).

[3] T. S. Lawrence *et al.* Principles and Practice of Oncology. 8th ed. Philadelphia: Lippincott Williams and Wilkins, (2008).

[4] T. S. Lawrence *et al.* ANSI N42.41-2007, 1,35, Feb. 15 2008.

[5] Y. Glinec *et al.* Phys. Rev. Lett. **94**, 025003 (2005).

[6] W. Bertozzi *et al.* Phys. Rev. C, **78**, 041601 (2008).

[7] J. Frittelli. Port and Maritime Security, Background and issues for Congress, CRS Report RL31733, US Library of Congress, (2005).

[8] Csi: Container security initiative. `http://www.cbp.gov/border-security/portsentry/cargo-security/csi/csi-brief`.

[9] J.M. Hall *et al.* Nucl. Inst. Meth. Phys. B **261**, 337, (2007).

[10] D.R. Slaughter *et al.* Nucl. Inst. Meth. Phys. B **241**, 777, (2005).

[11] D. J. Corvan *et al.* Nucl. Inst. Meth. Phys. A **in print**, (2016).

[12] E. B. Podgorsak. Radiation Oncology Physics: A Handbook for Teachers and Students*, IAEA, Wien 2005.*

[13] Gamma knife therapy. "`http://www.gammaknife.org.uk/treatment/what-is-a-gamma-knife`".

[14] Gamma knife overview. "`https://en.wikipedia.org/wiki/Radiosurgery#Gamma_Knife`".

[15] V. Bom *et al.* Phys. Med. and Bio. **56**, 3199 (2011).

[16] K. Li & L. Ma. Phys. Med. and Bio. **49**, 3455 (2004).

[17] A. Rousse *et al.* Phys. Rev. E **50**, 2200 (1994).

[18] Accelerators. "`http://www.esrf.eu/Accelerators/Performance/Brilliance/`".

[19] Psi. "`http://www.psi.ch/sls/microxas/femto/`".

[20] P. Argan *et al.* Nucl. Instr. Meth. Phys. **228**, 20 (1984).

[21] D. I. Thwaites and J. B. Tuohy. Phys. Med. Biol. **51**, R343 (2006).

[22] C. B. Schroeder E. Esarey and W. P. Leemans. Rev. Mod. Phys. **81**, 1229 (2009).

[23] A. Giulietti *et al.* Phys. Rev. Lett. **101**, 105002 (2008).

[24] W. Schumaker *et al.* Phys. Plasmas **21**, 056704 (2014).

[25] S. Kneip *et al.* Nat. Phys. **7**, 737 (2012).

[26] A. Di Piazza *et al.* Rev. Mod. Phys. **84**, 3, 1177 (2012).

[27] N. D. Powers *et al. Nat. Phot.* ***8*** *28 (2014).*

[28] C. Liu *et al.* Opt. Lett. **39**, 4132 (2014).

[29] K. Ta Puhoc *et al.* Nature. Phot. **6**, 308 (2012).

[30] The flash laser system. "`http://flash.desy.de/`".

[31] S. Cipiccia *et al.* Nat. Phys. **7**, 867 (2011).

[32] L. H. Gray. R. Soc. Lond. A **128**, 361 (1930).

[33] R. H. Milburn *et al.* Phys. Rev. Lett. **10**, 75 (1963).

[34] F. R. Arutyunyan *et al.* Phys. Rev. Lett. **4** 176 (1963).

[35] S. Corde *et al.* Rev. Mod. Phys. **85**, 1 (2013).

[36] S.H. An *et al.* Nucl. Inst. Meth. Phys. A **571**, 251, (2007).

[37] A. Studen *et al.* Nucl. Inst. Meth. Phys. A **501**, 273, (2003).

[38] M. Csatlós *et al.* Nucl. Inst. Meth. Phys. A **421**, 272, (1999).

[39] M. Wilhelm *et al.* Nucl. Inst. Meth. Phys. A **381**, 462, (1996).

[40] M. Lipoglavšek *et al.* Nucl. Inst. Meth. Phys. A **557**, 523, (2006).

[41] C. Harvey *et al. Phys. Rev. A **79** 063407 (2009).*

[42] F. Mackenroth and A. Di Piazza. Phys. Rev. A **83** 032106 (2011).

[43] G. Sarri *et al. Phys. Rev. Lett. **113** 224801 (2014).*

[44] K. Khrennikov *et al.* Phys. Rev. Lett. **114**, 195003 (2015).

[45] B. A. Remington *et al.* Rev. Mod. Phys. **78** 755 (2006).

[46] O. Lundh*et al.* Nat. Phys. **7** 219 (2011).

[47] D. Umstadter *et al.* Phys. Rev. Lett. **76** 2073 (1996).

[48] A. R. Bell and J. G. Kirk. Phys. Rev. Lett. **101** 200403 (2008).

[49] F. F. Chen. Introduction to Plasma Physics and Controlled Fusion*, volume 1. Plasma Physics, Springer, 2 edition, 2006.*

[50] K.J. Orford. Nature **267**, 103, (1977).

[51] R. Dendy. Plasma Physics An Introductory Course*, volume 1. Plasma Physics, Cambridge University Press, 1 edition, 1996.*

[52] W. L. Kruer. The Physics of Laser Plasma Interactions*, volume 1. Plasma Physics, Westview Press, Frontiers in Physics, 1 edition, 2003.*

[53] S. V. Chekalin & V. P. Kandidov. *Physics. Uspekhi **56**, 123, (2013).*

[54] C. Yamanaka *et al. Phys. Rev. A **11**, 2139, (1975).*

[55] T. Tajima & J. M. Dawson. Phys. rev. Lett. **43**, 267 (1979).

[56] E. Fermi. Phys. rev. **75**, 1169 (1949).

[57] N. H. Matlis *et al.* Nat. Phys. **2**, 749 (2006).

[58] A. Hofmann. The Physics of Synchrotron Radiation*, Cambridge University Press, 1 edition, 2004.*

[59] Lifshitz Beresteetskii and Pitaevskii. L. D. Landau and E. M. Lifshitz Quantum Electrodynamics*, volume 4, Pergamon Press, 4 edition, 1980,.*

[60] Extreme Light Infrastructure. "`http://www.eli-beams.eu/`".

[61] C.A. Ur *et al.* Nuclear Instruments and Methods in Physics Research B **355** 198 (2015).

[62] P. Constantin *et al.* Nuclear Instruments and Methods in Physics Research B **372** 78 (2016).

[63] S. Leoni *et al.* ACTA PHYSICA POLONICA B **46** 637 (2015).

[64] E. Rutherford. Philosophical Magazine **21**, 669 (1911).

[65] N. Bohr. Philos. Mag. **26**, 1 (1913).

[66] A. Einstein. Physika Zeitschrift **18**, 121 (1917).

[67] C. C Davis. Lasers and Electro-Optics*, Cambridge University Press (1995).*

[68] E. Hecht. Optics*, 3 edition, 1998.*

[69] D. Strickland & G. A. Mourou. Opt. Commun. **56**, 219, (1985).

[70] G. A. Mourou *et al. Rev. Mod. Phys.* ***78****, 309, (2006).*

[71] The national grid (uk) 2014. "`http://www2.nationalgrid.com/uk/Industry-information/electricity-transmission-operational-data/`".

[72] C Boulmer-Leborgne *et al.*

[73] O.Chekhlov *et al.* Z.Bor Opt. Lett. 14, 119 (1989).

[74] J. L. Collier *et al.* Quantum Electronics and Laser Science Conference (QELS) (2005).

[75] C.J. Hooker *et al.* J. Phys. IV France **133**, 673 (2006).

[76] C.J. Hooker *et al.* Optics Express **19**, 2193 (2011).

[77] Amplitude. "`http://www.amplitude-technologies.com/`".

[78] T. P. A. Ibbotson *et al.* New Journal Phys. **12**, 045008 (2010).

[79] *et al.* Y. Glinec. Rev. Sci. Instrum. **77**, 103301, (2006).

[80] T. P. A. Ibbotson *et al.* Plasma Phys. Control. Fusion **46**, B179 (2004).

[81] M. Vargas *et al.* Phys. Plasmas **104**, 174103 (2014).

[82] W. P. Leemans *et al. Proceedings of PAC2013, Pasadena, CA, 1097, (2013).*

[83] W. P. Leemans *et al. Phys. Rev. Lett.* ***113****, 245002, (2015).*

[84] B.R. Maddox *et al.* Rev. Sci. Instrum. **82**, 023111, (2011).

[85] K.A. Tanaka *et al. Rev. Sci. Instrum.* **76**, 013507, (2005).

[86] Y. Amemiya & J. Miyahara. Nature **336**, 89, (1998).

[87] G. Jackson Williams *et al. Rev. Sci. Instrum.* **85**, 11E604, (2014).

[88] N. Nakanii *et al. Rev. Sci. Instrum.* **79**, 066102, (2008).

[89] I. J. Paterson *et al. Meas. Sci. Technol.* **19**, 095301, (2008).

[90] Y. Glinec. Propagation d'une impulsion laser ultra-intense dans un plasma sous-dense Génération de faisceaux d'électrons quasi monoénergétiques et développement d'applications. *École Polytechnique PhD dissertation, (2006).*

[91] Y. Glinec *et al. CARE-Report-(2006).*

[92] Fujifilm medical products.

[93] Imagej. `http://imagej.nih.gov/ij/`.

[94] National institute of standards and technology. `http://www.nist.gov/`.

[95] *et al.* W. C. Priedhorsky. Rev. Sci. Instrum. **54**, 1605, (1983).

[96] Film-screen systems and kodak lanex screens. "`http://www.ndt-service.de/wp-content/uploads/2012/02/Lanex-screens.pdf`".

[97] *et al.* K. Nakamura. Phys. Rev. ST Accel. Beams **14**, 062801, (2011).

[98] W. Schumacker *et al. to be published (2014).*

[99] A. Ferrari*et al.* CERN-2005-10 , INFN/TC 05/11, SLAC-R-773, 2005.

[100] S. Roesler *et al.* Computing in High Energy and Nuclear Physics 2003 Conference (CHEP2003), La Jolla, CA, USA, March 24-28, 2003.

[101] G. Sarri *et al.* Phys. Rev. Lett. **110**, 255002, (2013).

[102] D. J. Corvan *et al.* Rev. Sci Instrum. **85**, 065119 (2014).

[103] Y. Eisen *et al.* Nucl. Inst. Meth. Phys. A **490**, 505, (2002).

[104] J. Piasecki *et al.* Appl. Opt. **19** 3749 (1980).

[105] D. Yelin D. Meshulach and Y. Silberberg. Opt. Soc. Am. B **14** 2095 (1997).

[106] C.N. Danson *et al.* Nucl. Fusion **44** 239 (2004).

[107] T. Dzelzainis *et al. Laser and Particle Beams **28**, 451, (2010).*

[108] Coherent. "`http://www.coherent.com/`".

[109] Mira 900f oscillator from coherent. "`http://neurophysics.ucsd.edu/Manuals/Coherent,%20Inc/Mira%20Optima%20900-F%20Laser%20Operator's%20Manual.pdf`".

[110] C. Bula *et al.* Phys. Rev. Lett. **76**, 3116 (1996).

[111] W. Schumaker. Doctoral Thesis (2014).

[112] I. H. Hutchinson. Principles of Plasma Diagnositcs*, volume 1. Plasma Physics, Cambridge University Press, 2 edition, (2002).*

[113] Andor. "`http://www.andor.com/`".

[114] D. J. Corvan *et al.* Optics Express **24**, 3127 (2016).

[115] Thorlabs. "`http://www.thorlabs.de/`".

[116] A.G.R. Thomas *et al.* Phys. Rev. X **2** 041004 (2012).

[117] S.G. Rykovanov *et al.* accepted Phys. Rev. Lett. (2016).

[118] K. Poder *et al.* APS conference proceedings (2015).

[119] T. G. Blackburn *et al.* Phys. Rev. X **112** 015001 (2012).

[120] J. V. Jelley. Čerenkov Radiation*, Pergamon Press, 1 edition, 1958.*